CLIMATE CHANGE EFFECTS ON THE REGIONAL SEAS OF TÜRKİYE FOCUSING ON PROJECTED EXTREME SEA LEVEL AND COASTAL FLOODING IN THE BLACK SEA

by
Pelin Uzun
B.S., Civil Engineering, Boğaziçi University, 2016
M.S., Civil Engineering, Boğaziçi University, 2019

Submitted to the Institute for Graduate Studies in
Science and Engineering in partial fulfillment of
the requirements for the degree of
Doctor of Philosophy

Graduate Program in Civil Engineering
Boğaziçi University
2025

ACKNOWLEDGEMENTS

I would first like to express my deepest gratitude to my beloved partner, Şükrü Olcay, and my dearest cat, Macun, for their endless support, love, and patience throughout this challenging journey. Their presence has been a source of strength and comfort during my studies.

It has been a privilege to work under the supervision of Professor Emre Otay, whose invaluable guidance, patience, and encouragement have shaped my academic journey. His insightful feedback and continuous support have been instrumental not only in completing this thesis but also in inspiring and guiding my path into an academic career.

I am also sincerely grateful to my thesis committee members, Professor Cem Avcı and Associate Professor Başak Güven, for their constructive comments and insightful suggestions during each progress presentation, which significantly contributed to the development and refinement of this thesis. I would also like to thank Professor Adem Akpınar and Professor Servet Karasu for their time and interest in participating in my thesis defense jury.

In addition, I would like to thank Dr. Recep Emre Çakmak for kindly answering my questions regarding the calibration and validation processes during the wave modeling. I would also like to thank my colleague and friend, Emre Tekdemir, for his continuous support and encouragement throughout this journey, especially for his invaluable assistance on the day of my thesis defense.

Finally, I would like to extend my sincere appreciation to my family and friends, who have always believed in me and supported me unconditionally throughout this demanding process.

ABSTRACT

CLIMATE CHANGE EFFECTS ON THE REGIONAL SEAS OF TÜRKİYE FOCUSING ON PROJECTED EXTREME SEA LEVEL AND COASTAL FLOODING IN THE BLACK SEA

Sea-level rise driven by climate change significantly threatens coastal regions by increasing flooding and erosion, impacting ecological, social, and economic systems. The main objective of this study is to analyze future total water levels (TWL), tidal elevations (TE), and storm surge (SS) in the regional seas of Türkiye, and project extreme sea levels (ESL) in the Black Sea under climate scenarios until 2100. This study presents the first dynamic shoreline-based modeling for the Black Sea, enhancing the spatial accuracy of flood projections. A novel contribution is the dynamic shoreline-based modeling approach, updating shoreline positions and slopes at each simulation step for both spectral wave modeling and wave runup computations. Using regional climate model (RCM) outputs from CMIP5 datasets provided by the Copernicus Climate Change Service (C3S), the methodology involved statistical analysis, spectral wave modeling (2071–2100), wave runup computations, ESL estimation, and flood mapping. Statistical analysis quantified trends and extremes in TWL, TE, and SS. Wave projections were generated using the SWAN model calibrated with regional wind data by comparing annual mean wave characteristics against ERA5 datasets. Wave runup was calculated with empirical formulas, integrating spatial slopes and wave projections for ESL determination. ESL values were propagated inland to delineate flood extents along the Black Sea coast. The results showed that extreme TWL is projected to rise up to 920 mm along the Ukrainian Sea of Azov and 440 mm along the Romanian Black Sea coast by 2100. The southwestern Azov Sea shows the highest SS rise (590 mm), while the north may see reductions up to 480 mm. The 99th percentile significant wave height is expected to rise up to 20%. Under extreme conditions, wave runup reaches 4–6 m between Zonguldak and Sinop, and exceeds 5 m near southeastern Crimea. ESL-based flood mapping shows a 640 km² increase in inundation compared to TWL-based extents under average conditions, mainly over low-lying deltas in Romania and Ukraine.

ÖZET

KARADENİZ'DE ÖNGÖRÜLEN AŞIRI DENİZ SEVİYESİ VE KIYI TAŞKINLARINA ODAKLANARAK TÜRKİYE'NİN BÖLGESEL DENİZLERİ ÜZERİNDEKİ İKLİM DEĞİŞİKLİĞİ ETKİLERİ

İklim değişikliğine bağlı deniz seviyesi yükselmesi, kıyı bölgelerinde su baskını ve erozyonu artırarak ekolojik, sosyal ve ekonomik sistemleri etkilemektedir. Bu çalışmanın amacı, Türkiye'nin bölgesel denizlerinde gelecekteki toplam su seviyesi (TWL), gelgit (TE) ve fırtına kabarması (SS) koşullarını analiz etmek ve 2100 yılına kadar Karadeniz için aşırı deniz seviyesi (ESL) projeksiyonları üretmektir. Özgün katkı olarak, hem spektral dalga modeli hem de dalga tırmanışı hesaplamalarında her zaman adımında kıyı çizgisi ve eğimin güncellendiği dinamik kıyı çizgisi tabanlı modelleme yaklaşımı sunan bu çalışma, Karadeniz için yapılan ilk dinamik kıyı çizgisi tabanlı modeli sunmakta ve projeksiyonların mekânsal doğruluğunu artırmaktadır. Copernicus İklim Değişikliği Servisi tarafından sağlanan CMIP5 veri setine ait bölgesel iklim modeli çıktılarıyla istatistiksel analiz, spektral dalga modellemesi (2071–2100), dalga tırmanışı hesaplaması, ESL belirlemesi ve taşkın haritalaması yapılmıştır. Analizler TWL, TE ve SS bileşenlerinin eğilimlerini ortaya koymuştur. Dalga projeksiyonları, yıllık ortalama dalga özelliklerinin ERA5 ile karşılaştırılmasıyla, bölgesel rüzgar verileri kullanılarak kalibre edilen SWAN modeliyle elde edilmiştir. Dalga tırmanışı, eğim ve dalga projeksiyonlarının entegre edildiği ampirik formüllerle hesaplanmış, ardından ESL değerleri kıyıdan iç kesimlere yayılmıştır. Ekstrem TWL'nin 2100 yılına kadar Azak Denizi'nin Ukrayna kıyılarında 920 mm'ye, Karadeniz'in Romanya kıyılarında ise 440 mm'ye kadar yükselmesi beklenmektedir. Güneybatı Azak Denizi'nde SS artışı 590 mm'ye ulaşmakta, kuzey kıyılarda ise 480 mm'ye varan azalma öngörülmektedir. aşırı dalga yüksekliği batı ve orta Karadeniz'de %20'ye kadar artmakta, maksimumlar 4.0 m'ye ulaşmaktadır. Aşırı koşullarda dalga tırmanışı Zonguldak-Sinop arasında 4–6 m'ye, güneydoğu Kırım kıyılarında ise 5 m'nin üzerine çıkmaktadır. ESL tabanlı haritalar, ortalama koşullarda TWL'ye göre yaklaşık 640 km² ek taşkın alanı göstermekte, özellikle Romanya ve Ukrayna'daki alçak kotlu deltaları etkilemektedir.

TABLE OF CONTENTS

LIST OF FIGURES

LIST OF TABLES

LIST OF SYMBOLS

A	Linear growth term
A_i	Actual value at year i
B	Exponential growth term
B_i	Benchmark (observed) value
$\bar{B}$	Mean of benchmark data
C_{ds2}	Whitecapping dissipation coefficient (calibration setting)
c_x	Group velocity component in x direction
c_y	Group velocity component in y direction
c_σ	Propagation velocity in σ space
c_θ	Propagation velocity in θ space
c_{ph}	Phase speed
d	Water depth
E	Energy density spectrum
g	Gravitational acceleration
h	Instantaneous water depth
H	Filter function (growth function)
H_0	Deep-water significant wave height
H_s	Significant wave height
H_{99}	99th percentile significant wave height
k	Wave number
$\tilde{k}$	Mean wave number
L	Wave length
L_0	Deep-water wave length
M_i	Modeled value
$\bar{M}$	Mean of modeled data
N	Action density
m_0	Zeroth spectral moment
m_2	Second spectral moment
n	Number of data points or years

p	Tunable coefficient (whitecapping dissipation)
R_2	2% exceedance wave runup
S	Source term (generation, dissipation, interactions)
S_{in}	Wind input source term
S_{wc}	Whitecapping dissipation source term
S_{nl3}	Nonlinear triad interactions source term
S_{nl4}	Nonlinear quadruplet interactions source term
S_{bot}	Bottom friction source term
S_{brk}	Depth-induced breaking source term
T_i	Trendline value at year i
T_m	Mean wave period
T_p	Peak wave period
t	Time
U^*	Friction velocity
U_{10}	Wind speed at 10 meters height
x	x coordinate
x_i	Year
y	y coordinate
y_i	TWL, SS, or TE values at year i

β	Beach slope
Γ	Wave steepness-dependent coefficient (whitecapping)
γ	Wave height reduction factor
Δ	Shortest angular distance
η	Water surface elevation
θ	Wave direction
θ_ω	Wind direction
μ	Mean value
ξ	Iribarren number
ρ_a	Air density
ρ_ω	Water density
σ	Wave frequency

$\tilde{\sigma}$	Mean frequency
σ_{PM}^{*}	Peak frequency for fully developed sea state
ω	Angular frequency

LIST OF ACRONYMS/ABBREVIATIONS

AW3D30	Advanced Land Observing Satellite World 3D - 30m
BG	Bulgaria
BSBT	Backward Space Backward Time
C3S	Copernicus Climate Change Service
CDS	Climate Data Store
CFD	Computational Fluid Dynamics
CMIP5	Coupled Model Intercomparison Project Phase 5
CoDEC	Coastal Dataset for the Evaluation of Climate Impact
CORDEX	Coordinated Regional Climate Downscaling Experiment
CY	Cyprus
DEM	Digital Elevation Map
DIA	Discrete Interaction Approximation
DJF	December-January-February
DMI	Danish Meteorological Institute
ECMWF	European Centre for Medium-Range Weather Forecasts
EDA	Ensemble Data Assimilation
EG	Egypt
end	end-century period
ERA5	ECMWF Reanalysis v5
ESL	Extreme Sea Level
FW30	Future Waves in 2071-2100
GCM	Global Circulation Model
GE	Georgia
GEBCO	General Bathymetric Chart of the Oceans
GEV	Generalized Extreme Value
GHG	Greenhouse Gas
GIS	Geographic Information System
GR	Greece
GTSM	Global Tide and Surge Model
HAT	Highest Astronomical Tide

HH	Normalized RMSE
hist	historical period
IAM	Integrated Assessment Model
IFS	Integrated Forecast System
IL/PS	Israel/Palestine
IPCC	Intergovernmental Panel on Climate Change
JAXA	Japan Aerospace Exploration Agency
JJA	June-July-August
LB	Lebanon
LTA	Lumped Triad Approximation
MAE	Mean Absolute Error
MAM	March-April-May
MENA	Middle East North Africa
MHHW	Mean Highest High Water
mid	mid-century period
MSL	Mean Sea Level
ND	Normalized Difference
NOAA	National Oceanic and Atmospheric Administration
PD	Probability Distribution
PW20	Past Waves in 1986-2005
RCM	Regional Circulation Model
RCP	Representative Concentration Pathway
RMSD	Root Mean Square Deviation
RMSE	Root Mean Square Error
RO	Romania
RP1	1-year Return Period
RP10	10-year Return Period
RP100	100-year Return Period
RSL	Regional Sea Level
RU	Russia
S06	Empirical formula from Stockdon et al. (2006)
SI	Scatter Index
SLR	Sea Level Rise

SON	September-October-November
SS	Storm Surge
std	standard deviation
SWAN	Simulating Waves Nearshore
SY	Syria
TE	Tidal Elevation
TR	Türkiye
TR-AS	Turkish Coasts of the Aegean Sea
TR-BS	Turkish Coasts of the Black Sea
TR-MED	Turkish Coasts of the Mediterranean Sea
TR-MS	Turkish Coasts of the Marmara Sea
TWL	Total Water Level
UA	Ukraine
USGS	U.S. Geological Survey
WCRP	World Climate Research Programme

1. INTRODUCTION

1.1. General

Climate change has been the focus of the scientific world for many years. Recently, it has become a phenomenon that has attracted the attention of politicians, people, and the media. In other words, not only the studies of scientists on climate change but also the measures to be implemented in this regard have begun to be considered. Consequently, all disciplines are required to act together to control the effects of climate change. Regarding these concerns, Integrated Assessment Models (IAM) have been developed to establish the link between decision-makers and scientists (Hasselmann, 1997; Weber et al., 2005; Hasselmann, 2009; Giupponi et al., 2013; Hasselmann, 2013; Hasselmann and Kovalevsky, 2013; Kovalevsky et al., 2015).

Due to the necessity of high reliability in these integrated models, the number of parameters and variables increases. Consequently, these models become more complex. However, the main purpose of these models is to create a simple link between scientists, engineers, economists, sociologists, and policy-makers. Hasselmann and Kovalevsky (2013) suggested that a hierarchy system consisting of modules for each component (climate, environment, socio-economic system, policy, etc.) can be utilized to keep an IAM simple. Thus, each module of an IAM can be reliable and give detailed projections while its connections with the other are kept simple.

As Hasselmann and Kovalevsky (2013) indicated, the main purpose of the IAMs is to model climate change and its effects in the best and simplest way possible. The simplest way refers to the links between modules, whereas the best way refers to projecting climate change effects properly. For this purpose, the professionals responsible for each module should accurately conduct their work, but keep the information chain between modules as simple and understandable as possible. The scenario prediction in Hasselmann and Kovalevsky (2013) is the link between scientists and policy-makers. For the assessment of coastal hazards, climate system information obtained by scientists should be implemented on coasts by engineers before the information is delivered to policymakers. Hence, if one expands the scenario prediction link, it is understood that more professions are required to simplify the IAM system.

For many years, the Intergovernmental Panel on Climate Change (IPCC) and many other scientists have studied the causes and future of climate change. Its impacts on changes in sea level, sea water temperature, wind patterns, precipitation, evaporation, area of ice coverings, current patterns, wave characteristics, TE, SS, and extreme event frequencies have been studied in detail. These variables are mandatory for assessing the future of coastal areas, and each one is quite complex to model. Considering all the variables and their interactions with each other, it is very time-consuming to dynamically and realistically model the future projection of coastal areas. On the other hand, it is necessary to make the most accurate future projections for coastal adaptation and migration. Furthermore, these variables vary both in time and space. At this point, the best way is to choose the most important and effective variables in a study area and investigate them, considering their impacts on each other.

The assessment of country-scale and/or basin-scale flood hazards for the future diminishes the stress on the economy, policy-makers, and people living in coastal areas and also creates time to decide on coastal adaptation strategies in advance. Identifying the most critical seas and coasts at a subregional scale and investigating these coasts help prevent disasters. After assessing the future of a coastal area, it is necessary to analyze and interpret the model results according to the characteristics of the study area. Thus, a comprehensive prediction of the coastal flood hazard extent of a specific area can be identified, and flood hazard maps can be prepared to guide decision-makers. Knowing the most critical coasts, obtaining coastal flood hazards in the long run, and realizing the role of coastal features enhance the accuracy and feasibility of the adaptation measures.

Türkiye is surrounded by four seas, namely the Eastern Mediterranean, Aegean, Marmara, and Black Seas. The study area covering the regional seas of Türkiye is called the subregion since it is located at the intersection of six CORDEX (Coordinated Regional Downscaling Experiment) domains (Figure 1.1). Considering that these seas have also coasts to 13 countries, assessing their future for climate change is of great importance not only for Türkiye but also for these countries. It is, therefore, important to investigate the impact of climate change on these seas and the roles of different contributors to TWLs. There are some global and regional studies (Muis et al., 2016; Vousdoukas et al., 2017; Melet et al., 2018; Muis et al., 2020) that address different contributions. However, these studies either have a coarse resolution due to global circulation model (GCM) outputs or fail to discuss smaller seas due to insufficient data points. Therefore, a subregional scale study can significantly contribute to the existing literature.

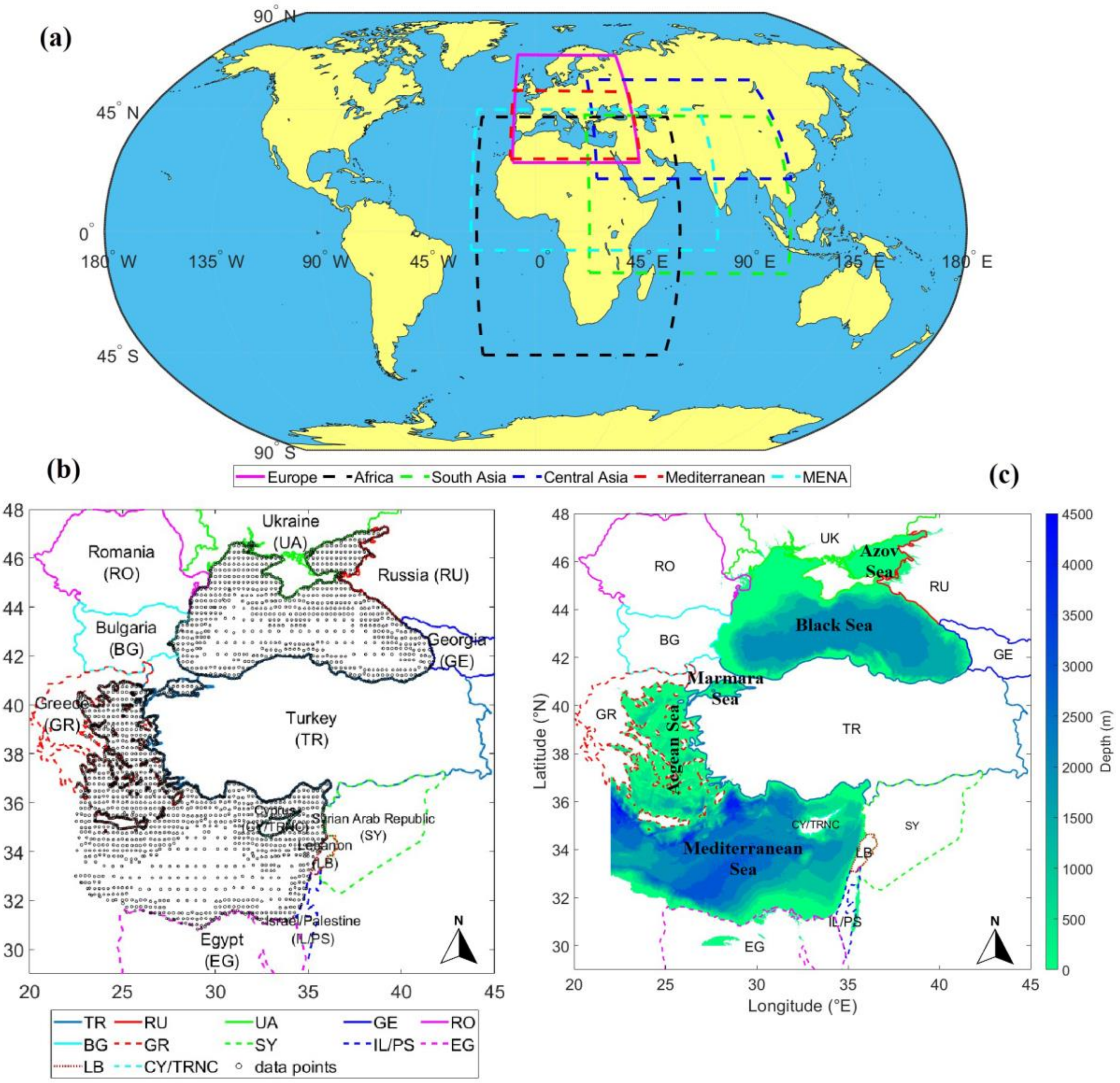

Figure 1.1. The study area: (a) the intersection of the six CORDEX domains, (b) data points, and (c) bathymetry obtained from the General Bathymetry Chart of the Ocean (GEBCO, 2024), adapted from Uzun and Otay (2025).

1.2. Literature Review

The growing concerns surrounding climate change have moved beyond academic circles and become a focal point for governments, media outlets, and the broader public. This shift reflects an increasing recognition of the pressing need to tackle climate-driven challenges. Among the most significant of these is the anticipated rise in sea levels, a gradual yet far-reaching consequence of climate change that poses varying risks across different regions. These risks threaten not only natural coastal environments but also the economic stability and social fabric of communities. As such, projecting future sea-level conditions is vital for assessing the likelihood and intensity of potential coastal hazards. When examined at finer spatial scales, sea-level trends offer critical insights that can ease pressures on vulnerable coastal zones and support the proactive development of adaptive strategies. Targeting areas likely to experience rising TWL and exploring their vulnerabilities allows for better preparation, potentially reducing disaster impacts. This also enables more precise and effective planning by prioritizing hot spot coastlines and estimating future extremes in water level conditions.

Considering these growing concerns, the following sections present a detailed review of key topics, including climate change, regional sea-level trends, the influence of sea-level rise on extreme events, coastal flood hazard assessments, strategies and needs for adaptation and migration, and the specific characteristics of Türkiye’s regional seas, reflecting the increasing depth and intensity of research in these areas.

1.2.1. Climate Change

According to IPCC (2007), global warming has been rising at an increasing rate. The increase in air temperature causes changes in ice cover, precipitation, evaporation, wind patterns, and, consequently, sea level. Changes in wind patterns and sea levels affect the magnitude and frequency of storms, wave characteristics, and current patterns.

The increase in temperature has been attributed mostly to greenhouse gas (GHG) emissions, which have been rising since pre-industrial times. Considering the current situation in the world, it is expected that GHG emissions and temperature will continue to increase without climate change mitigation policies and sustainable development. The rate and amount of this increase have been estimated for years according to different GHG emission scenarios.

The future increase in temperature varies regionally. The Earth's northern hemisphere will face greater temperature rises compared to its southern hemisphere (IPCC, 2007). Especially towards the North Pole, the increase in temperature is higher. Different sectors and systems will respond differently to the impact of the temperature rise. Temperature rise, together with sea level rise (SLR) and extreme weather intensification, affects coastal areas, especially low-lying ones. When rapid urbanization and economic developments are considered, coastal vulnerability and adaptation must be urgently investigated. The worst part is that even if GHG emissions are controlled, the impacts of climate change may grow for decades. The reason is that climate processes need a long time to respond to changes in GHG emissions (Hinkel and Nicholls, 2020).

The chain reaction created by GHG emissions can be summarized as shown in Figure 1.2. Increased GHG emissions cause an increase in atmospheric temperature. This increase in temperature affects evaporation, melting of ice and snow, sea surface temperature, and atmospheric pressure. Changes in atmospheric pressure affect wind characteristics. Changes in evaporation, melting of ice and snow, sea surface temperature, precipitation, and river runoff cause SLR. In addition, SLR causes a change in tidal range. Wave characteristics and SS are affected by SLR, changes in tidal range, and wind. As a result of this climatic process, ESL, consisting of SLR, tidal range, SS, and wave, increases.

The projected global mean SLR rise following the predicted increase in surface temperature is shown in the IPCC report (IPCC, 2007) for the different GHG emission scenarios. Towards the end of the 21st century, global SLR will accelerate. Due to the regional variations of the SLR, it is estimated that worldwide around 70% of coastlines will experience a sea level change of ±20% of the global average. The heightened awareness of climate change underscores the urgency of addressing climate-related issues and has led scientists to diligently study climate change, covering its causes (IPCC, 2021), impacts (IPCC, 2022a), and potential solutions (IPCC, 2022b).

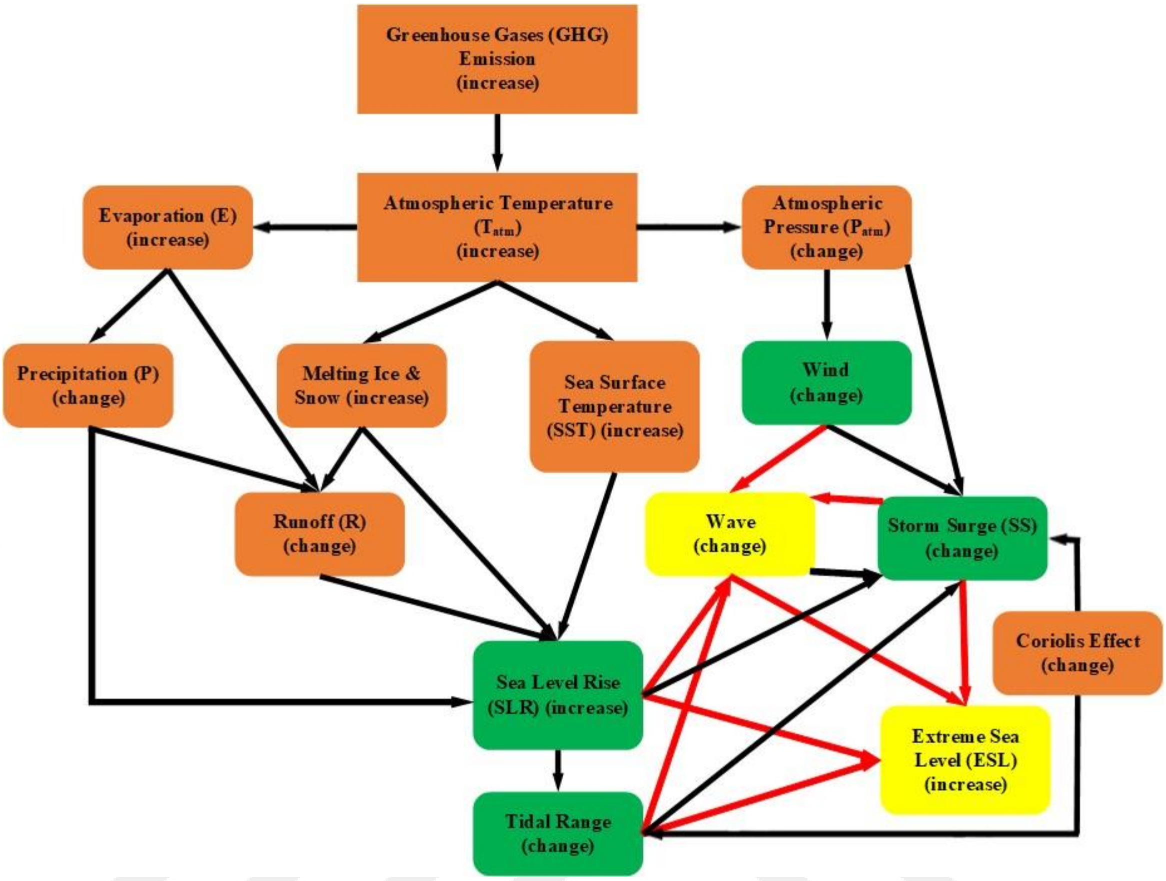

Figure 1.2. The climate change process chart (Orange, green, and yellow boxes represent the indirect input, direct input, and output variables of this study, and black and red arrows represent the relations that are analyzed in the previous studies and this study, respectively.).

1.2.2. Regional Sea Level Changes

Regional sea level (RSL) changes result from spatial variations in the climate, vertical land movements, and melting ice mass redistributions (IPCC, 2019). While examining local climate change impacts, RSL should be taken into account. In this regard, it is important to use regional circulation models (RCMs) instead of GCMs to account for the location dependency. That is because GCMs have insufficient resolutions and cannot capture the regional features as accurately as RCMs for RSL change studies. Therefore, many studies have used multiple methods to achieve a high-resolution RSL analysis. Cui et al. (1995) studied a statistical downscaling method to obtain RSL changes and applied it to the Japanese Islands. The results showed that better model resolutions and regional considerations are significant to local studies. Using a dynamical downscaling method, Olbert et al. (2012) highlighted the importance of high-resolution global and nested regional models. Slangen et al. (2023) highlighted the importance of accounting for distinct regional contributions, such as ocean mass redistribution and steric changes, when producing accurate sea-level projections, reinforcing the need for physically resolved models in coastal-scale assessments. Wang et al. (2025) reconstructed long-term sea level changes and showed that regional variability is strongly influenced by large-scale climate patterns, emphasizing the importance of considering regional climate signals when evaluating sea level trends.

Some studies have also examined the local effects at the country scale. Johansson et al. (2014) combined large-scale and local SLR, including vertical land movement and melting ice mass, to assess the Finnish mean sea level (MSL) scenarios. Brunnabend et al. (2015) and Brunnabend et al. (2017) investigated changes in extreme RSL due to ocean mass distributions and local steric effects, including thermal and salinity effects. They found that worldwide ocean mass distributions were almost uniform, whereas steric effects varied significantly in different coastal regions, showing the impacts of regional features. Carvalho and Wang (2019) studied the sea level changes in the Indian Ocean and coastal flooding due to global warming. Sea surface temperature, air temperature, and vertical land movements were considered. They used a statistical method and a bathtub model to assess the RSL changes and inundation mapping, respectively. They did not consider the dynamic nature of the components of coastal flooding because the bathtub model works by controlling the wet/dry state of the land area. Gonzalez et al. (2025) further dissected regional sea-level trends in the Mediterranean by decomposing steric and dynamic components, revealing that salinity-driven mass changes and circulation patterns significantly influence regional sea-level variability under high-emission scenarios.

All studies have proven that RSL change is more accurate at regional, local, and coastal scales. Thus, while projecting future events and conditions, RSL variations of the study area should be considered rather than the global sea level change.

1.2.3. The Effects of SLR on Extreme Events

While investigating ESL events, wave characteristics, TE, and SS are crucial to estimating total changes in local sea level (IPCC, 2019). Changes in water level and wind pattern affect these hydrodynamic variables (Arns et al., 2015; Vousdoukas et al., 2017), which construct the ESL. Arns et al. (2017) found that waves and storm tides are highly correlated with SLR, especially in shallow coastal areas. They concluded that it is necessary to combine wave characteristics, SS, TE, and sea level anomalies. Boumis et al. (2023) additionally emphasized that present-day 100-year sea level events could occur every 9–15 years globally by mid-century due to SLR, especially under high-emissions scenarios.

In Figure 1.3, the contributors to ESL are shown. SLR affects tidal dynamics because tides propagate as shallow-water waves, which are sensitive to changes in water depth. Changing water depth alters the tidal wave speed (Dean and Dalrymple, 2001; Wilmes et al., 2017; Muis et al., 2020) and modifies basin resonance characteristics (Pickering et al., 2012), which can amplify or dampen tidal amplitudes. Another component of ESL is SS, including wind setup, barometric tide, and Coriolis tide in the order of decreasing contribution percentage. In Figure 1.3, barometric and Coriolis tides are not shown because they have smaller effects compared to the SS and wave setup (Dean and Dalrymple, 2001). Wave setup is separately shown because, depending on the work, SS may not contain the wave setup component. Under hydrostatic (steady-state) and one-dimensional considerations, SS is proportional to the square of the wind speed at 10 m above the sea surface. Assuming monotonically decreasing depth in the shoreward direction, using shallow water asymptote and the spilling breaker assumptions, wave setup is also proportional to the wave height (Dean and Dalrymple, 2001). Hence, one can factor in both global and local impacts by examining coastal flood hazards using ESL. Zhou and Wang (2024) recently highlighted that compound extremes, such as concurrent heatwaves and ESL events, are projected to occur on average 38 days annually by 2049 under high emissions, amplifying risk along densely populated coasts.

There are many studies regarding the aforementioned relations. Albert et al. (2016) studied interplays between the accelerating SLR and wave characteristics in the Solomon Islands. Even though they did not consider the extreme wave cases, they found that wave energy is the key driver of the changes in the Solomon Islands. Vousdoukas et al. (2017) investigated the extreme SLR on the coasts of Europe until 2100. They found the relationships between the MSL, TE, waves, and SS. Also, they assessed extreme SLR by summing these phenomena for different RCP (Representative Concentration Pathways) scenarios. They concluded that the SLR is the key driver, and tides have a negligible effect on a regional scale in Europe. Melet et al. (2018) and Melet et al. (2020) examined the contributions of waves, tides, and atmospheric surges to the long-term SLR variations on the coastal scale. They found that waves have an important amplifying or damping role in the SLR, which depends on the study region. Calafat et al. (2022) further showed that storm surge extremes in Europe have risen at a similar rate as mean sea level, suggesting compound effects need greater attention.

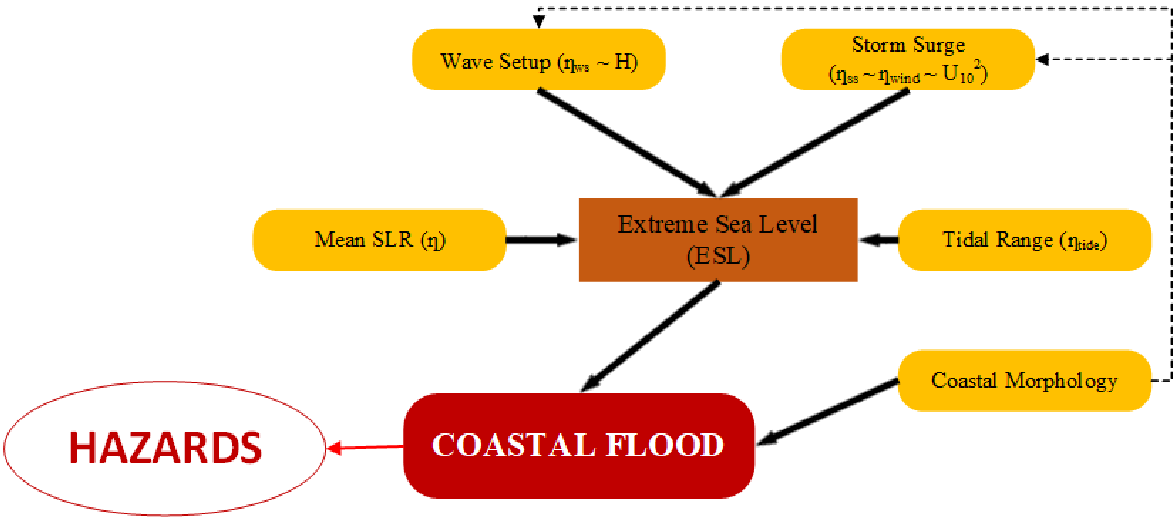

Figure 1.3. The ESL and its variables, which lead to the 'Hazards' component of the IPCC's climate change and socioeconomics processes (IPCC, 2014).

Vitousek et al. (2017) examined the relationship between SLR and the frequency of coastal flooding and found that the frequency of coastal floods can quickly increase with even gradual SLR. To assess this finding, they combined SLR with waves, TE, and SS using the extreme value theory. Erikson et al. (2018) identified the storm events and modeled the future coastal flood using the identified storms and the future total water level. They used the linear superposition method to evaluate the climate change effects on coastal flooding and added up sea level anomalies, wave runups, and SS. Results showed that the same storm causes more severe but rare coastal floods due to the effects of climate change. Kirezci et al. (2020) found that flood-exposed populations could increase by over 50% globally by 2100 due to SLR and extremes, highlighting the need for spatially resolved flood forecasting.

These studies have proven that there are unignorable feedbacks and relationships between the sea level change, wave characteristics, frequencies of extreme events, SS, and TE. These relations should be taken into account when predicting future hydrodynamic events and constructing flood hazard maps.

1.2.4. Coastal Flood Hazard Assessment

As mentioned in the previous section, climate change causes the intensification of hydrodynamic events. In particular, SLR and SS contribute to flood hazards and extreme wave events (Oppenheimer et al., 2019). Future projections of flood hazards have an important role in coastal adaptation and migration. Therefore, predicting these hazards on a local scale is necessary to take measurements on time.

Regarding this concern, there are many studies with different methodologies. Saxena et al. (2013) identified the vulnerable coasts of the Cuddalore region in South India to SLR, SS, and flooding to assess the design life of coastal structures. According to Didier et al. (2015), wave characteristics should be combined with SS to model coastal flooding with good accuracy. Muis et al. (2015) suggested that GCM results can be useful for assessing flood extent on a country scale using probabilistic methods. After reanalyzing global ESL and SS, Muis et al. (2016) generated a global bathtub flood extent map using the linear superimposition of SS, TE, and SLR. Hatzikyriakou and Lin (2017) hydrodynamically examined the structural vulnerability and flood hazard by considering wave effects, flood characteristics, and erosion of dunes. They concluded that their hydrodynamic method for projecting the future flood and erosion works well. Vousdoukas et al. (2018) conducted a future coastal flood risk analysis in Europe. They considered the changes in the sea level, tropical cyclones, and socioeconomic developments. However, wave effects were not taken into account. Maranzoni et al. (2023) provide a recent review of flood hazard classification methods globally, reinforcing the importance of using multi-indicator models (e.g., depth, velocity, duration) to evaluate coastal flood threats.

Aucelli et al. (2018) identified the coastal hazard hotspot areas of the Molise region on the Italian Adriatic coast and predicted SLR, flooding, and erosion for 2065 and 2100. Similarly, Jisan et al. (2018) projected the future SLR impact on SS and mapped the inundation extent on the Bangladesh coast. Lerma et al. (2018) coupled overflow and overtopping processes for the hydrodynamical model of the marine flood. Chtioui et al. (2024) demonstrated that in the Casablanca-Mohammedia coastline, inundated areas could expand by 20.9% by 2100 under combined SLR, waves, and SS influences.

Li et al. (2018) investigated SLR and intensification of the storm in Hawaii until 2100 and probabilistically mapped the inundation hazard. Ballesteros et al. (2018) combined flash floods, marine flooding, and SLR to assess multi-component flood extent at the coast of Maresme in the Northwest Mediterranean and found flash floods as the main disaster for the study area. Gallien et al. (2018) reviewed the coastal flood modeling studies and concluded that the best way to model future coastal flood hazards is an integrated framework combining multiple flooding pathways and marine and hydrological compounds. Almar et al. (2021) emphasized that coastal overtopping hours are increasing faster than sea-level rise, particularly in regions exposed to high-energy wave climates.

Didier et al (2019a) compared two coastal flood maps that were generated using a numerical flood model and a bathtub model, and consequently, the numerical flood model was found to be more accurate. Furthermore, they concluded that the feedback between sea level, wave characteristics, and SS should be included while a multi-hazard analysis is conducted. After that, Didier et al. (2019b) examined the SLR effects and propagation of coastal floods using numerical modeling at Maria coasts in Eastern Canada.

Favaretto et al. (2019) studied the regional-scale coastal flood hazard due to overflow at the Venice coasts and constructed a coastal hazard map. This study assumed negligible advective acceleration using a linearized friction term, which was not suggested in Gallien et al. (2018). Xie et al. (2019) constructed an integrated atmosphere-ocean-coast and overtopping-drainage modeling scheme to assess the coastal flooding map under the SLR case. They concluded that overflow processes should also be included.

Sekovski et al. (2020) developed a coastal vulnerability index and applied it to the Ravenna coast in Italy. SLR and marine flood processes were considered. Idier et al. (2020) combined historical, statistical, and numerical methods to assess coastal flood processes in Gâvres, France. The study site is a macro tidal area and subject to overtopping. The SLR was also included. They indicated that more simulations are needed to assess future flood conditions fully. Muis et al. (2020) presented a novel global dataset of ESL, which is the Coastal Dataset for the Evaluation of Climate Impact (CoDEC), and downscaled this dataset for the Europe region. They concluded that this dataset can be used to investigate climate change impacts at a local scale.

As expressed in these studies, coastal flood hazard assessment is necessary to examine the effects of climate change. Anticipating these hazards can help authorities take action before communities experience economic and social losses.

1.2.5. Necessity for Coastal Hazard Assessments

According to Field et al. (2014), climate change-related risks arise from the relationship between climate change hazards and the exposure and vulnerability of natural systems and humans. These risks depend on time, region, and hazard types. For instance, Laino and Iglesias (2024) established an assessment framework for a wide variety of climate-related hazards, including coastal flooding, sea level rise, and erosion, across diverse coastal cities to prioritize the severity and urgency of their specific risks. For coastal flood hazards, coastal adaptation options consist of the reinforcement of buildings and coastal defense structures, the construction of new defense structures, the definition of a new setback line, and coastal migration. According to a specific region's future risks under climate change, the proper coastal adaptation option should be identified and implemented. Tiggeloven et al. (2020) found that without adaptation, coastal flood damages could increase by a factor of 150 globally by 2080; however, cost-effective adaptation can prevent the vast majority of losses. There are many studies improving the existing adaptation techniques.

Bernatchez and Fraser (2012) studied the reduced resilience to climate change effects due to the reflective nature of coastal defense structures and highlighted that it is important to allow a coast to conserve its natural adjustment skills. They also concluded that hard defense structures are not good for low-lying sandy coasts. Galiatsatou et al. (2018) investigated methods to economically upgrade rubble mound breakwaters under climate change effects and compared these methods with each other. They found the most feasible solution is the placement of a berm at the seaside of the breakwater. Foti et al. (2020)

reviewed the impacts of climate change on coastal defense methods. They listed the techniques that should be applied in order of priority as the upgrade of existing defense structures, the implementation of nature-based solutions, and the integration of traditional and innovative techniques to create antifragile systems. Mentaschi et al. (2020) demonstrated that over 80% of projected flood damages in Europe could be avoided by raising dikes along just 30% of high-risk coastlines, yielding benefit-cost ratios as high as 15:1. Galiatsatou et al. (2021) examined the effects of the ESL, including SLR, waves, TE, and SS, on port defense structures and concluded that the future safety levels and increased vulnerability of the defense structures should be further investigated under climate change effects. Formentin (2021) experimentally examined the hydraulic and structural safety of the upgrade options of coastal defenses, considering changes in sea level and amplified intensity and frequency of extreme weather events. Salauddin et al. (2021) presented the first study about the effects of ecologically modified sea defenses on the dissipation of wave energy and flood hazards, i.e., wave overtopping.

Garland et al. (2010) took into account SLR, waves, tides, and SS resulting from climate change and assessed the vulnerability to shoreline retreat of the nearshore islands of the United Arab Emirates. They tried to establish a safety setback line for these islands and Abu Dhabi to avoid coastal flood hazards and erosion. Lincke et al. (2020) presented the first study about the role of setback zones in future coastal flood hazards and erosion on a regional scale. They concluded that setback zones are an economical and feasible option for coastal adaptation. Furthermore, they suggested that combining coastal defense mechanisms and managed setback zones provides better protection.

Nicholls et al. (2021) gathered the updated projections of SLR and its effects and developed practical methods for coastal adaptation and risk assessment. They suggested that the SLR projections and risk assessment studies should be regularly updated with consideration of previous works. They concluded that a pragmatic approach is the most suitable way to adopt a coastal adaptation method due to today’s uncertainty in the predictions of the future sea level.

Lincke and Hinkel (2021) globally examined the 21st century’s coastal migration using SLR scenarios, discount rates, and socioeconomic conditions. They found that if coastal migration is coupled with the coastal protection techniques by local decision-makers, the global cost to adapt to the SLR can be significantly reduced.

Hinkel and Nicholls (2020) emphasized that the prediction of the response of a coastal adaptation method is crucial to completely assess coastal risk analysis. They stated that there is no absolute way to manage coastal hazards, but being prepared and having some time to implement the method should be deemed important. For this reason, continuous research on climate change and its effects, prediction of coastal hazard risk, and, accordingly, comparison of the options for coastal adaptation and migration are highly significant. Even if climate mitigation measures are stringently applied, there will be SLR for centuries due to the response period of climatic events. Additionally, Rogers et al. (2025) projected that global flood exposure will grow by 300 million people by 2100, largely due to unregulated coastal urbanization; adaptation planning must address both hazards and population trends. This underscores the critical need for hazard-informed development policy.

Thus, although this thesis does not directly investigate adaptation and migration strategies, the reviewed literature clearly demonstrates that rigorous coastal hazard assessments are crucial. Such assessments not only help quantify the risks posed by climate change but also lay the groundwork for informed decision-making in coastal management. In turn, understanding these hazards is essential for shaping any future strategies aimed at adaptation and migration, thereby highlighting the indispensable role of coastal hazard studies in the broader climate change discourse.

1.3. Study Area: Regional Seas of Türkiye

Situated between 30–47°N and 22–42°E, the study region lies at the intersection of six of the 14 CORDEX domains (Figure 1.1a). Although this subregion is not the primary focus of any single domain, it is included in all six, and currently, the EURO-CORDEX domain provides the only available physical ocean data for this area. The region encompasses several key basins—the Black Sea (including the Azov Sea), Marmara, Aegean, and Eastern Mediterranean—which correspond to the northern, northwestern, western, and southern segments of the study area, respectively (Figure 1.1c). This subregion holds significant spatial importance, as it borders 13 countries: Türkiye (TR), Russia (RU), Ukraine (UA), Georgia (GE), Romania (RO), Bulgaria (BG), Greece (GR), Syria (SY), Lebanon (LB), Israel/Palestine (IL/PS), Egypt (EG), and Cyprus (CY). In the analysis, all islands are excluded except Cyprus, with its coasts treated as a single entity that includes both the Turkish Republic of Northern Cyprus and the Republic of Cyprus. For Türkiye, the coastline is subdivided into four distinct segments corresponding to the Black (TR-BS), Marmara (TR-MS), Aegean (TR-AS), and Mediterranean (TR-MED) Seas. At the same time, the coasts of Israel and Palestine are considered together.

The Black Sea is a semi-enclosed basin that connects to the Marmara and Aegean Seas via the Straits of Istanbul and Çanakkale and to the Azov Sea through the Kerch Strait. Covering approximately 461,000 km² (including the Azov Sea) and featuring an 8,350 km long shoreline, its maximum depth reaches 2,588 m (Figure 1.1c), establishing it as one of the largest enclosed basins globally (Akpınar et al., 2012). In contrast, the Marmara Sea, a small inland sea entirely within Türkiye's borders, divides the country's European and Asian parts. It measures roughly 240 km by 70 km, spans an area of 11,500 km², and has a deepest point of 1,270 m (Kutupoğlu et al., 2018). The Aegean Sea, an elongated embayment of the Mediterranean nestled between the Greek and Anatolian peninsulas, extends approximately 670 km in length and 390 km in width, covering around 214,000 km² with depths reaching up to 2,639 m (Figure 1.1c). The Eastern Mediterranean Sea is a semi-enclosed marginal sea connected to the global ocean via the Strait of Gibraltar, bordered by Türkiye, the Greek Dodecanese islands, Egypt, Israel, Palestine, and Syria, and plunges to a maximum depth of 3,310 m (Figure 1.1c).

Türkiye, bordered on three sides by the Mediterranean, Aegean, Marmara, and Black Seas (illustrated in Figure 1.1c), experiences high population densities and intense economic activity along its coasts. This underscores the critical need to assess the impacts of climate change on these surrounding seas. Although several studies have addressed the historical and modeled effects of climate change on the Black Sea coasts (e.g., Alpar, 2009; Aydoğan et al., 2021; Başaran and Güner, 2021; Ceyhunlu et al., 2021; Görmüş et al., 2021), a comprehensive ESL assessment for the coasts of these four seas remains lacking. Considering that hydrodynamic modeling is essential for coastal flood hazard analyses (Gallien et al., 2018), it is imperative to conduct a systematic statistical examination. The Black Sea's high wave energy and extensive river inputs, tourist activities on the

Mediterranean coasts, the intricate geometry of the Aegean coast with its significant tourist activities, and the strategic importance of the Marmara Sea collectively highlight the necessity of such research.

1.4. Objectives and Scope

The main objective of this study is to develop a comprehensive understanding of the future behavior of the regional TWL surrounding Türkiye and its contributors (TE and SS) and ESL in the Black Sea under the influence of climate change until the end of the 21st century. This is achieved by integrating statistical analysis, numerical wave modeling, and coastal flood extent assessments. To this end, the study focuses on three main objectives.

The first objective is the quantitative assessment of TWL and its components. It aims to conduct a detailed statistical analysis of TWL at a subregional scale by decomposing TWL into its main components, SS and TE, using datasets obtained from the Climate Data Store (CDS) (Yan et al., 2020a; Yan et al., 2020b), to understand their contributions and combined effects on coastal hazards. In these datasets, sea level components, including TWL, TE, and SS, are provided based on a modeling framework considering their individual and combined influences. TWL is obtained by simultaneously accounting for TE, SS, and their nonlinear interactions. TE includes barotropic tidal components such as astronomical and radiational tides, self-attraction and loading, MSL, and long-term SLR. While TE and TWL are provided as separate outputs from hydrodynamic simulations, SS is calculated as their difference, thereby implicitly reflecting tide–surge interactions. This objective also aims to identify the most hazard-prone sea among the four regional seas (Black Sea, Marmara, Aegean, and Eastern Mediterranean) through comparative analysis. Particular emphasis is placed on the Black Sea due to its significant SS events and complex hydrodynamic behavior.

The second objective is dynamic shoreline-based numerical wave projection. This objective aims to simulate future wave conditions using a third-generation spectral wave model, SWAN (Simulating Waves Nearshore) (Booij et al., 1999), focusing on the period between 2071 and 2100 (far future) and using statistically analyzed and spatiotemporal

TWL. This component is designed to capture changes in wave characteristics under the influence of climate change and provide key inputs for subsequent analysis.

The third objective is the projection of high-resolution coastal flood extents. First, an established empirical formulation (Stockdon et al., 2006) is used to calculate the high-resolution dynamic shoreline-based wave runup based on simulated wave parameters. This step converts wave projection outputs into wave runup estimates, which are critical for assessing how wave dynamics contribute to coastal ESL. High-resolution ESL projections are then generated by superimposing the statistically analyzed TWL with the empirically derived wave runup values. These ESL forecasts serve as the basis for mapping potential coastal flood extents, providing a robust framework for assessing future coastal flood hazards. This mapping informs coastal hazard assessments and guides decision-making on future coastal flood hazard management and adaptation strategies.

To achieve these objectives, the scope of the study outlines the geographical focus, temporal scale, and methodological integration. The research covers the regional seas of Türkiye, which are located at the intersection of six CORDEX areas. While all four seas (Black Sea, Marmara, Aegean, and Eastern Mediterranean) are considered, the Black Sea is of special interest due to its dynamic SS behavior and significant hydrodynamic interactions. Therefore, wave projection and coastal flood extent are applied for the Black Sea.

The analysis includes historical period (1976-2005), mid-future (2041-2070), and far future (2071-2100) projections, focusing on the far future period for wave projections. This timeframe was chosen to capture the long-term impacts of climate change on coastal systems, and it aligns with the typical design life of major coastal infrastructure, which often spans 50-100 years (e.g., ports, breakwaters, and sea walls).

The study integrates multiple methodological approaches, such as statistical analyses, numerical modeling, and empirical formulations, to produce robust ESL projections. These methods are applied in a sequential framework where outputs from one component inform subsequent analyses (e.g., using wave model outputs to predict wave runup).

While the study provides a comprehensive framework for understanding future coastal hazards, it does not directly address broader adaptation and migration strategies. Instead, the focus is on the development of coastal flood hazard assessments necessary to support subsequent decision-making on adaptation measures.

This integrated approach is designed to bridge the gap between high-resolution local studies and broader climate change impacts and ultimately contribute to improving coastal planning and risk management for the surrounding regions.

1.5. Research Significance and Contributions

This study addresses critical gaps in our understanding of future coastal hazards in regional seas surrounding Türkiye under climate change. As sea levels are projected to rise over time, coastal communities face increasing threats to economic stability, social well-being, and environmental sustainability. However, most existing studies fail to capture the complexities of smaller and regional seas. This research fills this gap by integrating high-resolution statistical analysis, numerical wave modeling, and empirical wave runup calculations with adaptive shoreline-based slope computation to represent coastal dynamics more realistically. Thus, it provides a robust projection of ESL and associated coastal flood hazards.

The main contributions of this study can be summarized as follows: localized and high-resolution analysis, integrated methodological framework, focus on the Black Sea, and implications for policy and adaptation.

As outlined before, focusing on the intersection of six CORDEX areas, namely Europe, Africa, South Asia, Central Asia, Mediterranean, and Middle East North Africa (MENA), this study provides detailed TWL projections at the subregional scale. Such high-resolution data are crucial to accurately assess the localized impacts of climate change on wave properties, SS, and TE, especially for regions that larger-scale models do not adequately represent.

The study combines statistical TWL analysis, numerical wave projections, and empirical wave runup to develop a comprehensive framework for estimating ESL in the Black Sea. In particular, the study introduces an improved first-order estimate of wave runup contribution by dynamically updating shoreline locations and computing corresponding beach slopes at each time step, thereby capturing the spatiotemporal variability of coastal morphology. It also incorporates, for the first time, high-resolution spatiotemporal TWL projections as well as future wind projections in wave projections, updating water depth, spatial differences in sea level, and shoreline, i.e., active nodes, at each computational time step. This integrated approach, called the dynamic shoreline-based approach, increases the reliability of coastal flood hazard assessments and supports better-informed risk management and coastal planning decisions.

While all four seas surrounding Türkiye are considered, the research highlights the Black Sea due to its pronounced SS events and complex hydrodynamics. By identifying the Black Sea as a critical area of concern, the study provides targeted insights that can guide focused adaptation strategies and contingency planning in one of the most vulnerable regions.

Robust ESL projections and detailed flood extent mapping in a GIS (Geographic Information System) environment serve as essential inputs for coastal management and help policymakers develop adaptive strategies that can reduce future risks. This study not only improves our understanding of the mechanisms behind ESL events but also lays the foundation for future studies on adaptation and migration measures, making it highly relevant for regional and international climate policy discussions.

In summary, the significance of this research lies in its ability to bridge the gap between global climate models and local coastal risk assessments. By providing a detailed and integrated analysis of TWL, wave dynamics, coastal flood hazards, and by integrating physically consistent wave runup modeling with high-resolution and dynamically updated topographic inputs, this study provides critical data that form the basis of effective coastal management and adaptation strategies for Türkiye and neighboring countries affected by these regional seas.

1.6. Thesis Outline

This thesis is organized into four main chapters. Chapter 1 introduces the study by outlining the research background, reviewing relevant literature, describing the study area, and defining the objectives and significance of the research. Chapter 2 details the methodology employed, including the statistical analysis of SS, TE, and TWL, numerical wave modeling, empirical wave runup calculations, and the development of coastal flood extent maps. Chapter 3 presents the results of statistical analyses, dynamic shoreline-based numerical wave modeling, empirical wave runup modeling, and coastal flooding. Chapter 4 offers a comprehensive discussion of the results of this thesis, focusing on the interpretation of TWL and SS trends, numerical wave modeling, empirical wave runup modeling, construction of ESL and coastal flood maps, and practical implications of these outcomes for coastal hazard and design. Finally, Chapter 5 concludes the thesis by summarizing the key findings and suggesting directions for future research.

2. METHODOLOGY

This study's methodology consists of three main components: statistical analysis of sea level components, wave projection using numerical modeling, and estimation of wave runup and coastal flood extent. First, CMIP5 (Coupled Model Intercomparison Project Phase 5) RCM outputs developed for the European domain are statistically analyzed to assess future TWL, SS, and TE conditions in the regional seas. Given the distinct oceanographic characteristics of these semi-enclosed seas, this analysis helps determine the most critical region for further investigation, which is identified as the Black Sea. In the second stage, future wave conditions in the Black Sea are simulated using the SWAN model, driven by RCM-derived spatiotemporal TWL, wind data, and detailed bathymetry. Calibration and validation of the model are performed using historical wave reanalysis. Finally, wave runup is estimated along the Black Sea coastline based on projected wave conditions and beach-face slope, applying the empirical wave runup formula of Stockdon et al. (2006) (hereinafter referred to as S06). The combined impact of future TWL and wave runup is utilized to generate a flood extent map in a GIS environment representing extreme coastal inundation conditions. Each methodological step is designed to provide a comprehensive understanding of future coastal hazards under climate change. The methodology is summarized in
Figure 2.1.

2.1. Statistical Analysis of Sea Level Data

This section presents the statistical analysis approach applied to the dataset, beginning with a description of the data sources and progressing through the methods used for comparison across seas and locations. GCMs are among the most reliable tools for projecting future SLR, as they simulate complex atmospheric and hydrological interactions. However, their coarse resolution necessitates further refinement. Hydrodynamic downscaling by scientists worldwide has produced RCMs, which provide higher-resolution outputs. Although both GCMs and RCMs are computationally intensive, their results are publicly available, enabling detailed local and regional analyses

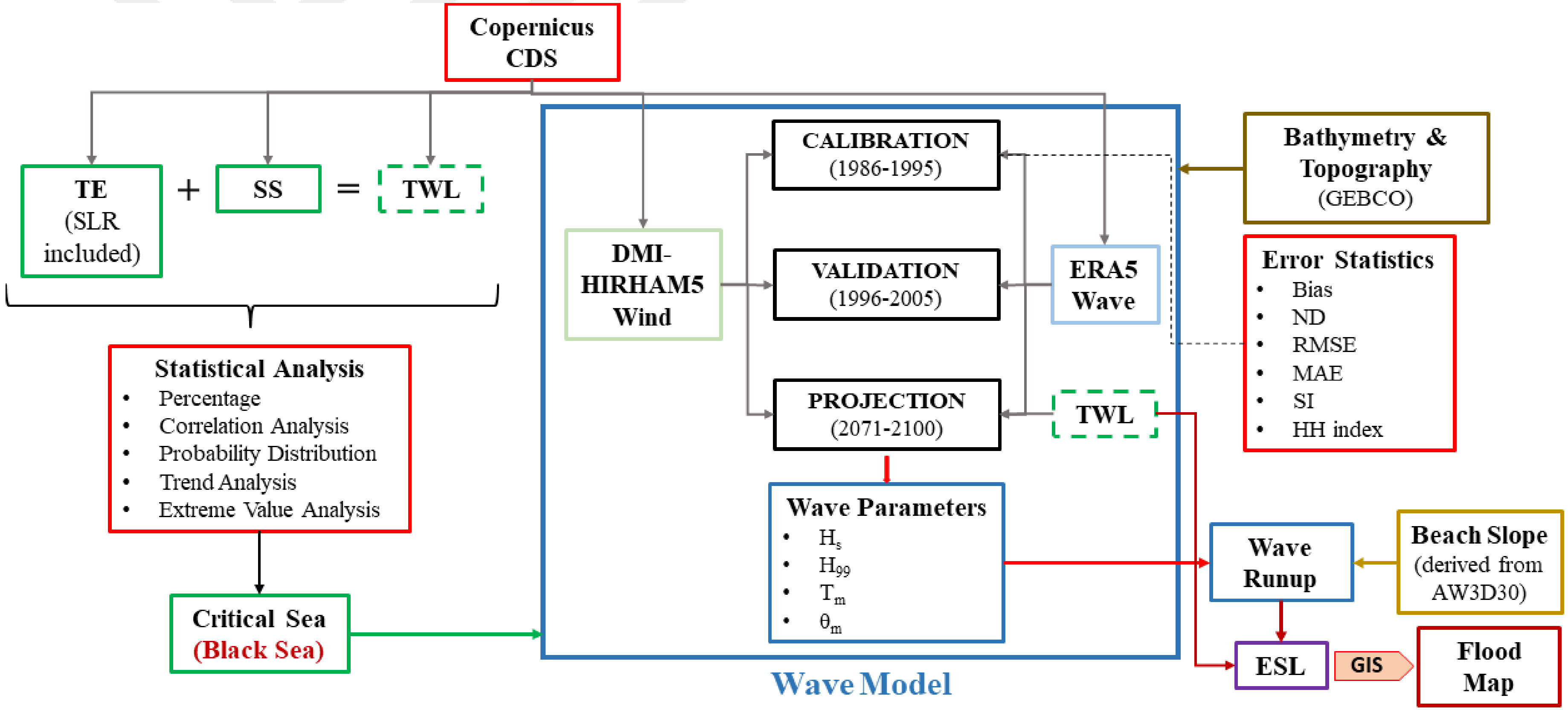

Figure 2.1. Methodology chart.

Given that the regional seas surrounding Türkiye vary significantly in their hydro-morphological and meteorological characteristics from south to north, RCM outputs for the European region (Yan et al., 2020b) are statistically analyzed for Türkiye’s surrounding seas. The key variables examined are TWL, SS, and TE. Comparative analyses of these variables across the seas reveal that the Black Sea exhibits more critical characteristics, making it the focal point for more detailed evaluation and future projections.

For the selected seas, the time series datasets are analyzed in terms of spatial averages, as well as maximum and minimum values, for both 10-minute and annual intervals. For the 10-minute interval data within each sea, the terms "maximum" and "minimum" refer to the highest and lowest values observed across all data points in a given time step. For annual data, these refer to the extreme values observed throughout a simulation year. However, it is important to note that the maximum values obtained by averaging the annual maximums across all locations may not accurately reflect the sea’s worst-case conditions due to the location-specific nature of the data. High values at one point may coincide with low values at another, leading to underestimation when averaged. Therefore, a time series analysis of spatial maximum and minimum values, along with the average, provides a more accurate basis for comparing the future conditions of the seas.

After comparing the seas, further assessments are carried out on extreme value indicators, tidal indicators, and MSL, aiming to explore the changes occurring at each data point and to observe local dependencies, thereby identifying critical coastal areas. These indicators are analyzed over a 30-year end-century epoch to identify extreme conditions and allow observation of localized variations. The extreme value indicators are defined according to their return periods and variable names (e.g., RP1 TWL or RP100 SS), which represent the TWL with a 1-year return period or the SS with a 100-year return period. Subsequently, comparisons are made between the end-century and historical epochs to evaluate how the projected extremes have evolved.

Using data points along the coastlines of countries bordering these seas, the SS distributions are examined based on the 10-minute time series data across three epochs. The RP100 SS and RP100 TWL extreme conditions are also analyzed by comparing the differences between the end-century and historical epochs along the coastlines. A summarizing methodology chart of the statistical analysis section is shown in Figure 2.2.

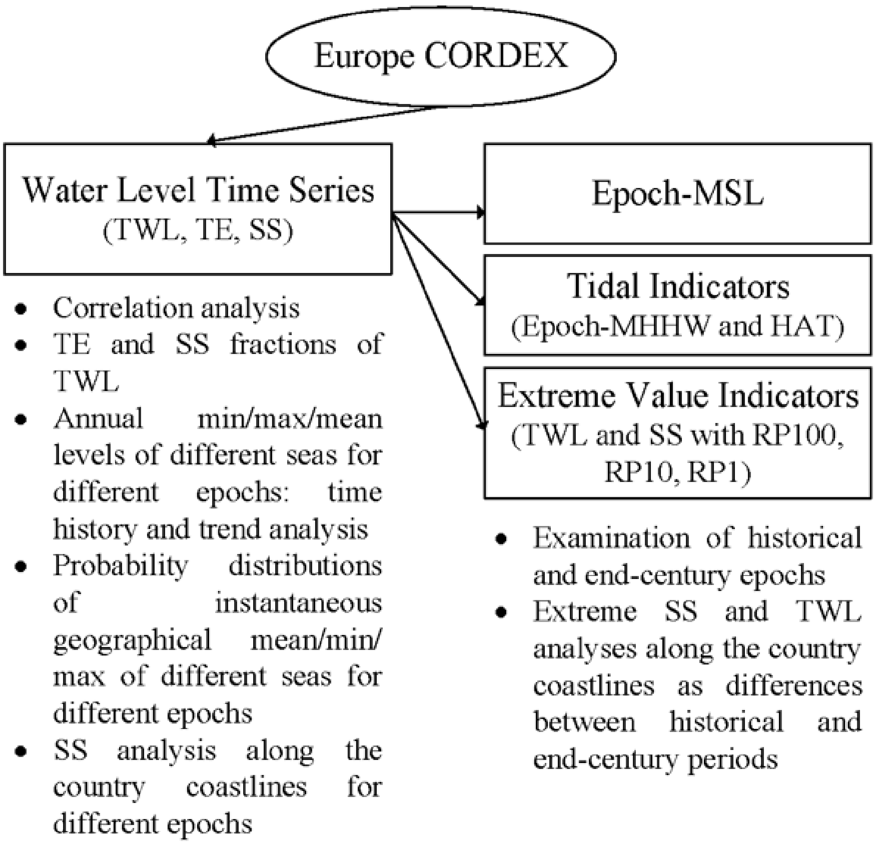

Figure 2.2. The detailed methodology chart of statistical analysis, modified from Uzun and Otay (2025).

2.1.1. Datasets

Two hydrological datasets in the EURO-CORDEX domain were employed to investigate the future climate-induced water level changes in the regional seas of Türkiye. Both datasets were downloaded via the CDS API and cover a broad section of the European coastline, including the four regional seas around Türkiye. These datasets originate from the same hydrodynamic modeling efforts but are presented in two different formats: one as a high-frequency time series and the other as statistical indicators.

The first dataset, "Water level change time series for the European coast from 1977 to 2100 derived from climate projections" (Yan et al., 2020b), includes TWL, SS, and TE data with a 10-minute temporal resolution. These simulations were produced using the Global Tide and Surge Model v3.0 (GTSMv3.0), a barotropic and depth-averaged hydrodynamic model built on Delft3D Flexible Mesh. Due to the flexible mesh, the model uses refined meshes in the Europe region. GTSMv3.0 has 5.0 million grid cells and no open boundaries. Each year is separately simulated. The number of the output locations, including the locations of tide gauges, is 44,734. Forcing fields for the future projections are derived from the EC-EARTH GCM, developed within CMIP5, and the regionally downscaled DMI-HIRHAM5 (Danish Meteorological Institute) model (0.11° resolution) from the EURO-CORDEX initiative. Figure 2.3 shows the generation process of the time series datasets used in this study.

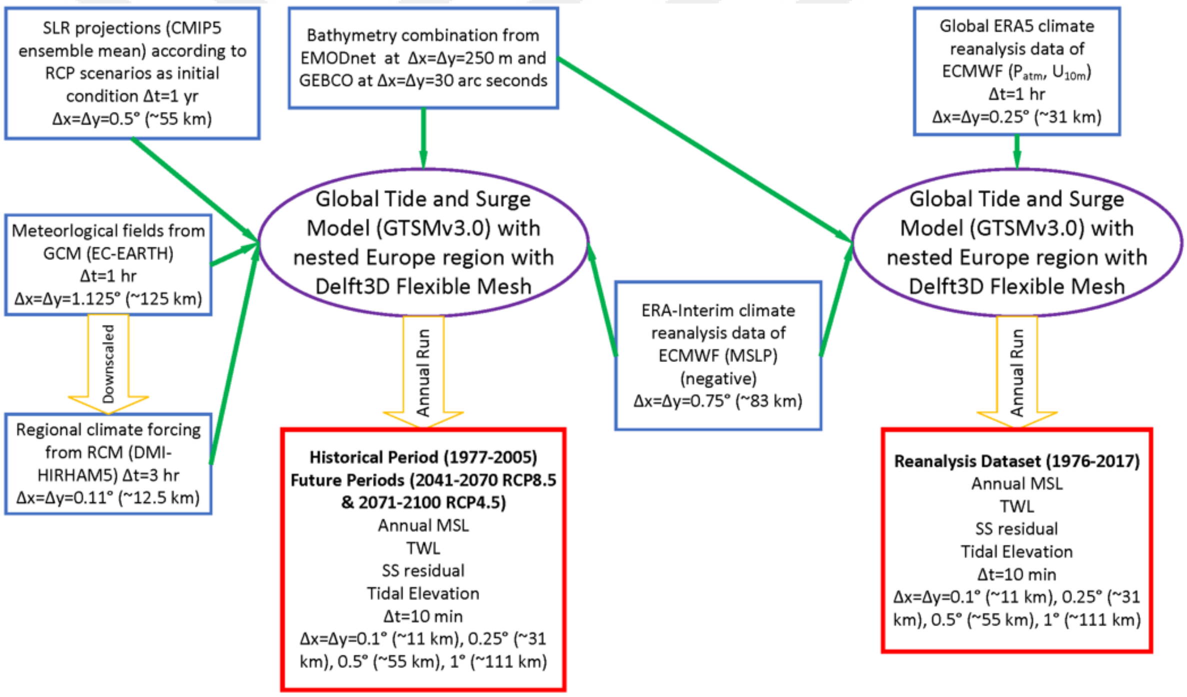

Figure 2.3. Summary scheme of the generation process of the time series datasets of Yan et al. (2020b).

This dataset spans four periods: historical (1977–2005), ERA5 reanalysis (1979–2017), mid-century (2041–2070; under RCP8.5), and end-century (2071–2100; under RCP4.5). Future simulations begin in 2041, as SLR signals require long-term trends to become distinguishable from natural variability. The RCPs are greenhouse gas concentration trajectories developed by the IPCC to explore different climate futures based on varying levels of greenhouse gas emissions. RCP8.5 corresponds to a high-emission scenario with a radiative forcing of 8.5 W/m² by 2100, reflecting continued fossil fuel-intensive development. In contrast, RCP4.5 represents a stabilization scenario where emissions peak around mid-century and then decline, resulting in a lower radiative forcing of 4.5 W/m² by 2100 (IPCC, 2013). The RCP8.5 scenario is used for mid-century because current emissions closely follow this pathway. However, considering international policy efforts such as the Paris Agreement, which aims to limit global temperature change to 1.5°C, the RCP4.5 scenario was selected to reflect a more climate-conscious trajectory for the end-of-century period.

A detailed methodological scheme of the production process of the time series dataset is shown in Figure 2.3. GTSMv3.0's vertical reference level is the MSL, defined according to the average conditions from 1985–2005. To align the model's reference level with that of CMIP5 SLR data, meteorological contributions to the MSL over this baseline period were subtracted from all scenarios using a negative mean sea level pressure field derived from ERA-Interim data.

Within the framework of this model, TWL is obtained by simultaneously considering the effects of SS, TE, and the nonlinear interactions between them. TE includes barotropic tidal effects such as astronomical tides, radiational tides, self-attraction and loading, MSL, and SLR. While TE and TWL are each produced by separate hydrodynamical simulations, SS is calculated as the difference between the two, capturing nonlinear interactions between tides and surges.

The second dataset, "Water level change indicators for the European coast from 1977 to 2100 derived from climate projections" (Yan et al., 2020a), provides tidal and extreme-value metrics including epoch-mean highest high water (MHHW), highest astronomical tide (HAT), and TWL and SS values associated with various return periods. These statistical indicators are derived from the same base simulations as the time series dataset but are processed differently to support coastal hazard assessment.

MHHW is computed by averaging the highest high tides (including MSL and SLR) over each tidal day during the simulated 30-year period. HAT represents the single highest astronomical tide during the same period. TWL and SS with specified return periods are obtained by fitting annual maximum values to a Gumbel distribution.

The spatial resolutions of these two datasets decrease as we go further offshore. For the first 100 km from the coast, the spatial resolution is 0.25°, while for distances between 100 and 500 km offshore, the resolution is 0.5°. Beyond 500 km, the resolution decreases to 1°. These varying resolutions allow for finer details near the coast while maintaining computational efficiency in offshore regions. Additionally, the datasets have been validated by Yan et al. (2020a, 2020b) through comparison with tide measurements to ensure their reliability and suitability for use in local-scale analyses.

2.1.2. Correlation Analysis

Correlation coefficients between TWL and TWL components, SS and TE, are calculated within a 10-year window. A 10-year window is chosen because the decadal period is reasonable for analyzing the climate change effects (Yan et al., 2020b). These analyses are performed between the maximums, minimums, and averages of the 10-minute TWL, SS, and TE data.

2.1.3. TE and SS Fractions of TWL

Fractions of SS and TE to TWL of the four seas are examined in percentages. These analyses are performed with the annual maximum values of these variables for each year between 2041 and 2100. That is, when SS reaches its maximum value, it is calculated as a percentage of TWL. In the same way, it is calculated for the maximum value of TE. It may not make sense to calculate percentages with minimum and average values because, in these cases, the SS data do not always have a positive value; occasionally, it has a reducing effect on TWL.

2.1.4. Trendline Analysis

The trendline analysis of the spatial annual average, maximum, and minimum values of TWL, SS, and TE using a linear least squares regression across the regional seas during historical, mid-century, and end-century periods. The general equation for the linear least squares trendline is expressed as

$$y_i = b_1 x_i + b_0, \tag{2.1}$$

where $i = 1,2, \dots, n$ representing the years, y_i is the corresponding TE, SS, and TWL values, b_1 is the slope, $x_{i,}$ is the year, and b_0 is the intercept. The linear least squares trendline slope and intercept are obtained with the equations

$$b_1 = \frac{n \sum_{i=1}^{n} x_i y_i - (\sum_{i=1}^{n} x_i)(\sum_{i=1}^{n} y_i)}{n \sum_{i=1}^{n} x_i^2 - (\sum_{i=1}^{n} x_i)^2}, \tag{2.2}$$

$$b_0 = \frac{\sum_{i=1}^{n} y_i - b_1 \sum_{i=1}^{n} x_i}{n}, \tag{2.3}$$

respectively (Walpole et al., 2010).

The coefficients and root mean square deviations (RMSD) are calculated for the historical, mid-, and end-century periods to observe the changes in the trends and deviations from the trendlines. The reason for examining the trendlines and RMSD under two future periods is to assess the changes in the maximum and minimum values due to climate change under two different RCP scenarios. The reason for choosing RMSD instead of standard deviation is that standard deviation is useful for calculating the deviations from the mean value of a time series. However, deviations from a trendline can be observed by calculating the difference between the value on the trendline and the actual value at the same time step. RMSD is expressed as

$$RMSD = \sqrt{\frac{1}{n} \sum_{i=1}^{n} |A_i - T_i|^2}, \tag{2.4}$$

where A_i and T_i are the actual and trendline values of the i^{th} year.

2.1.5. Probability Distribution

The probability distributions (PD) of the dataset in the historical, mid-century, and end-century periods are examined as histograms. The average, maximum, and minimum values of the 10-minute interval TWL, SS, and TE data in each sea are used to examine the differences in the PD shapes of the four seas, the changes between the current and future climate, and the moments of the PDs. To achieve that, the statistical moments of the PDs, which are mean (μ), standard deviation (std), skewness, and kurtosis, are examined. The PD moments are examined and expressed as

$$\mu = \sum_{i=1}^{n} x_i / n, \tag{2.5}$$

$$std = \sqrt{\frac{1}{n-1} \sum_{i=1}^{n} (x_i - \mu)^2}, \tag{2.6}$$

$$skewness = \frac{\sum_{i=1}^{n} (x_i - \mu)^3 / n}{std^3}, \tag{2.7}$$

$$kurtosis = \frac{\sum_{i=1}^{n} (x_i - \mu)^4 / n}{std^4}, \tag{2.8}$$

where n is the number of time step and x_i is the actual data.

2.1.6. Tidal Indicators and MSL

The effect of climate change on tidal evolution is still an active area of research. While the full extent of this effect has yet to be fully understood, several factors are known to contribute. Changes in water depth and the resonance properties of ocean basins can have a notable impact on tidal behavior. These changes in tidal characteristics are also reflected in extreme water levels (Yan et al., 2020a). It is important to distinguish between tide-induced and surge-induced changes, as they differ in nature and timescale. Tidal evolutions occur daily and are experienced regularly, whereas extreme SS events unfold over a much longer timescale, spanning multiple years. Additionally, TE tends to exhibit a continuous upward trend, unlike storm-related changes. To evaluate these variations in TE and their regional significance, the epoch-mean MHHW and epoch-maximum HAT values are analyzed in both the historical and end-century periods. Furthermore, the epoch-mean MSL is examined to represent the sea-level changes, excluding the tidal effects.

2.1.7. Extreme Value Indicators

The highest expected water level is important for flood-risk assessments as well as the frequency of this value (Martzikos et al., 2021). It is expected that the extreme values will increase with SLR, and historical extreme values will be reached with milder storms. Furthermore, changes in the frequency and intensity of extreme storms will affect the extreme values of TWL. To observe these changes, extreme-value indicators of the time series data are calculated using the Gumbel distribution over the annual maxima values for the historical (representing current climate), mid-century, and end-century periods (30 years) by Yan et al. (2020a). The extreme value indicators are defined as RP, which describes the severity and likelihood of an event. An increase in specific RP values or a decrease in the frequency of a given extreme value indicates changes in the severity and likelihood of an event. Due to SLR, a general upward shift is expected in the extreme values. In this study, the extreme-value indicators of SS and TWL for the historical and end-century periods and the differences in SS and TWL between these periods are examined, considering 1-year RP (RP1), 10-year RP (RP10), and 100-year RP (RP100). RP1 TWL and SS data are not included in the dataset. Therefore, RP1 datasets are obtained during this study using the Gumbel distribution.

2.1.8. Country Coasts

To analyze SS and TWL along the coastlines of each country, the most shoreward data points from each country's coast are selected. The number of data points included in the country-based analysis is presented in Table 2.1, listed in geographical order.

Table 2.1. The number of data points along the countries' coasts.

	BG	GE	RO	RU	TR-BS	TR-MS	TR-AS	TR-MED	UA	GR	CY	EG	IL/PS	LB	SY
No. of data	27	25	20	74	112	47	107	128	153	189	69	51	11	11	17

The SS box plots, using 10-minute time series data for three different epochs along the countries' coastlines, are examined. These plots allow us to investigate the changes in SS across the three epochs. Additionally, the differences in RP100 SS and TWL between the end-century and historical epochs at these coastal data points are analyzed. When interpreting the extreme values of SS and TWL, the coasts of the Sea of Azov are treated separately from those of the Black Sea due to their distinct outcomes.

2.2. Wave Modeling

In this section, the methodology of the calibration, validation, and wave projection is presented. Calibration, validation, and wave projection processes are conducted in the Black Sea using the SWAN for 1986-1995, 1996-2005, and 2071-2100, respectively. The aim here is to consider the effect of climate change on wave properties while considering the effects of water depth and shoreline changes.

In many wave projections, only wind change is considered (Morim et al., 2019; Casas-Prat and Wang, 2020; Çakmak et al., 2023). However, it is known that water depth has a highly significant effect on wave evolution and propagation. The model used in this study is first calibrated according to the projected wind data. Then, in addition to the wind, spatial and temporal changes of the water level are taken into account at each step, and future wave conditions are projected accordingly. That is, the shoreline is updated at each time step of the model run; in other words, the active nodes (wet nodes or nodes on the sea) have changed at each time step.

This section, which starts with the wave model description, explains the wind and water level data used as input in the model, the model setup, the ERA5 reanalysis data for comparison, calibration, validation, and the methodology of the wave projection. The selection of ERA5 reanalysis data for calibration and validation is supported by the findings of Çakmak et al. (2022), who demonstrated that ERA5 performs adequately when compared with both in situ measurements and remote sensing observations.

2.2.1. Wave Model Description

The third-generation SWAN model has been applied to the Black Sea to analyze wave characteristics using various wind data. Originally developed by Delft University of Technology, the model is available on the SWAN website. Its theoretical and numerical foundation is extensively detailed in works by Holthuijsen et al. (1993), Ris et al. (1999), Booij et al. (1999), and Zijlema and Van der Westhuysen (2005). Widely utilized for both regional and global wave modeling efforts, SWAN has been successfully applied in various studies, particularly at regional scales (Akpınar et al., 2016; Bingölbali et al., 2019; Amarouche et al., 2020).

SWAN operates on the action density equation,

$$\frac{\partial(N)}{\partial t} + \frac{\partial(c_x N)}{\partial x} + \frac{\partial(c_y N)}{\partial y} + \frac{\partial(c_\sigma N)}{\partial \sigma} + \frac{\partial(c_\theta N)}{\partial \theta} = \frac{S(\sigma,\theta;x,y,t)}{\sigma}, \tag{2.9}$$

using an Eulerian energy conservation approach, based on linear wave theory (Dingemans, 1997; Whitham and Ting, 1976). Here, N is the wave action density, c_x and c_y are the group velocity components in the x and y directions, c_σ and c_θ are the propagation velocities in σ and θ spaces while $S(\sigma,\theta;x,y,t)$ is the source term accounting for wave generation, dissipation, and non-linear interactions. The source term $S(\sigma,\theta)$ is broken down into several components as

$$S(\sigma,\theta) = S_{in} + S_{wc} + S_{nl4} + S_{bot} + S_{brk} + S_{nl3}, \tag{2.10}$$

representing, respectively: wind input, whitecapping dissipation, non-linear quadruplet interactions, bottom friction, depth-induced wave breaking, and triad wave-wave interactions (Hasselmann et al., 1985; Cavaleri et al., 2007). The six key source terms involved are classified as either deep-water or shallow-water processes: wind input, whitecapping, and quadruplet wave interactions dominate in deep water, whereas bottom friction, depth-induced breaking, and triad interactions govern shallow-water dynamics. Further details are provided in the SWAN user manual (SWAN Team, 2024).

The wind characteristics at 10 meters above sea level drive wave generation in the SWAN model, with the linear and exponential wind input formulation

$$S_{in}(\sigma,\theta) = A + BE(\sigma,\theta), \tag{2.11}$$

where $E(\sigma,\theta)$ is the energy density spectrum. The linear growth (A) follows Cavaleri and Rizzoli (1981), while the exponential growth (B) depends on wind energy transfer described by Pierson and Moskowitz (1964). The linear growth is expressed as

$$A = \frac{1.5x10^{-3}}{2\pi g^2}\left(U_* max[0, \cos(\theta - \theta_\omega)]\right)^4 H, \tag{2.12}$$

$$H = exp\left\{-\left(\frac{\sigma}{\sigma_{PM}^* x 28U_*}\right)^{-4}\right\}, \tag{2.13}$$

$$\sigma_{PM}^* = \frac{0.13g}{28U_*}2\pi, \tag{2.14}$$

where θ_ω, H, σ_{PM}^*, U_* and σ are the wind direction, filter, peak frequency of the fully developed sea state according to (Pierson and Moskowitz, 1964), friction velocity, and relative radian frequency, respectively.

The exponential growth formulation can vary according to different formulations such as Komen et al. (1984) and Janssen (1989, 1991). Their formulations are shown as

$$B = max\left[0{,}0.25\,\frac{\rho_a}{\rho_\omega}\left(28\,\frac{U_*}{c_{ph}}cos(\theta-\theta_\omega)\right)-1\right]\sigma, \qquad (2.15)$$

$$B = \beta\,\frac{\rho_a}{\rho_\omega}\left(\frac{U_*}{c_{ph}}\right)^2 max[0, cos(\theta-\theta_\omega)-1]^2\sigma, \qquad (2.16)$$

where ρ_a and ρ_ω air and water densities, respectively. c_{ph} and β are the phase speed and Miles constant. N is the action density.

Whitecapping dissipation in the SWAN model is controlled by wave steepness. As outlined by WAMDI group (1988), the formulation of the whitecapping source term is defined as

$$S_{wc}(\sigma,\theta) = -\Gamma\tilde{\sigma}\,\frac{k}{\tilde{k}}\,E(\sigma,\theta), \qquad (2.17)$$

where Γ is the wave steepness-dependent coefficient k, $\tilde{k}$, and $\tilde{\sigma}$ are wave number, mean wave number, and mean frequency, respectively.

In SWAN, the value of Γ is determined by the selected wind input formulation, as it is derived by ensuring the closure of the wave energy balance under fully developed conditions (Booij et al., 1999). The formulations are

$$\Gamma = \Gamma_{KJ} = C_{ds}\left[(1-\delta)+\delta\,\frac{k}{\tilde{k}}\right]\left(\frac{\tilde{s}}{\tilde{s}_{PM}}\right)^p, \qquad (2.18)$$

$$\tilde{s}_{PM} = \sqrt{3.02x10^{-3}}, \qquad (2.19)$$

where C_{ds}, δ and p are tunable coefficients. $\tilde{s}$ is the overall steepness and $\tilde{s}_{PM}$ is the the value of $\tilde{s}$ for the Pierson-Moskowitz spectrum (Pierson and Moskowitz 1964).

Modifications to the tunable coefficient C_{ds} result in adjustments to both the steepness-dependent coefficient and the dissipation rate associated with whitecapping. Initially, the parameter Γ was introduced following Komen et al. (1984). Subsequently, an adaptation by Günther et al. (1992), based on Janssen (1991), was incorporated. Consequently, multiple alternative whitecapping formulations have been implemented in the SWAN model, including the approach by Alves and Banner (2003), which is grounded in experimental research. These findings suggest that whitecapping dissipation is linked to the nonlinear hydrodynamics within wave groups. This formulation is employed in conjunction with a wind input term derived from Yan's expressions (Yan, 1987; Van der Westhuysen, 2007).

SWAN is versatile; it simulates wave generation, propagation, and dissipation while accounting for processes such as depth- and current-induced refraction, shoaling, bottom friction, triad and quadruplet nonlinear wave-wave interactions, depth-induced wave breaking, and whitecapping dissipation. Additionally, SWAN supports wave computations on regular, curvilinear, or unstructured grids within spherical or Cartesian coordinate systems (Zijlema, 2010). The SWAN model produces both one-dimensional and two-dimensional wave spectra, along with various wave parameters, including spectral significant wave height, spectral wave period, wave direction, and directional spreading.

2.2.2. RCM Wind and TWL Data

The outputs of GCMs are central to the CMIP experiments, conducted under the auspices of the World Climate Research Programme (WCRP). The application of RCMs for dynamically downscaling regional climates has become increasingly prevalent due to their enhanced resolution and detailed representation of processes (Rummukainen, 2009).

The EURO-CORDEX RCMs represent outputs from dynamic downscaling experiments based on CMIP5 GCMs (Taylor et al., 2012), contributed by 36 modeling groups. These simulations are initialized using boundary conditions derived from coarse-resolution GCMs and apply dynamic downscaling techniques to resolve regional-scale climate features based on RCP scenarios (Vautard et al., 2013; Moss et al., 2010). More detailed descriptions and information about the EURO-CORDEX RCM experiments can be found in Kotlarski et al. (2014).

In this study, DMI-HIRHAM5 RCM wind and TWL data produced by the WCRP EURO-CORDEX initiative are used to project the future wave climate in the Black Sea. The wind data are the near-surface u and v components at 10 m height with a spatial resolution of 0.11° (~12.5 km) and a temporal resolution of 6 hours, dynamically downscaled using ICHEC-EC-EARTH (Ireland) by DMI (Denmark) as one of the experiments of the EURO-CORDEX initiative. The data are obtained from Copernicus C3S - CDS (Copernicus Climate

Change Service, 2019) using the CDS API. The wind data are extracted for the periods 1986–2005 (historical period) and 2071–2100 (future period). Wind data under the RCP4.5 scenario is used for the future period.

The selection of DMI-HIRHAM5 wind data is primarily motivated by its consistency with the regional water level dataset produced by the same experimental group using the same atmospheric data. Most importantly, no alternative regional water level dataset exists. Furthermore, the water level data has high temporal and spatial resolution. Since the regional TWL data for the period 2071–2100 is available under the RCP4.5 scenario, the DMI-HIRHAM5 wind data were also extracted for the same scenario. The TWL variable of the water level dataset is used, and the details are given in the Datasets section of this thesis. Although this dataset originally had a 10-minute temporal resolution, it is utilized in wave simulations at an hourly resolution to reduce computational costs and manage data storage limitations. Specifically, data points are extracted from the original dataset at 6-hour intervals between 2071 and 2100. More information about the regional TWL data can be found in Yan et al. (2020b).

2.2.3. Model Setup

In this study, version 41.45AB of the SWAN model is utilized to conduct wave climate simulations for the entire Black and Azov Seas region. The computational grid system, a regular rectangular grid, spans from 27°E to 43°E in longitude and from 40.7°N to 48°N in latitude, with a spatial resolution of 0.08°×0.08° and comprising 201x92 grid points. The spectral domain is discretized into 35 frequency bins, logarithmically spaced between 0.04 Hz and 1 Hz, and divided equally into 36 directional bins. The numerical scheme BSBT (first-order upwind, Backward Space Backward Time) is employed for its stability and efficiency in handling wave dispersion.

Bathymetric data for the model domain is sourced from the General Bathymetric Chart of the Oceans (GEBCO, 2024) with a resolution of 15 arc-seconds (~450 m), ensuring accurate depth representation across the entire domain. The SWAN model is driven by the wind data, DMI-HIRHAM5, from CMIP5 RCMs and operated in a non-stationary mode with a 1-hour time step and 1 iteration per time step, utilizing the STOPC convergence criterion, which requires 99% of active grid points to reach convergence. Water level data for the future wave projections is obtained from the statistically analyzed TWL, containing SLR, TE, and SS, and is created with the input data from DMI-HIRHAM5 RCM.

According to the findings of Amarouche et al. (2021), the Komen et al. (1984) formulation is used for wind-wave growth and whitecapping source terms. Different values of the tunable parameter (C_{ds2}) are examined in the calibration process as discussed in the following section. Since the calibration of the SWAN model using DMI-HIRHAM5 wind is found successful and the main focus is to project the wave climate using spatial and temporal water level change in the far-future period, calibration was not further refined.

The default source term formulations in SWAN version 41.45AB are applied for the remaining components. Nonlinear four-wave interactions (S_{nl4}) are approximated using the Discrete Interaction Approximation (DIA) of Hasselmann et al. (1985), with parameters $C_{nl4} = 3x10^7$ and $\lambda = 0.25$. Bottom friction (S_{bot}) is modeled using the JONSWAP formulation of Hasselmann et al. (1973) with $C_{fric} = 0.038$ m^2s^{-3}. Nonlinear triad interactions (S_{nl3}) are represented using the Lumped Triad Approximation (LTA) method by Eldeberky (1996) with parameters $tr_{fac} = 1.0$ and $cut_{fr} = 2.5$. Depth-limited wave breaking (S_{brk}) was incorporated using the bore-based model of Battjes and Janssen (1978), with $\alpha = 1$ and $\gamma = 0.73$.

2.2.4. ERA5 Reanalysis Data

ERA5, the fifth-generation reanalysis produced by the European Centre for Medium-Range Weather Forecasts (ECMWF), provides global climate data and serves as the evaluation reference for the DMI-HIRHAM5 RCMs. ERA5 utilizes an advanced data assimilation system (4D-Var) along with the Integrated Forecast System (IFS) cycle 41r2 (ECMWF, 2016). Compared to its predecessor, ERA-Interim, which had a spatial resolution of 79 km and a temporal resolution of 6 hours, ERA5 offers improved temporal resolution with hourly wave data available from 1940 to the present (Çakmak et al., 2022).

A significant enhancement in ERA5 is the inclusion of uncertainty estimation through an ensemble data assimilation (EDA) system. The EDA system consists of 10 independent assimilations with a reduced resolution of 63 km. These assimilations differ due to variations in physical parameterizations, observational uncertainties, and sea surface temperature conditions (Isaksen et al., 2010). This EDA system allows for uncertainty quantification in reanalysis products (Hersbach et al., 2020).

The CDS system has the hourly ERA5 data with 0.25° × 0.25° spatial resolution for the atmospheric variables and 0.50° × 0.50° spatial resolution for the wave parameters. (Copernicus Climate Change Service, 2019; Hersbach et al., 2023). Three wave parameters which are significant wave height (H_s), mean wave period (T_m), and mean wave direction (θ_m) are obtained from the CDS with a spatial resolution of 0.5° for the historical period (1986-2005) to calibrate the wave model and evaluate the calibrated wave model as ERA5 wave data was found suitable for calibration and evaluation after several studies (Hersbach et al., 2020; Bellotti et al., 2021; Çakmak et al. 2022; Liu et al., 2022; Zhai et al., 2023).

2.2.5. Calibration and Validation

The wind-wave growth and whitecapping source terms are usually identified as the primary focus of model calibration for physical processes (Akpınar et al., 2012; Kutupoğlu et al., 2018; Amarouche et al., 2021; Lei et al. 2023). Amarouche et al. (2021) conducted sensitivity analyses on the Black and Azov Seas using various wind input and whitecapping formulations, adjusting C_{ds2} to optimize the model performance. They found that the most accurate simulation was performed with the Komen scheme for wind input and whitecapping formulations on the Black Sea region by forcing the wave model with ERA5 wind data. Since the ERA5 wave data are utilized to compare the wave model results in this study, following Amarouche et al. (2021), the Komen-Komen scheme is used for wind-wave growth and whitecapping source terms.

Whitecapping remains one of the least comprehended physical processes in wind wave modeling and serves as an adjustable parameter for calibrating wind wave models (Pallares et al., 2014; Cavaleri et al., 2018). Adjusting the coefficient associated with wave dissipation due to whitecapping, C_{ds2}, can address the common underestimations and/or overestimations of wave parameters in simulation models.

This research analyzed five C_{ds2} values of 0.8E-5, 2.36E-5 (default), 3.0E-5, 3.5E-5, and 4.0E-5 which are in the range studied in the literature for the calibration of C_{ds2} (Sun et al. 2022) within the framework of the Komen scheme governing wind input and whitecapping formulations to calibrate the wave model to the DMI-HIRHAM5 winds. For these five C_{ds2} values, the results of the wave models performed for 10 years between 1986 and 1995 are compared with ERA5 wave data considering H_s, T_m, H_{99}, and θ_m wave parameters (Table 2.2) and the model with the best results is selected for the validation of the calibrated wave model using an unweighted normalized decision matrix.

Table 2.2. SWAN model setup for calibration, validation, and projection.

	Calibration	**Validation**	**Projection**
Time period	1986-1995	1996-2005	2071-2100
Temporal resolution	1 hr	1 hr	1 hr
Spatial resolution	0.08°x0.08°	0.08°x0.08°	0.08°x0.08°
Wind source term	Komen	Komen	Komen
Whitecapping source term	Komen	Komen	Komen
$\boldsymbol{C_{ds2}}$	0.8E-5, 2.36E-5, 3.0E-5,	4	4
Wind data	EC-EARTH DMI-HIRHAM5		
Wind spatial resolution	0.11°x0.11°		
Wind temporal resolution	6 hr		
Wave data for evaluation	ERA5 Reanalysis		-
Wave spatial resolution	0.5° x 0.5°		-
Wave temporal resolution	1 hr		-
Bathymetry source	GEBCO (15 arc-seconds)		
Bathymetry resolution	0.004167° x 0.004167° (15 arc-seconds)		
TWL Source	-	-	DMI-HIRHAM5
Wave parameters	Annual means of H_s, H_{99}, T_m, θ_m		
Statistical parameters	Bias, RMSE, MAE, HH index, SI, ND		-

The performance of the DMI-HIRHAM5 wave climate simulations under present climate conditions is comprehensively assessed through comparisons with ERA5 data. Hourly wave simulations and ERA5 reanalysis are used to derive annual and seasonal means of H_s as well as annual means of T_m, θ_m, and H_{99} which is the 99th percentile of the SWAN model output (representing the extreme values of H_s) and ERA5 reanalysis. The seasons are categorized as December-January-February (DJF), March–April-May (MAM), June-July-August (JJA), and September-October-November (SON) for winter, spring, summer, and autumn, respectively. In the SWAN wave simulations, H_s, T_m, and θ_m represent the significant wave height, mean absolute (zero-crossing) wave period, and mean wave direction, respectively. θ_m is identified relative to the x-axis of the Cartesian coordinate system and positive in the counterclockwise direction. H_s and T_m are defined as

$$H_s = 4\sqrt{m_0}, \tag{2.20}$$

$$T_m = \sqrt{m_0/m_2}, \tag{2.21}$$

where m_0 and m_2 are zeroth and second moments of the energy density spectrum, respectively.

The comparison approach employed in all analyses involves an initial presentation of the mean values for the relevant parameters derived from the ERA5 data. Following this, the differences between each calibration model's parameters and those of the ERA5 data are analyzed. To ensure consistency in the comparison, the wave climate simulations, originally conducted at a resolution of 0.08°, are upscaled to match the 0.5° resolution of the ERA5 dataset.

This study presents the statistical error metrics employed to spatially evaluate SWAN model outputs against the ERA5 data. Commonly used error statistics are computed to assess the performance of wind wave models. These include bias, normalized difference (ND) in percentage, root mean square error (RMSE), scatter index (SI), mean absolute error (MAE), and normalized RMSE-type metric, known as the HH index. They are primarily used to identify systematic errors, measure data accuracy, and analyze relative errors to determine whether the models tend to overestimate or underestimate the simulated parameters compared to the benchmark data.

HH index (Hanna et al., 1985) is included since it is unbiased toward simulations that underestimate or overestimate averages and is not influenced by the mean of the benchmark data. Mentaschi et al. (2013) also strongly recommended its use for evaluating wind wave models. Using M_i for the modeled values, $\bar{M}$ for the mean of modeled data, B_i to represent the benchmark data values, $\bar{B}$ for the mean of observed data, and N for the total data number,

$$bias = \bar{M} - \bar{B}, \tag{2.22}$$

$$ND = \sum_{i=1}^{N} \left(\frac{M_i - B_i}{B_i}\right) x100, \tag{2.23}$$

$$RMSE = \left[\frac{1}{N}\sum_{i=1}^{N}(M_i - B_i)^2\right]^{1/2}, \tag{2.24}$$

$$MAE = \frac{1}{N}\sum_{i=1}^{N}|M_i - B_i|, \tag{2.25}$$

$$SI = \frac{RMSE}{\bar{B}}, \tag{2.26}$$

$$HH = \sqrt{\frac{\sum_{i=1}^{N}(M_i - B_i)^2}{\sum_{i=1}^{N}(M_i x B_i)}} \tag{2.27}$$

are applied to H_s, H_{99} and T_m wave parameters to compute the error metrics.

The shortest angular distance (Δ) between the mean wave directions of the SWAN output and the ERA5 dataset is used to evaluate the θ_m parameter of the SWAN output. Positive contour values are clockwise deviations from the ERA5 θ_m while negative values correspond to counterclockwise deviations. This approach helps in identifying and analyzing directional discrepancies between the model outputs and the benchmark dataset.

After the wave model is calibrated, it is forced with the same wind data for 10 years between 1996 and 2005 to evaluate the calibrated model using the C_{ds2} value that gives the best agreement with the ERA5 reanalysis data according to an unweighted normalized decision matrix. The model results are compared with ERA5 wave data considering the wave parameters H_s, T_m, and θ_m as in the calibration process.

2.2.6. Wave Projection

Wave simulations in the future climate for 30 years from 2071 to 2100 (FW30) are performed using DMI-HIRHAM wind forcing with a temporal resolution of 6 hours, TWL with a temporal resolution of 1 hour, and bathymetry including topography data from GEBCO (Table 2.2). The TWL data, which originally had an unstructured grid, is interpolated on a 0.1° x 0.1° structured grid. This is suitable due to the high resolution of the TWL data in the nearshore area.

A key methodological advancement of this study is the integration of spatially distributed TWL data and the dynamic updating of active computational nodes in SWAN at every time step. This feature allows the model to reflect temporal changes in shoreline and inundation extent under projected sea level rise. While most existing wave projections assume static bathymetry and shoreline conditions, this approach accounts for dynamically evolving coastal topography, thereby offering improved accuracy in nearshore wave forecasts. Moreover, the inclusion of wet/dry transitions enables a preliminary identification of flooded areas before transferring the data to a GIS environment for detailed flood analysis. This method strengthens the physical consistency of wave-runup and flood impact estimations in the context of future coastal hazards.

Similarly, wave simulations in the present climate for 20 years from 1986 to 2005 (PW20) are performed using DMI-HIRHAM wind forcing. In the initial analysis stage, PW20 simulations are evaluated against ERA5 data during the calibration and validation process. As a second stage, FW30 and PW20 simulations are also compared to examine the impact of climate change on the wave climate towards the end of the 21st century, considering both changes in the wind characteristics and water level. Differences between the period averages of FW30 and PW20 are studied using ND in percentage. This comparison provides quantification of the projected changes.

The FW30 simulations are performed for the same wave parameters, H_s, H_{99}, T_m, and θ_m, as in the calibration and validation processes. Furthermore, spatially distributed projected trends in wave parameters over 2071–2100 are analyzed using the linear least squares regression method at each data point. Thus, the slopes of the predicted changes (cm/year) in annual and seasonal H_s and H_{99} are obtained. Additionally, annual and seasonal spatially distributed projected changes (ND, %) in 10-meter wind speed, U_{10}, of FW30 and PW20, which influence overall wave climate trends, are analyzed.

2.3. Wave Runup and Coastal Flooding

ESL and coastal flood analyses require consideration of wave-induced contributions in addition to sea level changes. Especially in storm conditions, the runup caused by waves reaching the shore significantly increases the water level at the shore, thus increasing the flood probability. Therefore, it is of great importance to integrate wave effects into TWL calculations (Dodet et al., 2019; Melet et al., 2018; Stockdon et al., 2023). Wave runup is a combination of wave-induced setup and time-varying swash components superimposed on a still water level. These components are often ignored or crudely represented by the assumption of constant morphology. However, recent studies (Almar et al., 2021; Kim et al., 2023; Agulles and Jordà, 2024) have discussed that changes in coastal slope and morphology can significantly affect wave runup estimates.

In this study, wave runup along the Black Sea and Azov Sea coasts is calculated based on the empirical formulation of Stockdon et al. (2006), S06, using hourly wave height and wave period data obtained from SWAN wave model outputs. The 2% exceedance wave runup, R_2, is estimated using deep-water H_s, peak wave period (T_p) obtained from the SWAN outputs, and coastal slope (β) for extremely dissipative and intermediate/reflective conditions. These conditions depend on the Iribarren number (surf similarity parameter, ξ). This formulation is also officially accepted by NOAA (National Oceanic and Atmospheric Administration) and USGS (U.S. Geological Survey). It is used in national operational flood and erosion prediction and early warning systems on the US coasts (Stockdon et al., 2023). In the scope of the study, these calculations are applied to the wave projection period between 2071 and 2100.

Unlike the common approaches in the literature, in this study, the coastline is redefined at each time step, and the land boundary is dynamically updated depending on the sea level change. Thus, the current slope value in the land direction for that moment is determined and used in the runup calculation. This method provides a more realistic representation than classical studies assuming the slope and land boundary are fixed. Therefore, the method used is defined as “improved first-order estimate of wave runup” as a more advanced derivative of the first-order estimate approaches in the literature. For slope calculations, the high-resolution AW3D30 (Advanced Land Observing Satellite World 3D - 30m) digital surface elevation dataset developed by the Japan Aerospace Exploration Agency (JAXA) is used (JAXA, 2015). This dataset has a resolution of 30 m and is widely used in global coastal analyses. It is the dataset showing the lowest bias among the six DEMs (Digital Elevation Maps) and has an average margin of error of ~1.5-2 m when compared to LiDAR data (Almar et al., 2021).

The ESL is obtained by superimposition of TWL with R_2 and analyzed with the bathtub approach to determine potential flood areas along the Black Sea coasts. In this approach, the calculated ESL is compared with the AW3D30 dataset; land cells with a surface elevation below this level are classified as potential flood areas. Flood area maps are created in a GIS environment based on the average and RP100 values of ESL.

As a result, the method proposed in this study provides a framework that goes beyond the existing global and regional scale first-order runup estimations in the literature, which estimates wave contribution more precisely by considering the time-varying shoreline, slope variations, and regional wave conditions together. This improved approach, the dynamic shoreline-based approach, provides a significant methodological advance compared to studies based on constant slope assumptions, as it directly reflects the topographic variability present (Gomes da Silva et al., 2020; Melet et al., 2020; Vousdoukas et al., 2017).

2.3.1. Wave Runup Calculation

In this study, wave runup calculations are performed based on H_s and T_p data obtained from hourly SWAN model outputs covering the period 2071–2100. Deep water wavelength (L_0) is derived from T_p value. For each coastal grid point, the seaward direction is determined, and deep-water conditions are taken from the point located 0.08° (~8.88 km) offshore in this direction. The average water depth at this point is approximately 85 m in the Black Sea and can be considered as deep-water condition since it represents wave conditions free from effects such as refraction and island shadowing outside the continental shelf (Erikson et al., 2018).

Area-averaged subaerial slope (β) data are calculated using AW3D30 digital surface elevation. The area-averaged slope is generated by averaging the valid slope values within the 0.01°×0.01° block around each coastal grid point, similar to Almar et. al. (2021). This method may provide a more stable and physically meaningful coastal slope by reducing single-cell errors and representing the general features of the mesh areas of regional and/or global-scale studies.

The Iribarren number (ξ) is calculated with the obtained H_s, T_p, and β values, and the runup formula is selected according to the coast type. If the Iribarren number is low ($\xi < 0.3$), the coast is classified as extremely dissipative and a different formula is applied. In runup calculations, the S06 empirical formulation is used (Gomes da Silva et al., 2020; Stockdon et al., 2023). The S06 formulas are

$$R_2 = 0.043 \sqrt{(H_0 L_0)} \text{ for } \xi < 0.3, \tag{2.28}$$

$$R_2 = 1.1(0.35 \beta \sqrt{(H_0 L_0)} + \sqrt{(H_0 (L_0 (0.563 \beta^2 + 0.004)))}) \text{ for } \xi \geq 0.3, \tag{2.29}$$

for extremely dissipative and intermediate/reflective conditions, respectively. H_0 represents the deep-water wave height. L_0 and ξ are calculated using

$$L_0 = g {T_p}^2 / (2 \pi), \tag{2.30}$$

$$\xi = tan(\beta) / \sqrt{(H_0 L_0)}, \tag{2.31}$$

respectively. Although the S06 formula was initially developed for specific coast types, e.g., low-lying sandy beaches, it is now widely used in global and regional flood analyses (Kirezci et al., 2020; Almar et al., 2021; Collings et al., 2024).

The calculations are made for hourly time steps. The obtained R_2 values are added linearly to the TWL of that time to calculate the ESL, similar to Stockton et al. (2006), Vousdoukas et al. (2017), Melet et al. (2018), Kirezci et al. (2020), Melet et al. (2020), Almar et al. (2021), and Collings et al. (2024). Since the nonlinear processes such as TE, SS, and climate change-induced sea level variations are already included in the TWL with the nonlinear interactions between them, only the wave-induced runup component, R_2, is added linearly in the study. In this way, the integrity of the TWL is preserved, but the missing runup contribution is taken into account.

After calculating hourly R_2 values and ESL for the 2071–2100 period, annual maxima were extracted for each coastal point. To estimate RP100 levels, a Generalized Extreme Value (GEV) distribution was fitted to the annual maxima series of R_2, TWL, and ESL separately. This approach enables consistent comparison across components and aligns with standard practice in coastal hazard studies (e.g., Vousdoukas et al., 2018; Melet et al., 2020).

3. RESULTS

In this section, the results of the statistical analysis of TWL, SS, and TE, wave modeling, wave runup, and coastal flooding are presented. The interconnections among the three modules can be described as follows: the statistical analysis identifies the most critical sea among Türkiye's regional seas and provides the corresponding TWL data, which are used as input for wave modelling. The wave model, in turn, supplies predicted wave characteristics that are utilized in the wave runup and coastal flooding assessments. Finally, coastal flood maps are generated along the coastline of the most critical sea by calculating the wave runup using an empirical formula.

3.1. Statistical Analysis

3.1.1. Time Series Data of the Regional Seas

According to the coordinates of the four seas, the time series datasets are downsized. The latitude and longitude coordinates for the Marmara, Black, Aegean, and Mediterranean Seas are chosen as 40.3°N - 41.0°N and 26.8°E - 29.5°E, 40.2°N - 47.2°N and 27.5°E - 41.9°E, 40.8°N and 22.6°E - 28.1°E, and 30.8°N - 36.9°N and 22.5°E - 36.2°E, respectively. Since the behaviors at all coastal data points should be taken into account when assessing on a country basis, it was decided to determine the coordinates of the four seas as landlocked as possible. Thus, while the Black (including the Sea of Azov), Marmara, and Aegean Seas are all covered, only the eastern part of the Mediterranean is covered. As a result, there are 68, 1068, 1018, and 696 data points covering the Marmara, Black, Aegean, and Mediterranean Seas, respectively (Figure 1.1b).

The 10-minute average and spatial maximum and minimum values of SS, TE, and TWL of the four seas in the mid and end-century periods are examined and shown in Figure 3.1, Figure 3.2, and Figure 3.3, respectively. To find upper and lower peak envelopes in the seas, signal envelope analysis is applied to 10-minute maximum and minimum SS, TE, and TWL data. Envelopes are decided by applying spline interpolation on local maxima separated by at least the peak separation sample. To examine the deviations of the upper and lower envelopes from the average values more clearly, annual sampling is applied by taking the peak separation parameter 52560. The highest deviations in SS and TWL data are observed in the Black Sea, whereas the highest deviations in TE data are observed in the Aegean Sea.

The maximum TWL of the Black, Marmara, Aegean, and Mediterranean Seas until 2100 can reach 3.75 m, 0.66 m, 1.26 m, and 1.65 m, respectively. SS and TE values with the same order are predicted to be 3.41 m, 0.24 m, 0.89 m, and 1.23 m, and 0.64 m, 0.46 m, 0.90 m, and 0.73 m in these seas. The average TE for all seas is approximately 0.4 in 2100, except for the Mediterranean Sea. The TE values in the Mediterranean Sea oscillate between 0.2 and 0.5 m towards 2100. It can be deduced that the primary difference among the four seas is the result of the SS residual.

The time series data are analyzed with correlation, percentages, probability distribution, and trendline studies and discussed in the following sections. These analyses help decide the critical sea and determine which contributor is more important for which sea.

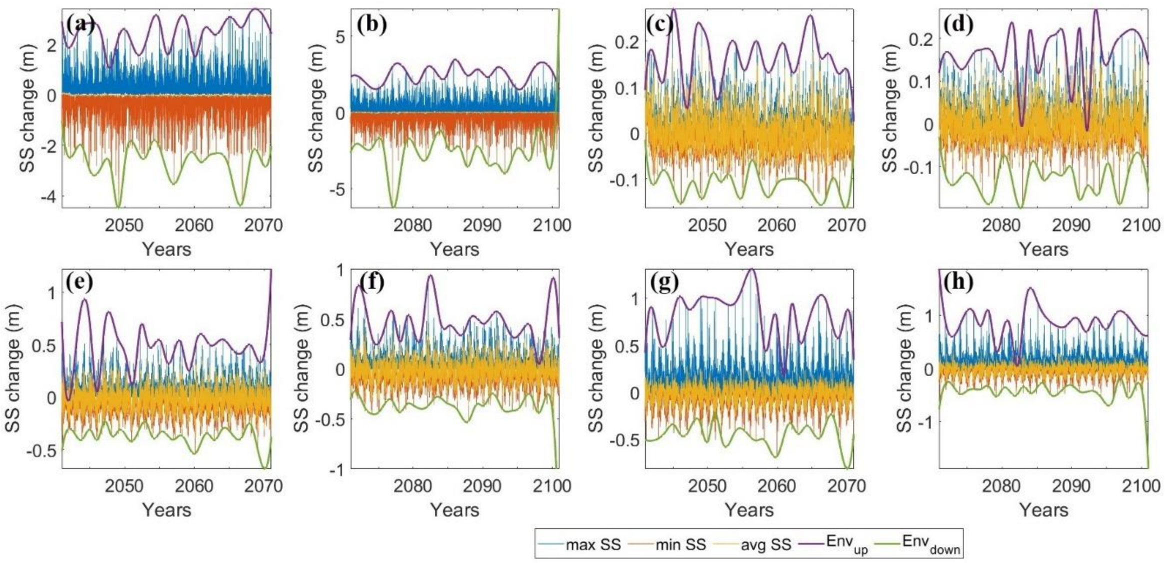

Figure 3.1. The SS and its envelopes of the Black Sea in (a) mid- and (b) end-century, Marmara Sea in (c) mid- and (d) end-century, Aegean Sea in (e) mid- and (f) end-century, and Mediterranean Sea in (g) mid- and (h) end-century periods.

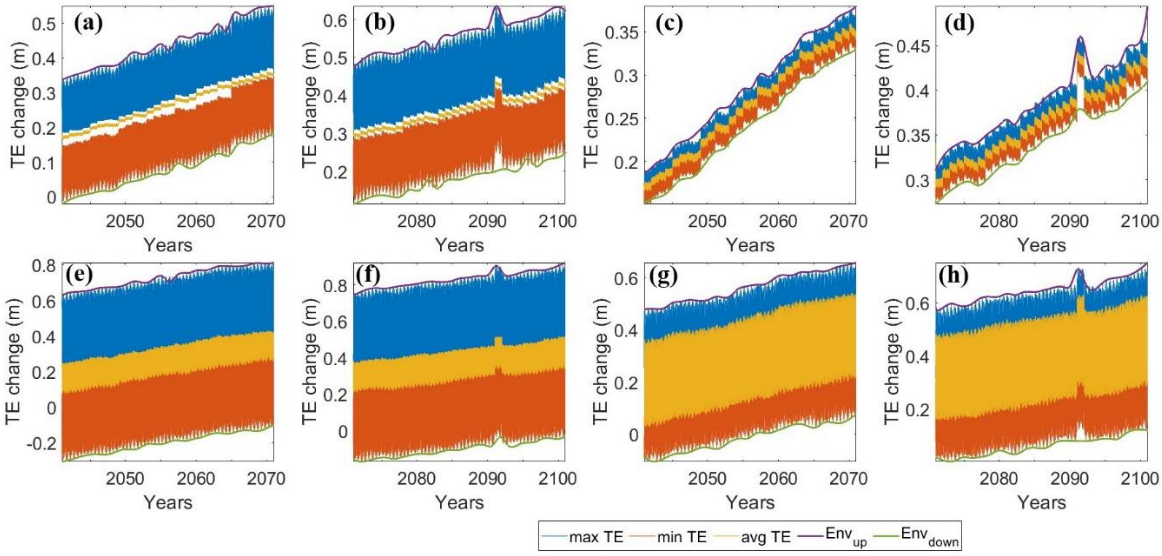

Figure 3.2. The TE and its envelopes of the Black Sea in (a) mid- and (b) end-century, Marmara Sea in (c) mid- and (d) end-century, Aegean Sea in (e) mid- and (f) end-century, and Mediterranean Sea in (g) mid- and (h) end-century periods.

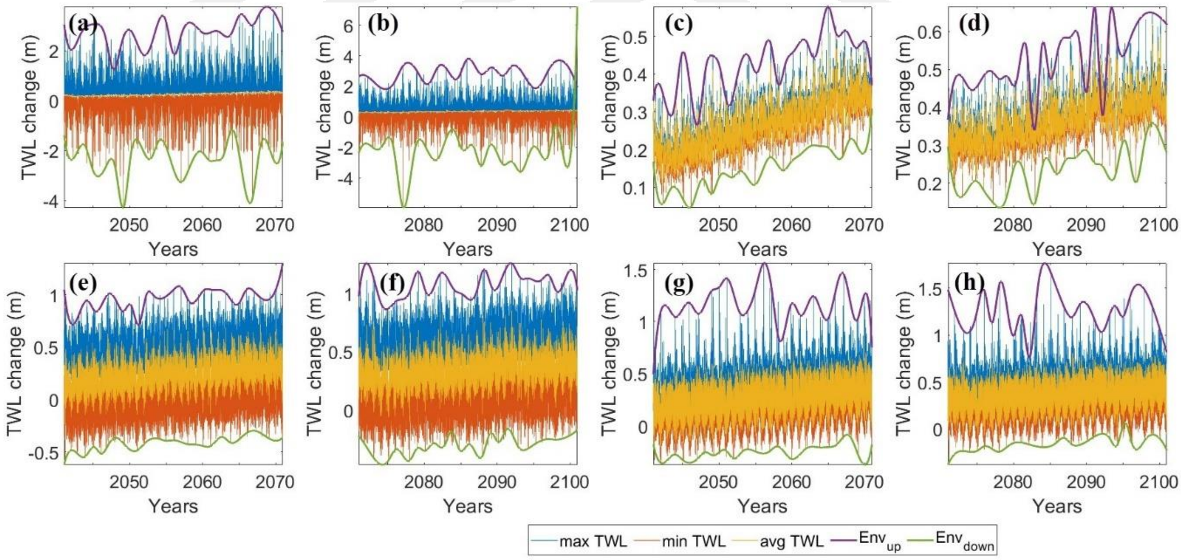

Figure 3.3. The TWL and its envelopes of the Black Sea in (a) mid- and (b) end-century, Marmara Sea in (c) mid- and (d) end-century, Aegean Sea in (e) mid- and (f) end-century, and Mediterranean Sea in (g) mid- and (h) end-century periods.

3.1.2. Correlation Analysis of Time Series Data

Correlation coefficients between TWL and its components calculated within a 10-year window are shown in Figure 3.4. In the Black Sea, the correlation between SS and TWL remains strong across all future periods, except 2061-2070. A Pearson's correlation coefficient of 0.75 or higher is generally interpreted as a strong relationship (Hinkel et al., 2003), and during both extremely high and low conditions, this coefficient approaches ~0.99. In contrast, the correlation between TE and TWL is negligible under maximum and minimum conditions (approximately 0.05), while the mean TE shows a much stronger correlation with TWL (~0.89). These findings indicate that SS is the dominant component influencing TWL during extremes, whereas TE has a greater influence under average conditions. A similar pattern is observed in the Marmara Sea, although the contribution of average TE to TWL is weaker (~0.40), suggesting a relatively minor role compared to SS.

Figure 3.4. Heatmap of correlation coefficients of TWL components with TWL in the (a) Black, (b) Marmara, (c) Aegean, and (d) Mediterranean seas, adapted from Uzun and Otay (2025).

In the Aegean Sea, both SS and TE exhibit strong correlations with TWL, indicating their comparable impact on sea level variability in the region. TE shows a stronger association under extreme conditions (~0.78), whereas SS is more closely related to TWL in average conditions (~0.90). In the Eastern Mediterranean, SS and TE also display similarly strong correlations with TWL (~0.70) across most decadal periods, although under maximum conditions, SS reaches a higher correlation (~0.78) compared to TE (~0.50). A slight upward trend is observed in the maximum TE correlation over time, while the correlation associated with maximum SS decreases marginally.

As illustrated in Figure 3.4, SS demonstrates the highest correlation with TWL in the Black Sea and Marmara Sea, whereas TE is more strongly correlated in the Mediterranean and Aegean Seas. Notably, in the Aegean Sea, TE maintains a stronger correlation than SS even under extreme conditions. In contrast, SS dominates in the Mediterranean Sea during both peak high and low conditions.

The decade spanning 2061-2070 exhibits the lowest TWL correlation values across all sea regions. This drop may be attributed to the transition between RCPs used in the climate projections. Specifically, the period of 2061-2070 corresponds to the terminal phase of RCP8.5, marked by high emissions and rapid climate shifts, while the subsequent decade (2071-2080) aligns with the more moderate RCP4.5 scenario. This shift introduces differences in the projected behavior of TWL, SS, and TE, stemming from distinct emissions trajectories and modeling assumptions. RCP8.5 tends to produce more pronounced and fluctuating impacts, while RCP4.5 reflects a more stabilized climate response. Consequently, this transition likely affects the internal dynamics among these variables and may explain the temporary weakening of their correlations. Furthermore, during that decadal period, while the correlation coefficients of SS decrease, those of TE slightly increase. This may be explained by the dominance of long-term impacts of climate change over its effects on instantaneous events in 2061-2070.

3.1.3. TE and SS Fractions of TWL

The results of the TE and SS fractions of TWL in the regional seas are shown in Figure 3.5. In descending order, the maximum SS percentages to TWL in these seas are as follows: Black, Mediterranean, Aegean, and Marmara Seas with approximate average percentages of 90%, 75%, 50%, and 35%, respectively. This descending order for the maximum TE percentages is Aegean, Marmara, Mediterranean, and Black Seas, with approximate average percentages of 75%, 70%, 50%, and 20%, respectively.

The percentage change over the years shows that the percentage of the maximum TE in each sea is increasing as the water level is predicted to continuously increase due to climate change. The RCP8.5 scenario, 2041-2070, shows more dramatic changes in percentages of both SS and TE for all seas because climate change worsens quickly in this scenario. However, the changes between 2071-2100, the RCP4.5 scenario, are softer as this scenario is more optimistic.

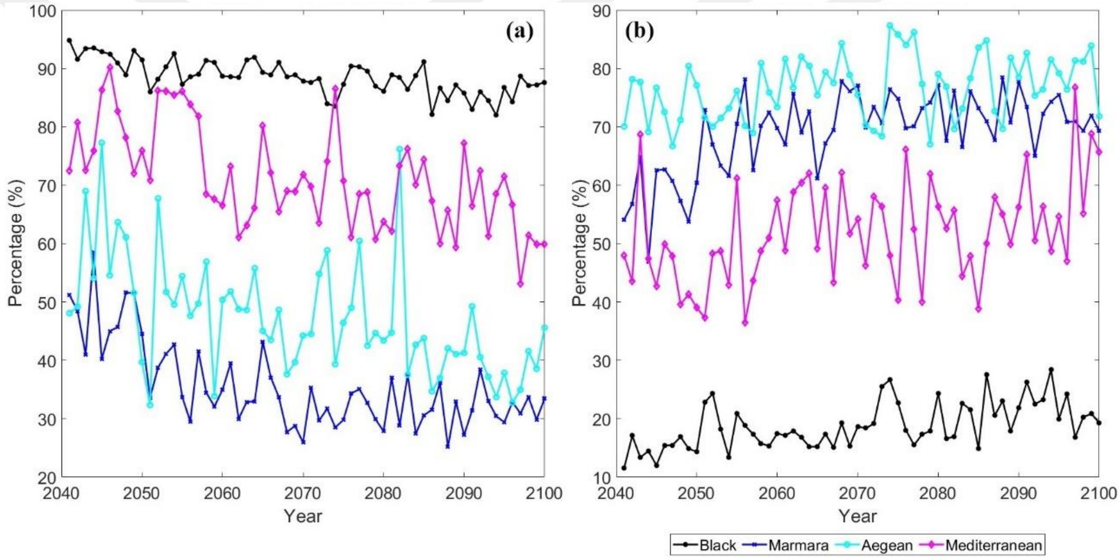

Figure 3.5. The (a) SS and (b) TE fractions of TWL, adapted from Uzun and Otay (2025).

3.1.4. Trendlines of Time Series Data

Trendlines of annual average, maximum, and minimum values of TWL, SS, and TE are obtained using the linear least squares regression method for the four seas in historical (1977-2005), mid-century (2041-2070), and end-century (2071-2100) periods are shown in Figure 3.6, Figure 3.7, and Figure 3.8, respectively. The slopes, intercepts, and RMSD values of these trendlines are shown in Table 3.1 for the historical period and Table 3.2 for the future periods.

In the historical period, TE trendlines have zero slope, which means they are stable. The ranges between minimum and maximum TE values in the Black, Marmara, Aegean, and Mediterranean Seas are -0.2 - 0.2 m, -0.05 - 0.15 m, -0.5 - 0.5 m, and -0.3 - 0.3 m, respectively (Figure 3.6). There is no considerable change in average SS and TWL values through the historical period. However, the trends and RMSD values of maximum and minimum values of SS and TWL indicate more dynamic behavior, especially in the Black Sea. The four seas' maximum TWL values have a decreasing trend, while the maximum SS in the Aegean Sea has an increasing trend. The Black Sea seems to have an increasing trend in the maximum SS. However, this is a miscalculation due to the incorrect SS data in the dataset at the beginning of the historical period. Considering the almost constant maximum TE values and the similar up-and-down movements of the SS and TWL data in the Black Sea through this period, it is reasonable to conclude that the maximum SS data has a decreasing trend similar to the maximum TWL data.

The slopes of the average TE trendlines in the mid-century period for the four seas are almost the same (Figure 3.7). The increase in the average TE is ~6.5 mm/year. For the maximum TE trendlines in the mid-century period, the slope has the highest value of 7.4 mm/year in the Black Sea and ~6.5 mm/year in the other three seas. However, the Aegean and Mediterranean seas still have the highest maximum TE values in 2070 due to their higher values in 2041. The slopes of the minimum TE trendlines of the Marmara, Black, Aegean, and Mediterranean seas are 6.5 mm/year, 6.4 mm/year, 6.3 mm/year, and 5.9 mm/year, respectively (Table 3.2).

The slopes of the average SS trend lines for the four seas are almost 0 in the mid-century period, meaning the mean value does not change significantly (Figure 3.7). The maximum SS value in the Black Sea increases with a slope of 22.7 mm/year, while those in the other seas slightly decrease (Table 3.2). While minimum SS values show a small decrease in the Black, Marmara, and Aegean Seas, they remain almost the same in the Mediterranean. However, unlike TE values, the maximum and minimum SS values have significant deviations (residuals) from the trendline regardless of the increasing or decreasing trends (Figure 3.7) because the SS has a short-term response as well as a long-term response to changes in atmospheric phenomena.

The average TWL trendlines in the mid-century period for the four seas increase at almost the same rate of around 6 mm/year (Figure 3.7 and Table 3.2). The seas with the slopes of the maximum TWL trendlines in decreasing order are the Black Sea (29.3 mm/year), Marmara Sea (5.8 mm/year), Aegean Sea (5.1 mm/year), and Mediterranean Sea (4.4 mm/year). The minimum TWL values in the Black, Aegean, Marmara, and Mediterranean Seas increase with slopes of 6.8 mm/year, 6 mm/year, 5.9 mm/year, and 5.6 mm/year, respectively.

The slopes of the average TE trendlines in the end-century period for the four seas are almost the same (Figure 3.8). The increase in the average TE is ~4.6 mm/year, which is smaller than that value in the mid-century period. This decrease arises from the difference between the RCP8.5 and RCP4.5 scenarios. For the maximum TE trendlines in the end-century period, the slope has a value of 4.8 mm/year in the four seas. However, the Aegean and Mediterranean seas still have the highest maximum TE values in 2100 due to their higher values in 2071. The slope of the minimum TE trendlines of the four seas is around 4.5 mm/year (Table 3.2). In addition, there are negligible deviations from the trendline in the mid and end-century periods, which indicates a continuous increase in the TE data. Hence, instead of the extreme value indicators such as return period, the highest values of TE data should be considered while investigating coastal flood hazards.

The slopes of the average SS trendlines for the four seas are almost 0 in the end-century period, meaning the mean value does not change significantly (Figure 3.8). The maximum SS values in the Black and Marmara Seas increase with a slope of 11.6 mm/year and 2.2 mm/year, respectively, while those in the Aegean (-3.5 mm/year) and Mediterranean Seas (3 mm/year) decrease (Table 3.2). While the minimum SS value shows a considerable downward trend in the Black Sea (-14.7 mm/year), it slightly decreases in the other seas. Furthermore, as observed in the mid-century period, the maximum and minimum SS values significantly differ from the trendline regardless of the increasing or decreasing trends.

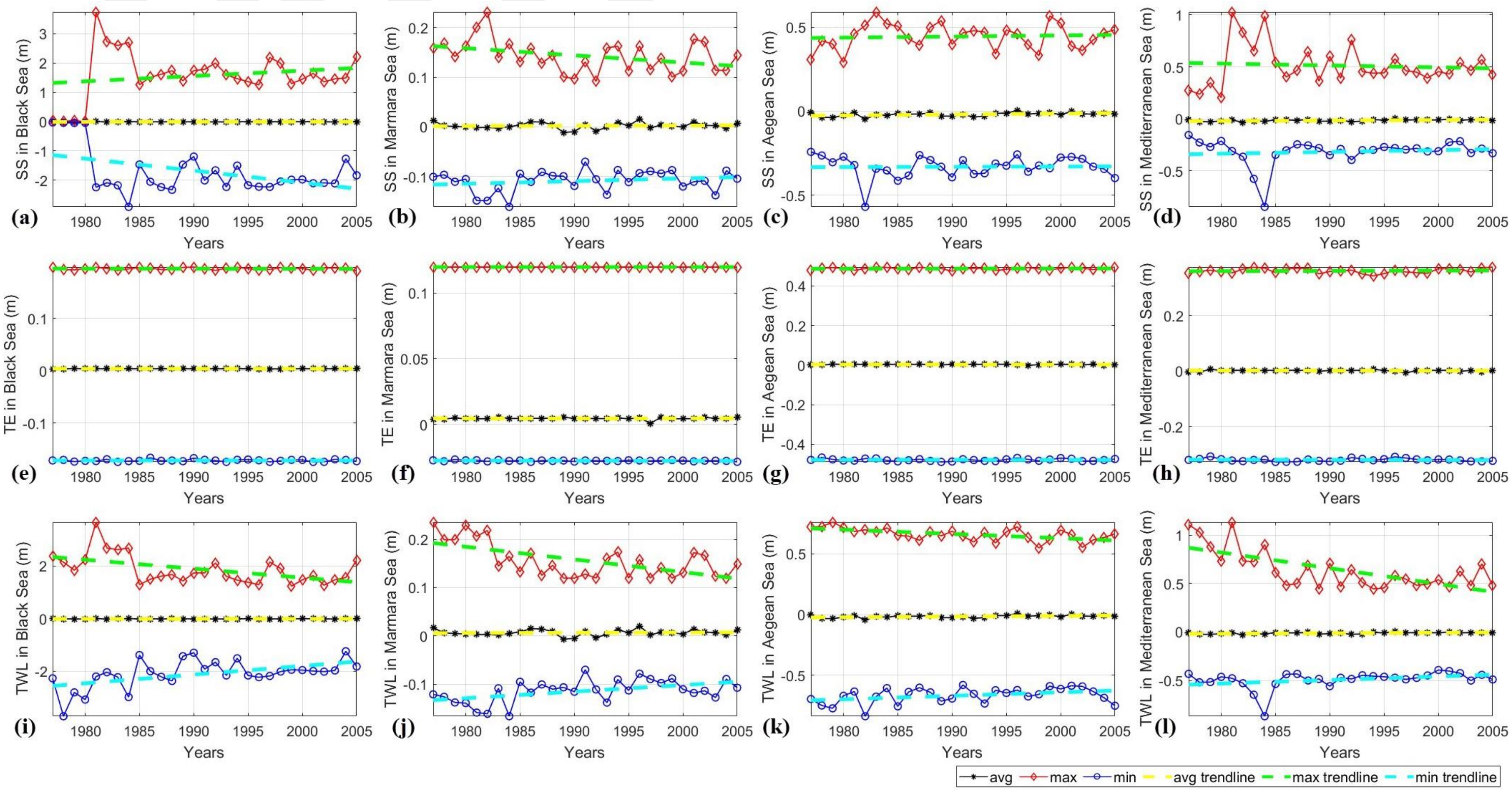

Figure 3.6. Trendlines of annual average, maximum, and minimum values of SS in (a) Black, (b) Marmara, (c) Aegean, and (d) Mediterranean seas, TE in (e) Black, (f) Marmara, (g) Aegean, and (h) Mediterranean seas, and TWL in (i) Black, (j) Marmara, (k) Aegean, and (l) Mediterranean seas for the historical period, adapted from Uzun and Otay (2025).

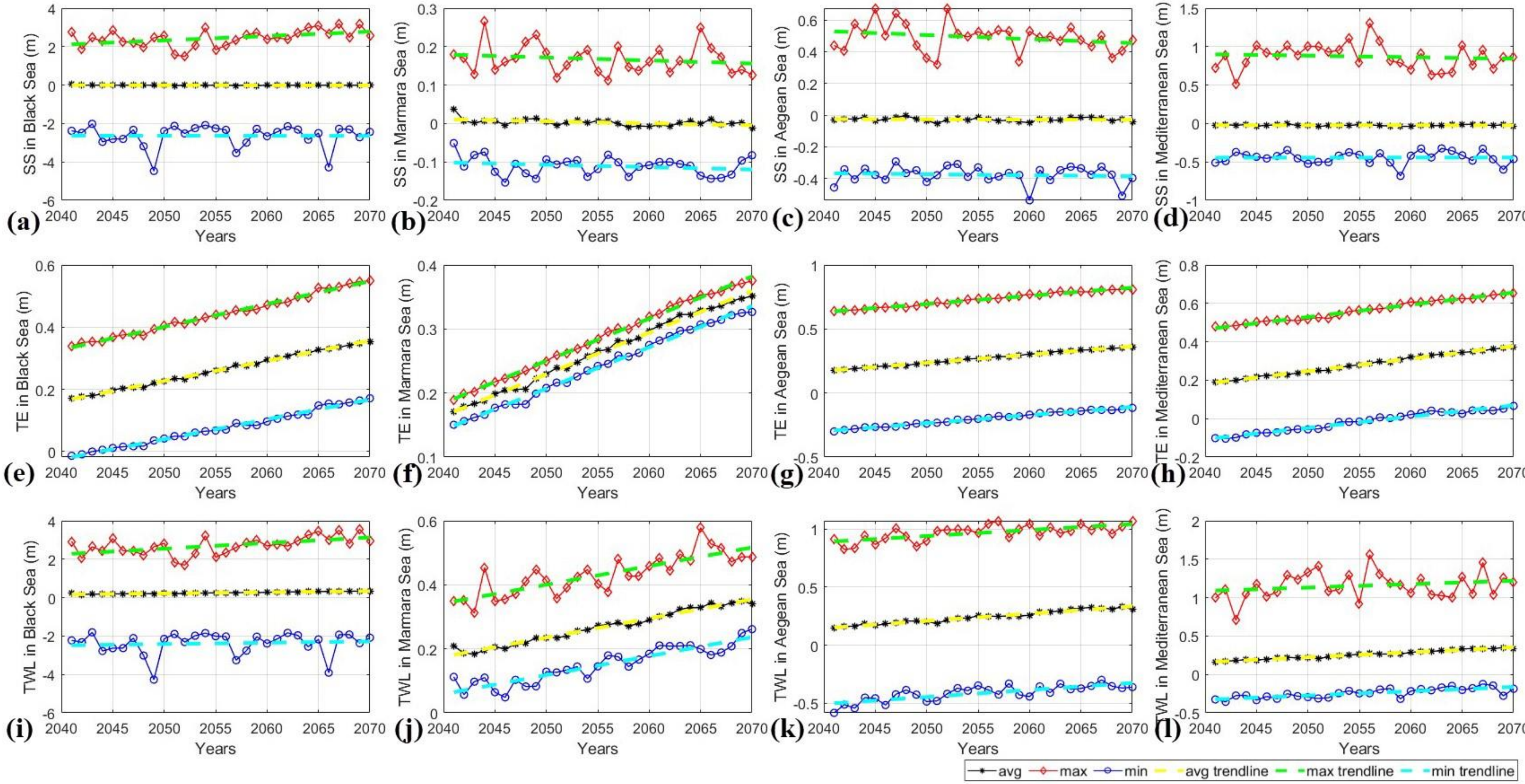

Figure 3.7. Trendlines of annual average, maximum, and minimum values of SS in (a) Black, (b) Marmara, (c) Aegean, and (d) Mediterranean seas, TE in (e) Black, (f) Marmara, (g) Aegean, and (h) Mediterranean seas, and TWL in (i) Black, (j) Marmara, (k) Aegean, and (l) Mediterranean seas for the mid-century period, adapted from Uzun and Otay (2025).

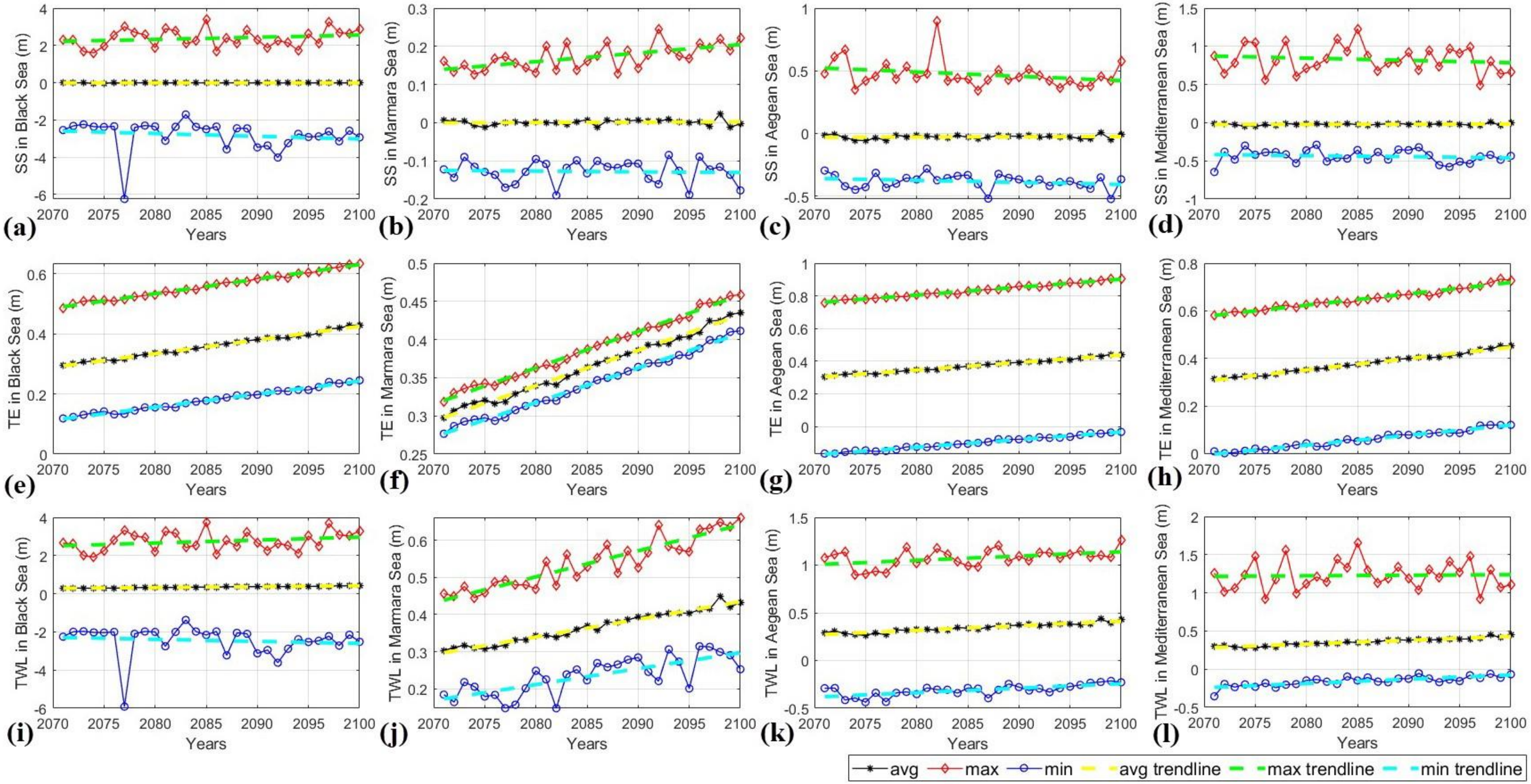

Figure 3.8. Trendlines of annual average, maximum, and minimum values of SS in (a) Black, (b) Marmara, (c) Aegean, and (d) Mediterranean seas, TE in (e) Black, (f) Marmara, (g) Aegean, and (h) Mediterranean seas, and TWL in (i) Black, (j) Marmara, (k) Aegean, and (l) Mediterranean seas for the end-century period, adapted from Uzun and Otay (2025).

Table 3.1. Slope, intercept, and RMSD of the trendlines for the historical period.

			Black Sea	**Marmara Sea**	**Aegean Sea**	**Mediterranean Sea**
TWL	Avg	Slope	0.0001	0.0001	0.0006	0.0005
		Intercept	-0.1239	-0.0994	-1.1288	-1.0062
		RMSD	0.0049	0.0061	0.0101	0.0076
	Max	Slope	-0.0341	-0.0026	-0.0035	-0.0163
		Intercept	69.7932	5.3832	7.6834	33.0199
		RMSD	0.4667	0.0279	0.0411	0.1432
	Min	Slope	0.0329	0.0014	0.0029	0.0036
		Intercept	-67.6336	-2.8233	-6.3873	-7.7454
		RMSD	0.4496	0.0204	0.0582	0.0814
TE	Avg	Slope	0.0000	0.0000	0.0000	0.0000
		Intercept	0.0030	-0.0009	0.0526	0.0745
		RMSD	0.0001	0.0008	0.0018	0.0027
	Max	Slope	0.0000	0.0000	0.0000	0.0001
		Intercept	0.2235	0.1197	0.3883	0.1379
		RMSD	0.0021	0.0000	0.0053	0.0083
	Min	Slope	0.0000	0.0000	0.0000	-0.0001
		Intercept	-0.1628	-0.0046	-0.4472	-0.2124
		RMSD	0.0020	0.0004	0.0058	0.0050
SS	Avg	Slope	0.0001	0.0000	0.0006	0.0005
		Intercept	-0.1257	-0.0972	-1.1351	-1.0123
		RMSD	0.0049	0.0062	0.0101	0.0076
	Max	Slope	0.0182	-0.0014	0.0007	-0.0018
		Intercept	-34.6502	3.0183	-0.8656	4.1584
		RMSD	0.8107	0.0295	0.0743	0.1913
	Min	Slope	-0.0410	0.0005	0.0001	0.0017
		Intercept	79.8967	-1.1832	-0.5911	-3.7782
		RMSD	0.6714	0.0204	0.0641	0.1226

Table 3.2. Slope, intercept, and RMSD for mid- and end-century of the trendlines for the future period.

			Black Sea		Marmara Sea		Aegean Sea		Mediterranean Sea	
			mid	**end**	**mid**	**end**	**mid**	**end**	**mid**	**end**
TWL	Avg	Slope	0.0060	0.0046	0.0060	0.0047	0.0063	0.0048	0.0065	0.0050
		Intercept	-12.0182	-9.1937	-12.0100	-9.5074	-12.6471	-9.7240	-13.0077	-10.1074
		RMSD	0.0114	0.0072	0.0086	0.0074	0.0110	0.0154	0.0089	0.0126
	Max	Slope	0.0293	0.0155	0.0058	0.0070	0.0051	0.0045	0.0044	0.0008
		Intercept	-57.4624	-29.5873	-11.5155	-14.0438	-9.6154	-8.3067	-7.9165	-0.4404
		RMSD	0.3869	0.4593	0.0359	0.0258	0.0490	0.0782	0.1663	0.1800
	Min	Slope	0.0068	-0.0109	0.0059	0.0043	0.0060	0.0047	0.0056	0.0056
		Intercept	-16.2697	20.2147	-12.0395	-8.7080	-12.8003	-10.0583	-11.6765	-11.8222
		RMSD	0.5792	0.7892	0.0226	0.0322	0.0417	0.0424	0.0390	0.0388
TE	Avg	Slope	0.0065	0.0045	0.0065	0.0046	0.0064	0.0046	0.0065	0.0048
		Intercept	-13.0610	-9.1237	-13.1035	-9.2914	-12.9762	-9.2550	-13.0975	-9.5822
		RMSD	0.0033	0.0038	0.0041	0.0038	0.0040	0.0036	0.0040	0.0041
	Max	Slope	0.0074	0.0048	0.0066	0.0048	0.0064	0.0048	0.0064	0.0048
		Intercept	-14.6720	-9.5370	-13.2744	-9.5372	-12.3752	-9.2287	-12.5705	-9.2777
		RMSD	0.0063	0.0044	0.0034	0.0036	0.0069	0.0047	0.0074	0.0072
	Min	Slope	0.0064	0.0043	0.0065	0.0045	0.0063	0.0047	0.0059	0.0042
		Intercept	-13.0365	-8.8603	-13.0174	-9.1022	-13.1574	-9.8434	-12.1072	-8.6615
		RMSD	0.0061	0.0046	0.0040	0.0037	0.0060	0.0049	0.0088	0.0066
SS	Avg	Slope	-0.0005	0.0000	-0.0005	0.0001	-0.0002	0.0002	-0.0001	0.0002
		Intercept	1.0428	-0.0701	1.0935	-0.2160	0.3291	-0.4690	0.0898	-0.5252
		RMSD	0.0106	0.0060	0.0079	0.0071	0.0111	0.0150	0.0085	0.0112
	Max	Slope	0.0227	0.0116	-0.0008	0.0022	-0.0026	-0.0035	-0.0020	-0.0030
		Intercept	-44.1287	-21.9058	1.7749	-4.5127	5.7493	7.7103	4.9481	7.0663
		RMSD	0.3864	0.4555	0.0365	0.0250	0.0837	0.1027	0.1617	0.1711
	Min	Slope	-0.0005	-0.0147	-0.0006	-0.0002	-0.0006	-0.0016	0.0001	-0.0014
		Intercept	-1.6993	27.8829	1.1585	0.2691	0.9029	2.9926	-0.6337	2.5148
		RMSD	0.5754	0.7893	0.0232	0.0285	0.0533	0.0541	0.0796	0.0824

The average TWL trendlines in the end-century period for the four seas increase at almost the same rate of around 4.8 mm/year (Figure 3.8 and Table 3.2). The seas with the slopes of the maximum TWL trendlines in decreasing order are the Black Sea (15.5 mm/year), Marmara Sea (7 mm/year), Aegean Sea (4.5 mm/year), and Mediterranean Sea (0.8 mm/year). The minimum TWL value in the Black Sea decreases with a slope of -1.1 mm/year, while those in the Aegean, Marmara, and Mediterranean Seas increase with slopes of 4.7 mm/year, 4.3 mm/year, and 5.6 mm/year, respectively.

RMSD values for the four seas in the mid and end-century periods can be seen in Table 3.2. These RMSD values quantify the deviations from the trendlines in Figure 3.7 and Figure 3.8. Maximum and minimum TWL and SS in the Black Sea have the highest RMSD values. In addition, small values of RMSD are observed in all TE graphs due to the small residuals. For the maximum values of the TWL and SS data, there is an increase between the RMSD values of mid- and end-century periods, except for the Marmara Sea. In addition, overall RMSD values in the historical period are less than RMSD values in the mid and end-century periods. This analysis proves that climate change considerably affects the maxima and minima of TWL and SS rather than their mean values.

3.1.5. Probability Distribution

This part of the analysis explores how the PD characteristics of TWL, SS, and TE differ across the four regional seas and how these characteristics shift under future climate scenarios. To evaluate these differences, the key statistical moments, the mean, std, skewness, and kurtosis, are examined.

Figure 3.9, Figure 3.10, and Figure 3.11 illustrate the histogram distributions of SS, TE, and TWL time series for the Black, Marmara, Aegean, and Mediterranean seas, spanning three periods. The mean of each time series is used to represent the expected long-term average. In this context, the evolution of mean TWL, SS, and TE values is tracked through the historical, mid-century, and end-century periods. During the historical period, the spatial mean, maximum, and minimum values for all three variables show relatively minor variation, as summarized in Table 3.3. The largest deviations occur in the Black Sea, where the gap between the mean of maximum and minimum TWL reaches 0.57 m, and for SS, this difference is 0.52 m.

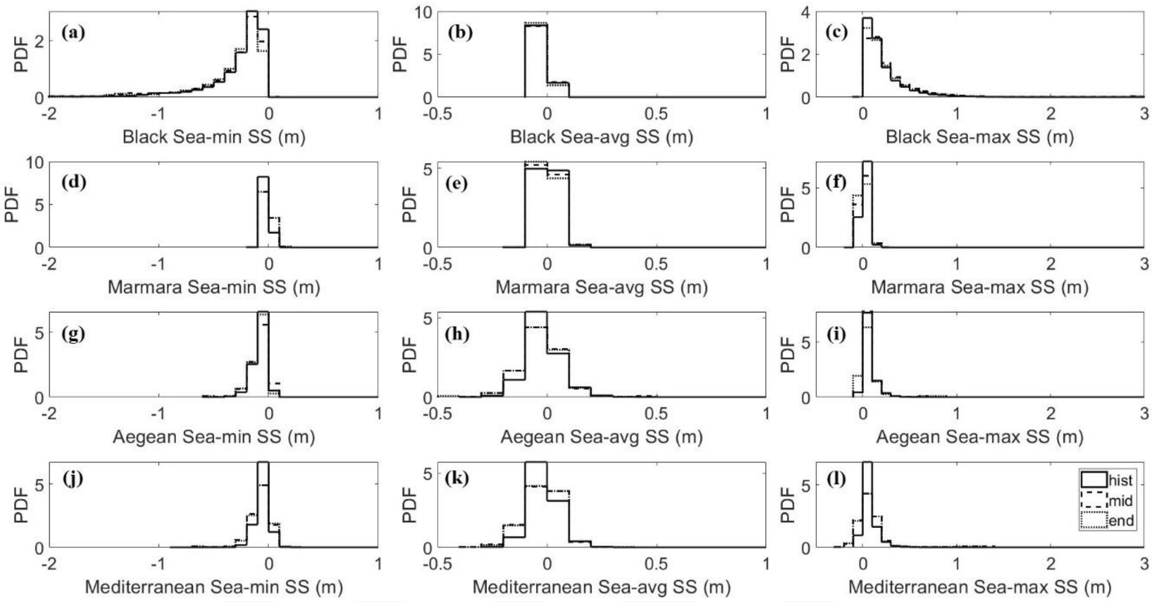

Figure 3.9. (a-c) Min, avg, and max SS histograms of the Black, (d-f) Marmara, (g-i), Aegean, and (j-l) Mediterranean Seas in the historical, mid-century, and end-century periods (Uzun and Otay, 2025).

Projections for the mid-century and end-century periods indicate that the Black Sea continues to experience the highest mean TWL values, rising from 0.53 m to 0.62 m across the two future intervals. The Aegean, Mediterranean, and Marmara seas follow with values of 0.41 m (0.51 m), 0.39 m (0.48 m), and 0.28 m (0.38 m), respectively (Figure 3.11). For the maximum SS, the mean values during the same periods are 0.26 m (0.25 m) in the Black Sea, 0.06 m (0.05 m) in the Aegean, 0.07 m (0.06 m) in the Mediterranean, and 0.02 m (0.01 m) in the Marmara (Figure 3.9). In contrast, maximum TE means show a slight increase over time, with values rising to 0.33 m (0.44 m) in the Black Sea, 0.41 m (0.52 m) in the Aegean, 0.37 m (0.46 m) in the Mediterranean, and 0.27 m (0.37 m) in the Marmara (Figure 3.10). Among all regions, the Marmara Sea consistently records the lowest average values across all three indicators. Importantly, a general upward trend is observed in TWL and TE means through time, while SS means tend to decline.

The std describes how much the values deviate from the mean within a dataset. When the std is higher, it means data points are more spread out, indicating increased variability.

In the future periods, std values generally rise compared to the historical baseline, reflecting more unstable sea level components. Among the studied basins, the Black Sea stands out with the highest standard deviations, reaching 0.27 m for maximum TWL and SS, and up to 0.41 m for their minimum counterparts, pointing to considerable fluctuations. The Aegean and Mediterranean seas also display relatively high std values for maximum TWL (~0.12 m), while the Marmara Sea shows much lower variability across all indicators (Table 3.3).

Skewness, on the other hand, reveals how asymmetrical a distribution is. Distributions with skewness above +0.5 are considered right-skewed, where the right tail (higher values) is more extended. Values below -0.5 indicate left-skewness, where unusually low values stretch the distribution's left side. Overall, the average SS, TE, and TWL across time appear approximately symmetric (Figure 3.9, Figure 3.10, and Figure 3.11), suggesting balanced data distributions. Similarly, the spatial maxima and minima of TE show minimal skewness. For spatial maximum SS, however, strong right-skewness is evident across the seas and periods, with skewness values between 0.82 and 2.70, highlighting the influence of high SS outliers. In the minimum SS and TWL distributions of future periods, skewness is weak in most basins, except in the Black Sea, which uniquely shows both strongly left-skewed and right-skewed distributions, reaching –2.58 and +2.97. Future maximum TWL distributions also show slight right-skewness in most basins. However, the Black Sea emerges with the most asymmetric pattern, with skewness values exceeding 2.6, primarily due to heavily skewed maximum SS (Table 3.3).

Kurtosis is a measure used to understand how concentrated or flattened a distribution is compared to a normal distribution (which has a kurtosis of 3). Distributions with values above 3 are classified as heavy-tailed, meaning they include more extreme values, while values below 3 indicate fewer outliers and a flatter profile. In both historical and projected future conditions, TE distributions tend to remain near-symmetric or lightly tailed, suggesting a limited presence of outliers. The Marmara Sea generally exhibits kurtosis values close to 3, except its maximum SS reaches 4.20 by the end of the century. By contrast, the Black Sea displays extremely peaked distributions for both SS and TWL extremes in future projections. Maximum kurtosis values range between 11.22 and 16.62, especially for maximum TWL and SS, indicating significant tail heaviness. Aegean and Mediterranean maximum SS distributions are also highly peaked, with kurtosis values around 8 (Table 3.3).

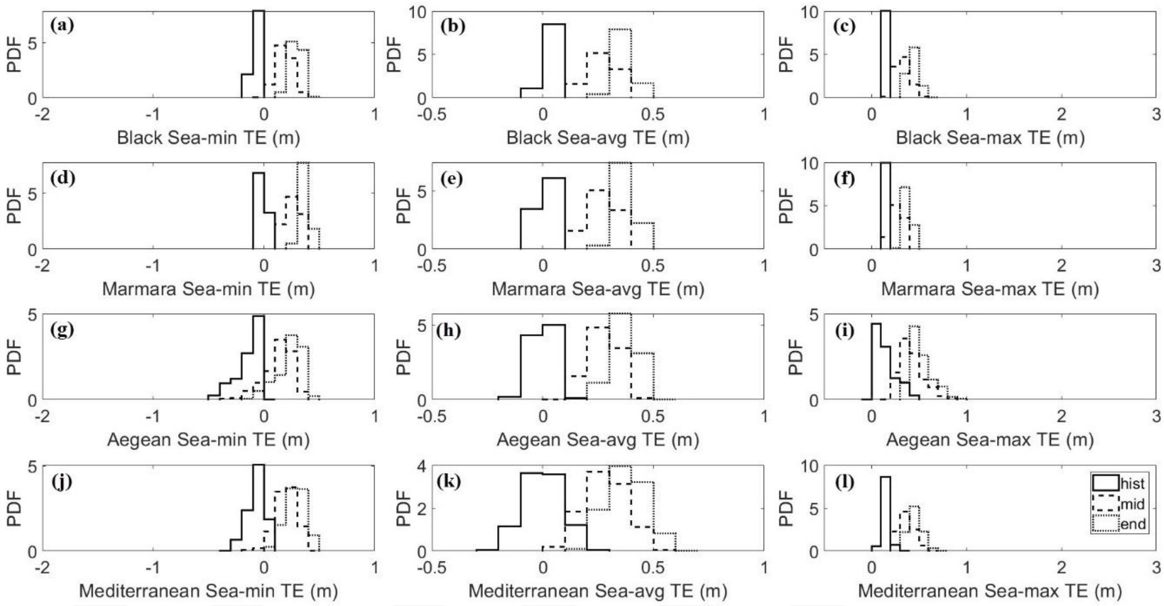

Figure 3.10. (a-c) Min, avg, and max TE histograms of the Black, (d-f) Marmara, (g-i), Aegean, and (j-l) Mediterranean Seas in the historical, mid-century, and end-century periods (Uzun and Otay, 2025).

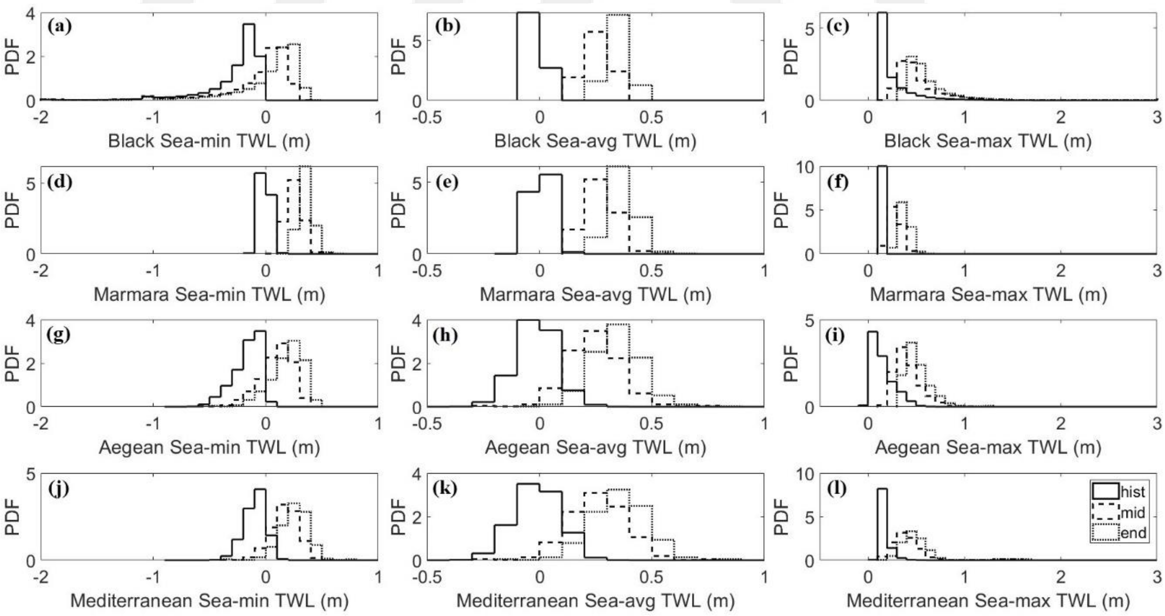

Figure 3.11. (a-c) Min, avg, and max TWL histograms of the Black, (d-f) Marmara, (g-i), Aegean, and (j-l) Mediterranean Seas in the historical, mid-century, and end-century periods (Uzun and Otay, 2025).

3.1.6. Tidal Indicators

Figure 3.12 displays the epoch-mean MHHW and the epoch-maximum HAT for both the historical and end-century periods. The spatial variability of these tidal indicators reveals a strong dependence on geographic location, particularly evident in the Aegean and Mediterranean seas by the end of the century. In contrast, the Black Sea and Marmara Sea demonstrate more spatially uniform patterns, which can be attributed to their relatively enclosed nature and limited exchange with larger oceanic systems. The change between the historical and future periods ranges from 0 to 0.1 m for MHHW, and from –0.05 to 0.1 m for HAT. These small differences suggest only modest shifts in tidal levels over time. Overall, the variation in tidal range across the four regional seas within this subdomain of the six CORDEX regions remains relatively limited in future projections.

3.1.7. Epoch-mean MSL

Figure 3.13 illustrates the epoch-mean MSL for the historical and end-century periods. The spatial pattern of epoch-mean MSL shows substantial location dependence, particularly in the Aegean and Mediterranean seas, where values in the end-century period range from approximately 0.3 m to 0.4 m. In contrast, the Black and Marmara Seas display relatively uniform sea level patterns, reflecting their more enclosed basin characteristics. The difference map in Figure 3.13 indicates a consistent MSL rise across all four seas, with increases falling within the range of 0.2 to 0.4 meters.

3.1.8. Extreme Value Indicators

As seen in Figure 3.14, RP1 SS values between the historical and end-century periods slightly increase with the maximum difference value of 0.1 m at the northeastern part of the Sea of Azov or do not change. In RP10 and RP100 SS values, the differences get higher. These differences range between -0.25 – 0.25 m in RP10 and -0.4 – 0.5 m in RP100. In the Marmara and Mediterranean Seas, the SS values slightly change in the order of a few centimeters. The Black and Aegean Seas, except their northern areas, experience small changes in the SS values.

Table 3.3. Moments of PDs in the historical, mid-century, and end-century periods.

			μ (m)			std (m)			skewness			kurtosis		
			hist	**mid**	**end**	**hist**	**mid**	**end**	**hist**	**mid**	**end**	**hist**	**mid**	**end**
Black Sea	**TWL**	**Avg**	-0.0051	0.2522	0.3482	0.0088	0.0529	0.0416	-0.2118	0.1647	0.0569	3.6366	1.8802	2.1010
		Max	0.2714	0.5264	0.6196	0.1962	0.2656	0.2581	3.3707	2.6625	2.6994	19.2804	14.2324	14.4907
		Min	-0.2966	-0.1160	-0.0079	0.3198	0.4163	0.4008	-2.8253	-2.5726	-2.9494	13.3828	11.2673	16.6214
	SS	**Avg**	-0.0087	-0.0093	-0.0114	0.0094	0.0146	0.0106	-0.1317	1.6371	-0.3146	3.4892	8.9326	3.3695
		Max	0.2159	0.2641	0.2476	0.2237	0.2670	0.2614	2.6720	2.6918	2.7000	13.8797	14.1424	14.2065
		Min	-0.2964	-0.3623	-0.3601	0.3251	0.4149	0.4015	-2.7587	-2.5825	-2.9699	12.9379	11.2150	16.5861
	TE	**Avg**	0.0037	0.2627	0.3596	0.0029	0.0564	0.0397	-0.1235	-0.0060	0.1007	2.4588	1.7129	1.8981
		Max	0.1732	0.3288	0.4365	0.0007	0.0693	0.0569	17.3085	0.2241	0.2867	363.794	2.4318	2.6820
		Min	-0.0720	0.1820	0.2914	0.0338	0.0691	0.0527	-0.4274	0.0196	-0.1679	2.4808	2.3508	2.5946
Marmara Sea	**TWL**	**Avg**	0.0067	0.2667	0.3659	0.0357	0.0640	0.0563	0.3754	0.2030	0.3439	3.9737	2.5700	3.1288
		Max	0.1202	0.2817	0.3771	0.0033	0.0614	0.0574	15.2103	0.3644	0.4371	281.538	2.6867	3.3312
		Min	-0.0049	0.2541	0.3546	0.0359	0.0635	0.0562	0.2145	0.2247	0.3097	3.6964	2.5608	3.0687
	SS	**Avg**	0.0023	0.029	0.0009	0.0361	0.0388	0.0381	0.4703	0.6825	0.7076	3.9948	3.6306	3.8880
		Max	0.0196	0.0174	0.0109	0.0291	0.0393	0.0403	1.7053	0.7862	0.8210	7.4037	3.6560	4.1988
		Min	-0.0165	-0.0090	-0.0092	0.0235	0.0365	0.0372	-0.8587	0.6580	0.6517	6.1054	3.7816	3.8796
	TE	**Avg**	0.0045	0.2651	0.3650	0.0100	0.0567	0.0405	0.5709	-0.0656	0.1037	2.5647	1.6856	1.8374
		Max	0.1197	0.2707	0.3707	0.0000	0.0569	0.0406	-	-0.0634	0.1039	-	1.6934	1.8543
		Min	-0.0029	0.2589	0.3593	0.0104	0.0569	0.0406	0.4201	-0.0587	0.1019	2.5788	1.7016	1.8519
Aegean Sea	**TWL**	**Avg**	-0.0155	0.2414	0.3429	0.0887	0.1097	0.1050	-0.0338	0.0506	0.0241	3.3941	3.0341	3.3141
		Max	0.1470	0.4076	0.5117	0.1161	0.1293	0.1246	1.0661	0.8584	0.9819	3.6772	3.6176	3.8875
		Min	-0.1637	0.0922	0.1931	0.1249	0.1437	0.1402	-0.8901	-0.6547	-0.7182	3.3312	3.1214	3.1730
	SS	**Avg**	-0.0191	-0.0277	-0.0282	0.0774	0.0875	0.0880	0.4896	0.0918	0.0886	4.1991	3.5770	3.6767
		Max	0.0613	0.0580	0.0541	0.0650	0.0628	0.0630	1.9414	1.8980	1.9531	7.9442	8.4341	8.6555
		Min	-0.0758	-0.0809	-0.0818	0.0610	0.0713	0.0715	-1.1018	-0.9499	-1.0343	4.7599	3.7128	3.9401
	TE	**Avg**	0.0025	0.2710	0.3711	0.0479	0.0682	0.0560	-0.1196	-0.1073	-0.0553	2.5553	2.3433	2.5029
		Max	0.1414	0.4149	0.5188	0.1088	0.1187	0.1102	0.9283	0.7179	0.8897	3.0104	3.0128	3.1658
		Min	-0.1354	0.1328	0.2333	0.1107	0.1222	0.1164	-1.0122	-0.7531	-0.8938	3.1036	3.0402	3.1275
Mediterranean Sea	**TWL**	**Avg**	-0.0123	0.2580	0.3562	0.1011	0.1214	0.1168	-0.0740	-0.0382	-0.0634	2.8412	2.7819	2.8816
		Max	0.1634	0.3908	0.4792	0.0582	0.1246	0.1227	2.9672	0.7718	0.6063	19.8451	4.7001	4.5855
		Min	-0.0961	0.1652	0.2571	0.0952	0.1177	0.1164	-0.4987	-0.3024	-0.3252	3.2989	3.0281	3.0875
	SS	**Avg**	-0.0152	-0.0234	-0.0218	0.0622	0.0787	0.0786	0.4387	-0.2998	-0.2579	4.5324	3.0275	3.2169
		Max	0.0664	0.0667	0.0656	0.0766	0.1029	0.1022	2.5205	1.2800	1.1203	14.6738	8.4620	7.7341
		Min	-0.0591	-0.0713	-0.0670	0.0565	0.0789	0.0792	-0.8099	-0.5549	-0.4888	5.4548	3.5806	3.6081
	TE	**Avg**	0.0016	0.2827	0.3779	0.0819	0.0934	0.0857	0.1072	0.0378	0.0750	2.3735	2.4633	2.4224
		Max	0.1427	0.3666	0.4580	0.0390	0.0804	0.0708	1.6577	0.4455	0.4349	6.6468	2.6895	2.8208
		Min	-0.0696	0.2013	0.2841	0.0750	0.0883	0.0883	-0.6170	-0.2723	-0.2465	2.7783	2.7016	2.5671

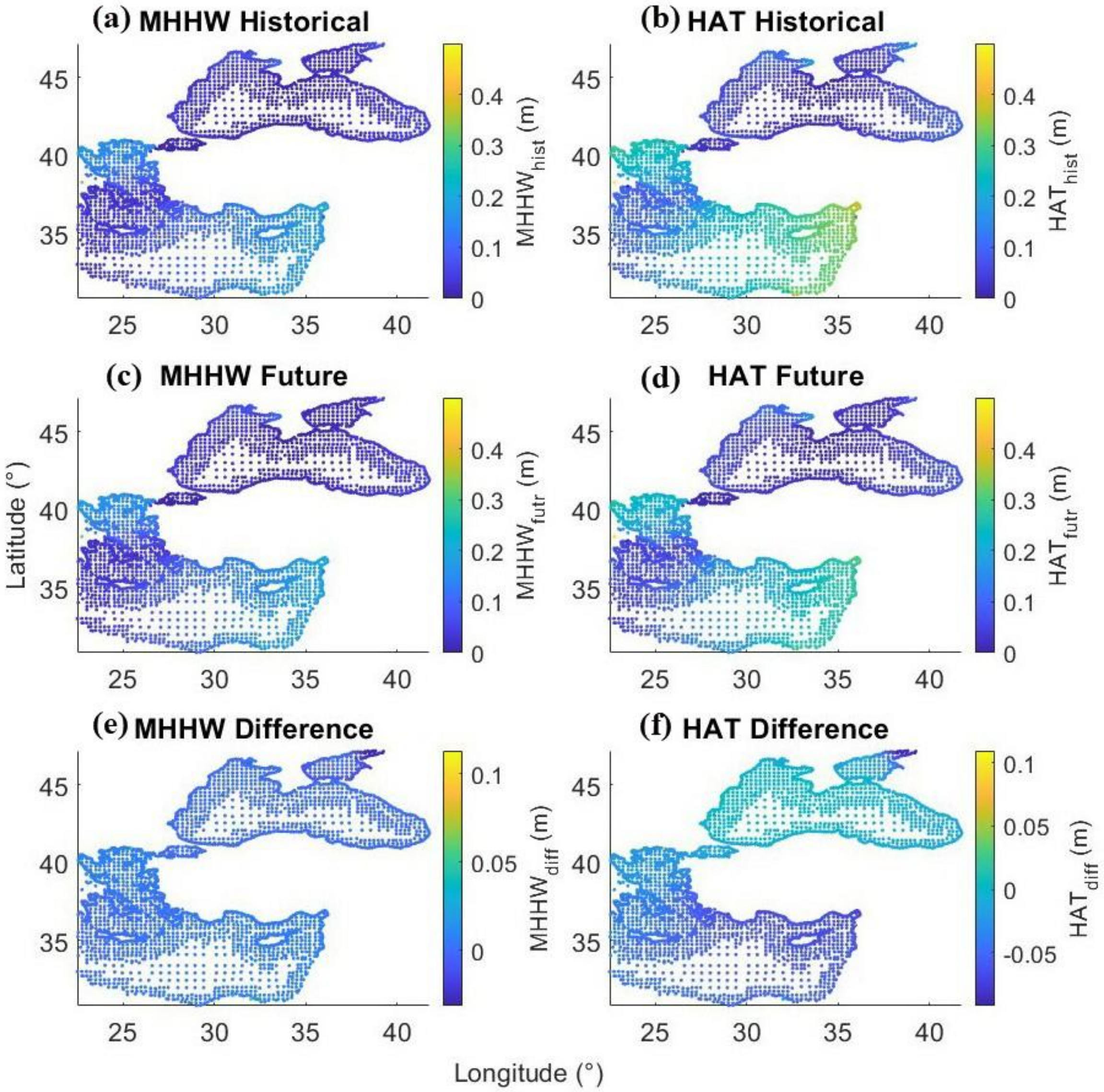

Figure 3.12. (a-b) Historical, (c-d) future, and (e-f) difference values between future and historical periods of MHHW and HAT, respectively, adapted from Uzun and Otay (2025).

There is a decrease in the future RP10 and RP100 SS values in shallow areas of the seas, such as the northern parts of the Black, Aegean, and Azov Seas, which is mainly the result of changes in water depth as well as changes in wind characteristics. It can be concluded that a small decrease may be observed in the future in regions with extreme SS values in the current climate.

The future TWL increases in all RPs (Figure 3.15). The increase in TWL shows that extreme water levels are growing and becoming more frequent. The difference between the

TWL of the historical and end-century periods ranges between 0.15 - 0.4 m in RP1, 0.1 - 0.6 m in RP10, and 0 - 0.9 m in RP100. In RP10 and RP100, the locations with the highest TWL values, the northern part of the Black Sea, including the Sea of Azov, are the same as the locations with the highest SS values. However, in RP1, the locations with the high TWL values are the reverse of those with the high SS values. That can be explained by the superposition of the TE and SS data since MHHW and MSL in the future period (Figure 3.12 and Figure 3.13) have the smallest values at the locations with the smallest RP1 TWL values.

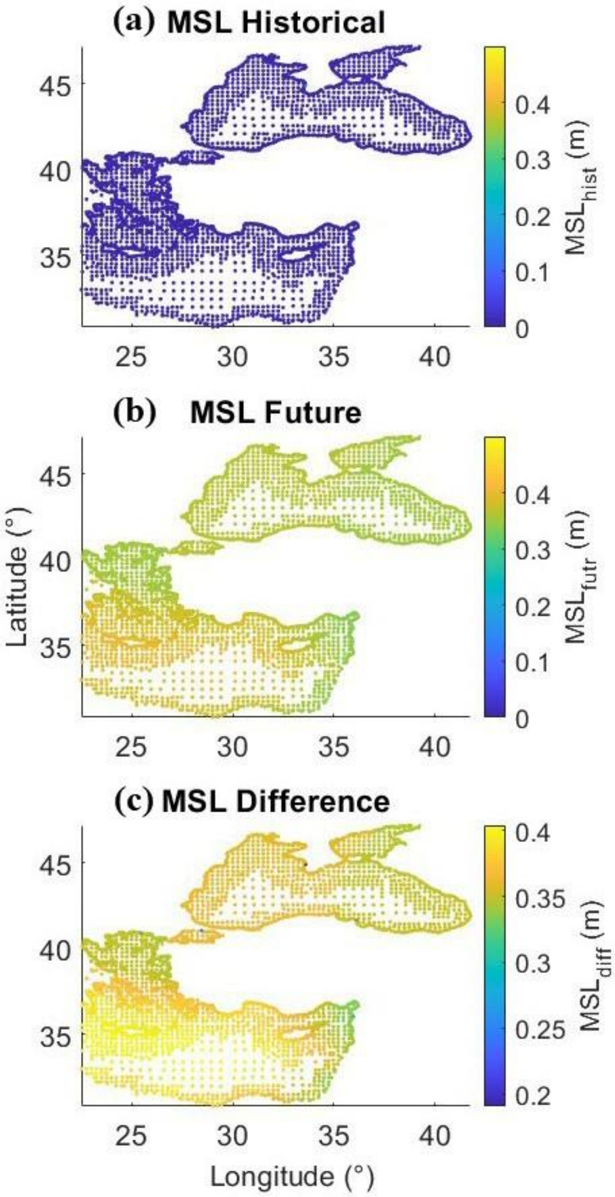

Figure 3.13. Epoch-mean MSL in (a) the historical and (b) end-century periods and (c) their difference, adapted from Uzun and Otay (2025).

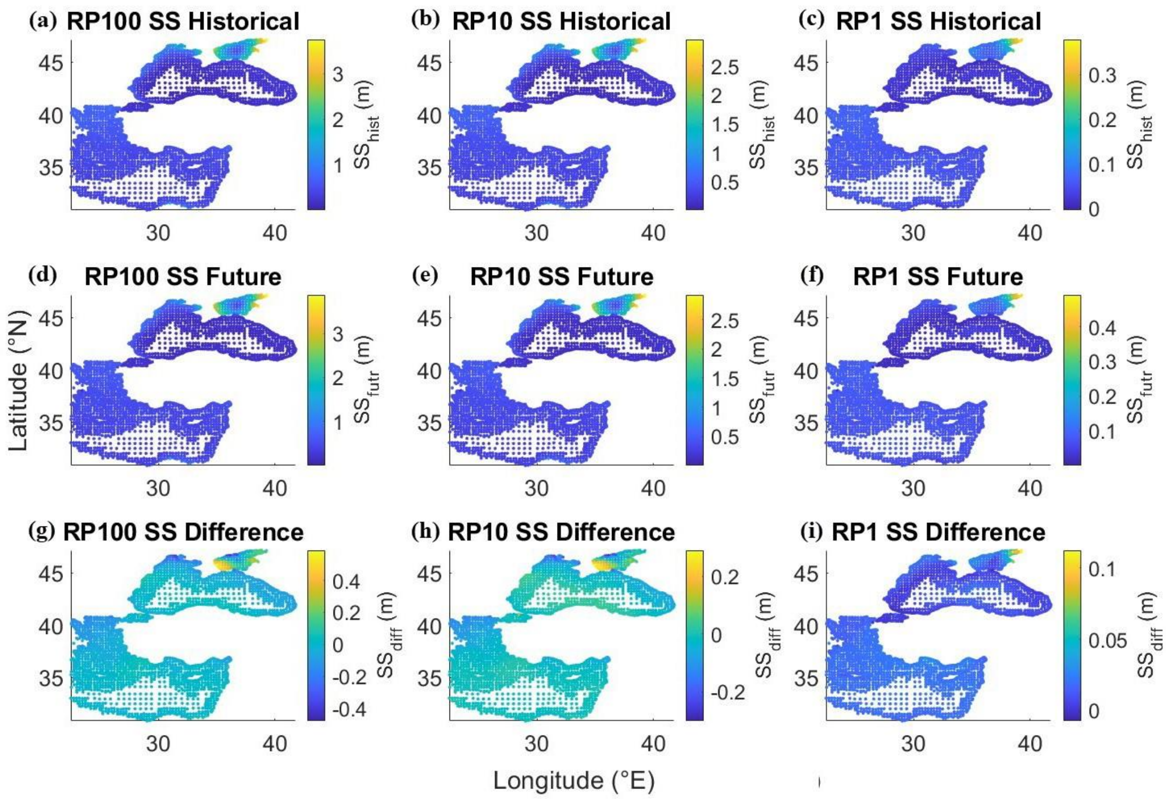

Figure 3.14. RP100, RP10, and RP1 SS of (a-c) the historical and (d-f) end-century periods and (g-i) their difference, respectively, modified from Uzun and Otay (2025).

3.1.9. Country Coasts

Figure 3.16 presents box plots of SS time series data, encompassing spatial and temporal mean, maximum, and minimum values along the coastlines of countries bordering the four seas, across three distinct periods. The median and mean values consistently drift around zero for all countries and epochs, indicating that the dataset captures a comprehensive range of wind conditions, not limited to storm events. This balanced inclusion of both calm and stormy conditions results in a symmetric distribution of SS values, maintaining stable central tendencies over time.

While the central tendencies remain stable, the variability and extremes of SS, depicted by the interquartile range, whiskers, and outliers, offer deeper insights into changes in SS behavior. A slight expansion in the interquartile range and whiskers across all countries suggests a modest increase in variability over time, likely influenced by evolving atmospheric and climatic conditions affecting SS patterns.

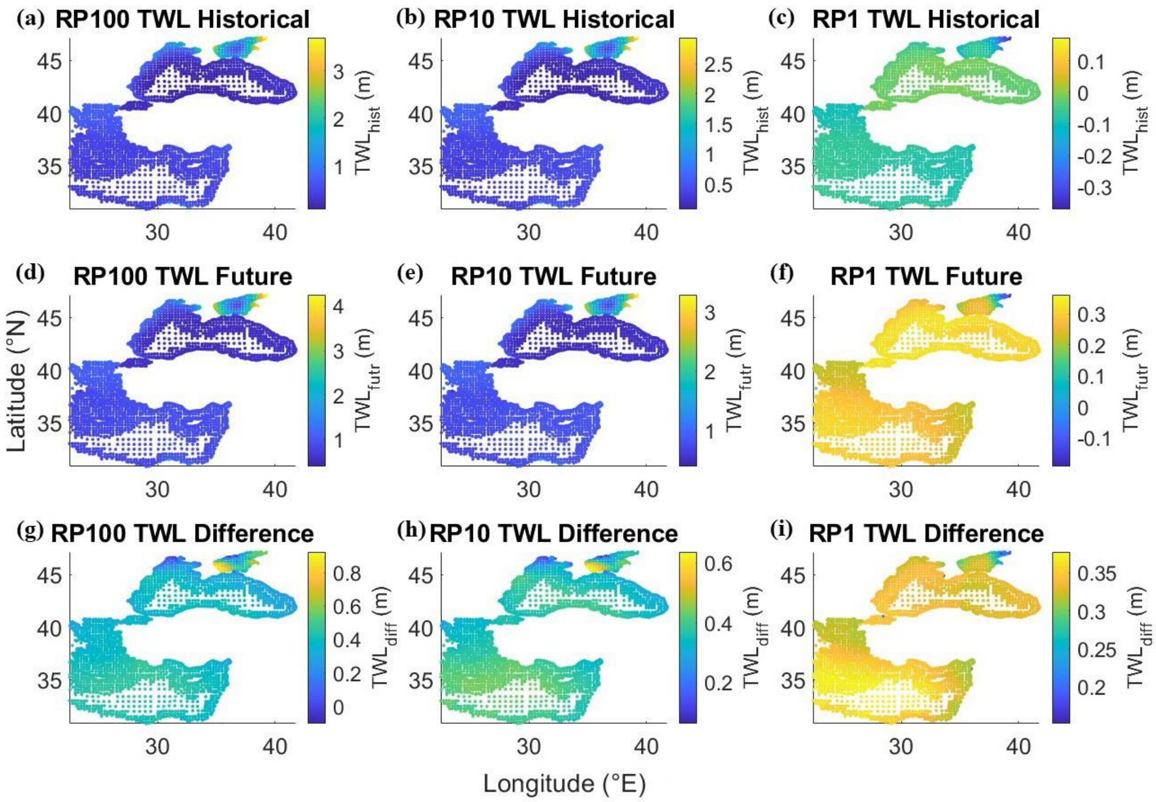

Figure 3.15. RP100, RP10, and RP1 TWL of (a-c) the historical and (d-f) end-century periods and (g-i) their difference, respectively, modified from Uzun and Otay (2025).

Notably, the outliers, along with the maximum and minimum values, exhibit more significant changes, highlighting an intensification of extreme storm surge events in certain regions. These changes are particularly relevant when assessing the heightened vulnerability associated with climate change-induced alterations in SS. Outliers increase along most coastlines, except those of the GE, RU, and TR-BS coastlines. In the end-century period, the most pronounced SS values are observed along the Russian (up to 3.4 m) and Ukrainian (up to 3 m) coasts, primarily attributed to the Azov Sea region. Conversely, certain coastlines, such as those of RO, EG, and IL/PS, exhibit a decrease in outliers in the end-century period compared to the mid-century. In the Aegean Sea, the GR and TR-AS coasts show similar SS values around 0.9 m in the end-century period. Along the Mediterranean Sea, the Egyptian coast stands out with SS values reaching 1.2 m in the end-century, while the TR-MS coast consistently displays the lowest SS values across all periods.

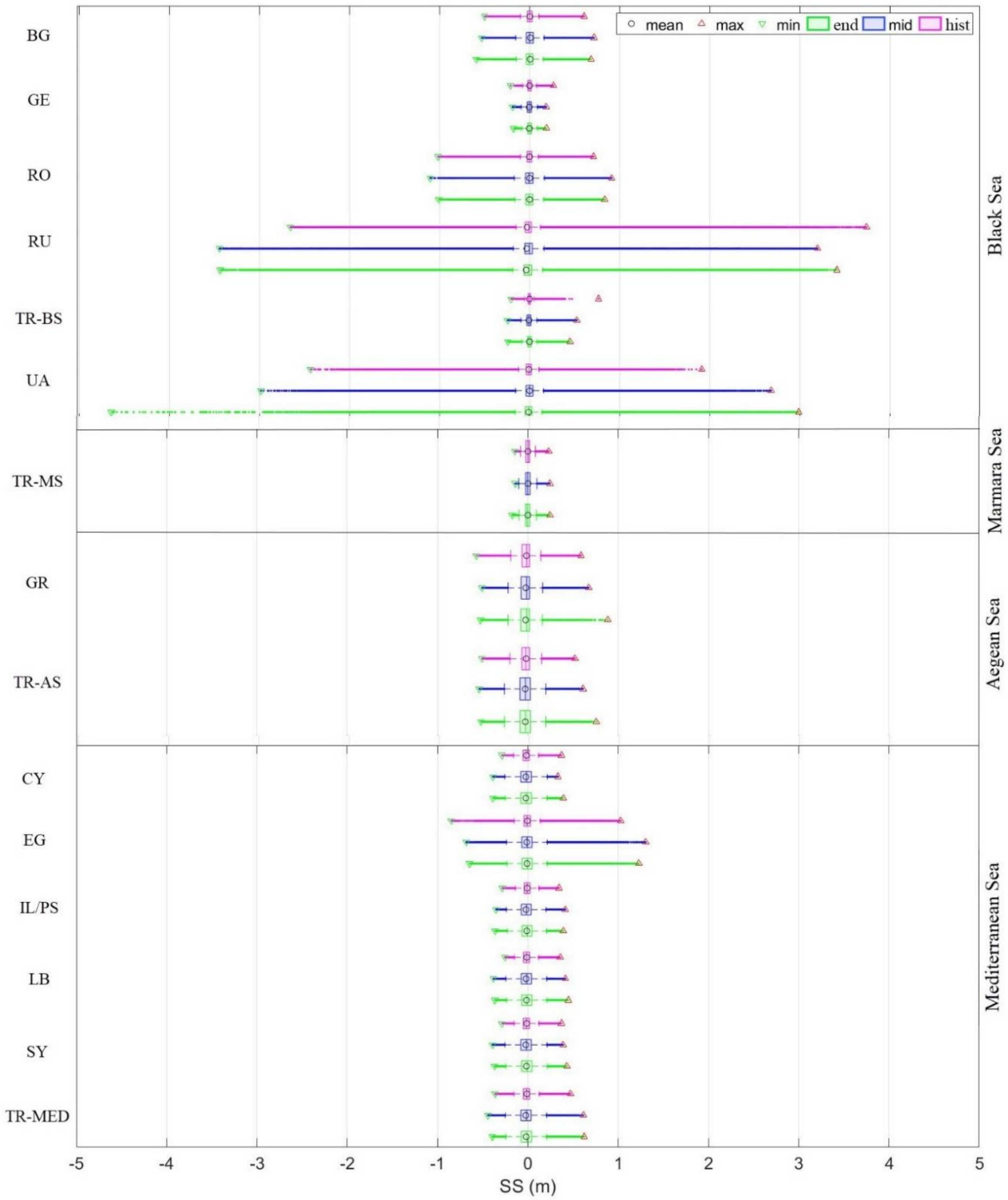

Figure 3.16. SS box plots of the coasts of the countries surrounding the regional seas (Each box contains a vertical line representing the median values), adapted from Uzun and Otay (2025).

Figure 3.17 and Figure 3.18 illustrate the changes in extreme values (RP100) between the historical and end-century periods along the coastlines within the study region. Figure 3.17 highlights the changes in RP100 TWL. The most significant increases are projected for the Ukrainian coasts of the Azov Sea, ranging from -100 mm to +920 mm, indicating that the highest rise in extreme TWL by the end of the century could reach 920 mm above current levels. Along the Black Sea coast, the Romanian shores experience the highest increase, up to 440 mm above present extreme values. In other Black Sea countries, the maximum projected increase in extreme TWL is 430 mm or less (Table 3.4).

For the Mediterranean Sea coast, the Turkish coastline is projected to see the highest increase in extreme TWL by the end of the century, reaching 540 mm above current levels, while other countries in the region may experience increases ranging between 390 mm and 520 mm. The coasts along the Aegean and Marmara Seas are expected to exhibit similar increases of approximately 450 mm.

Mirroring the trends in TWL, the most substantial changes in RP100 SS are also anticipated along the Ukrainian coasts of the Azov Sea, as depicted in Figure 3.18. By the end of the century, extreme SS on the southwestern shores of the Azov Sea could rise by 590 mm above current levels. Conversely, the northern shore of the Azov Sea, also part of Ukraine, may experience a maximum decrease of 480 mm. The Ukrainian Black Sea coast is projected to see variations in extreme SS ranging from -410 mm to +230 mm. In other Black Sea countries, the second maximum projected increase in extreme SS is 160 mm for the Turkish coast, with other nations expecting changes not exceeding -210 mm and 110 mm.

Along the Marmara Sea coasts, SS changes are projected to range from -40 mm to 200 mm. In the Aegean Sea, the Greek coast is expected to experience the highest increase in RP100 SS values, reaching up to 170 mm above current levels, while the Turkish Aegean coast may observe a decrease in extreme SS values. In the Mediterranean Sea, the Turkish coast is projected to have the highest increase in SS values at 230 mm, whereas other countries in the region are not expected to exhibit significant changes.

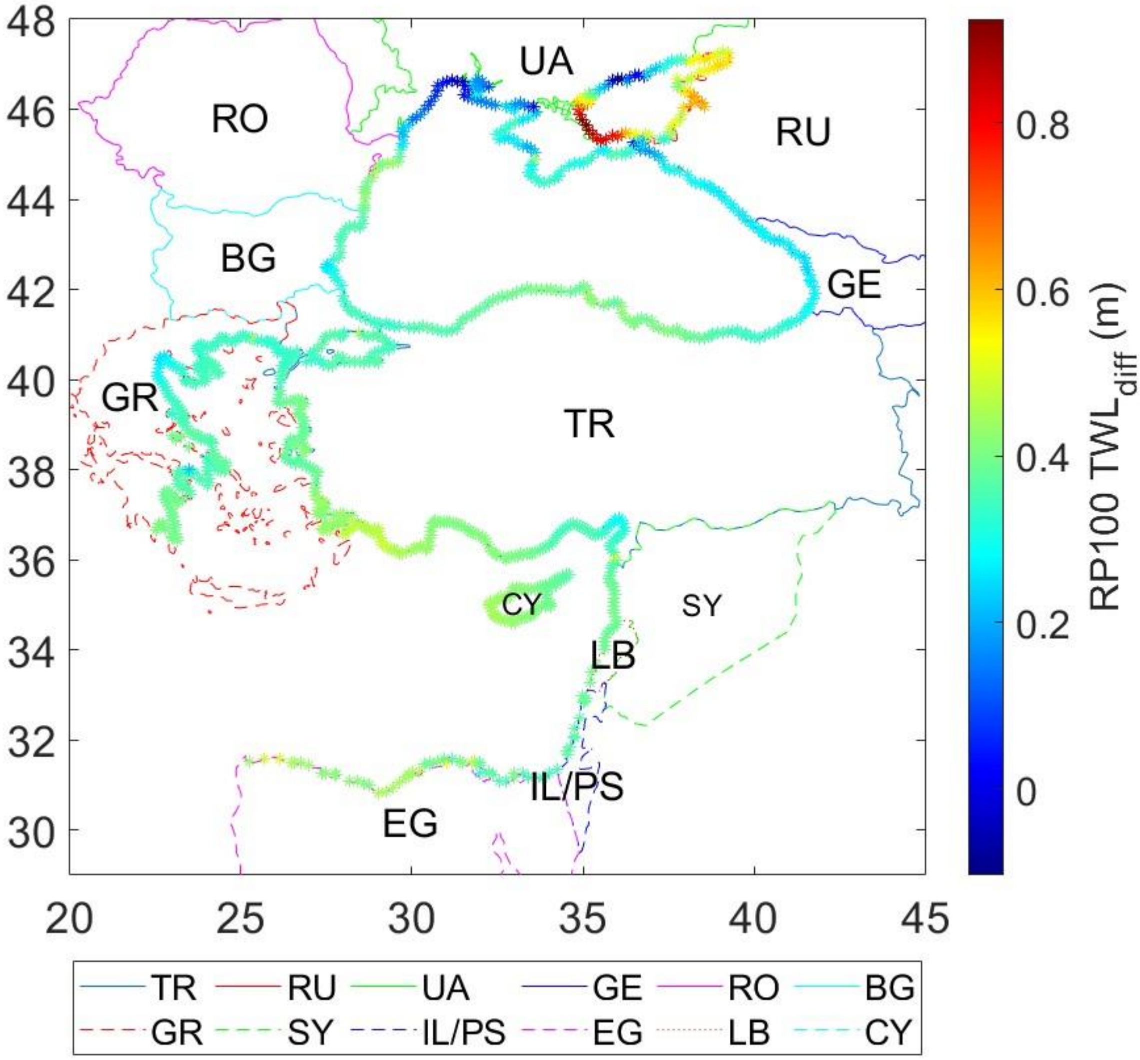

Figure 3.17. Difference of RP100 TWL between the end-century and historical periods along the coastlines, adapted from Uzun and Otay (2025).

Monitoring extreme TWL and SS in coastal areas is crucial, as severe weather systems primarily drive them. Depending on the location, RP100 SS may increase or decrease along the coasts. However, RP100 TWL is projected to increase in all countries, except for certain parts of the Ukrainian coasts along the Black and Azov Seas, where a significant drop in SS values is expected. The largest flood area due to extreme TWL and SS is expected on the southwestern shores of the Azov Sea. In this area, a 112 km low-lying barrier island, the Arabat Spit, may be particularly vulnerable to flooding. Additionally, the Romanian coast, including the Danube River (-0.10 m), the Ukrainian coast with the Dnieper River (-0.25 m), and the Egyptian coast encompassing the Nile River (-0.05 m) (ElKotby et al., 2024) are projected to experience decreases in extreme SS and minimal changes in extreme TWL.

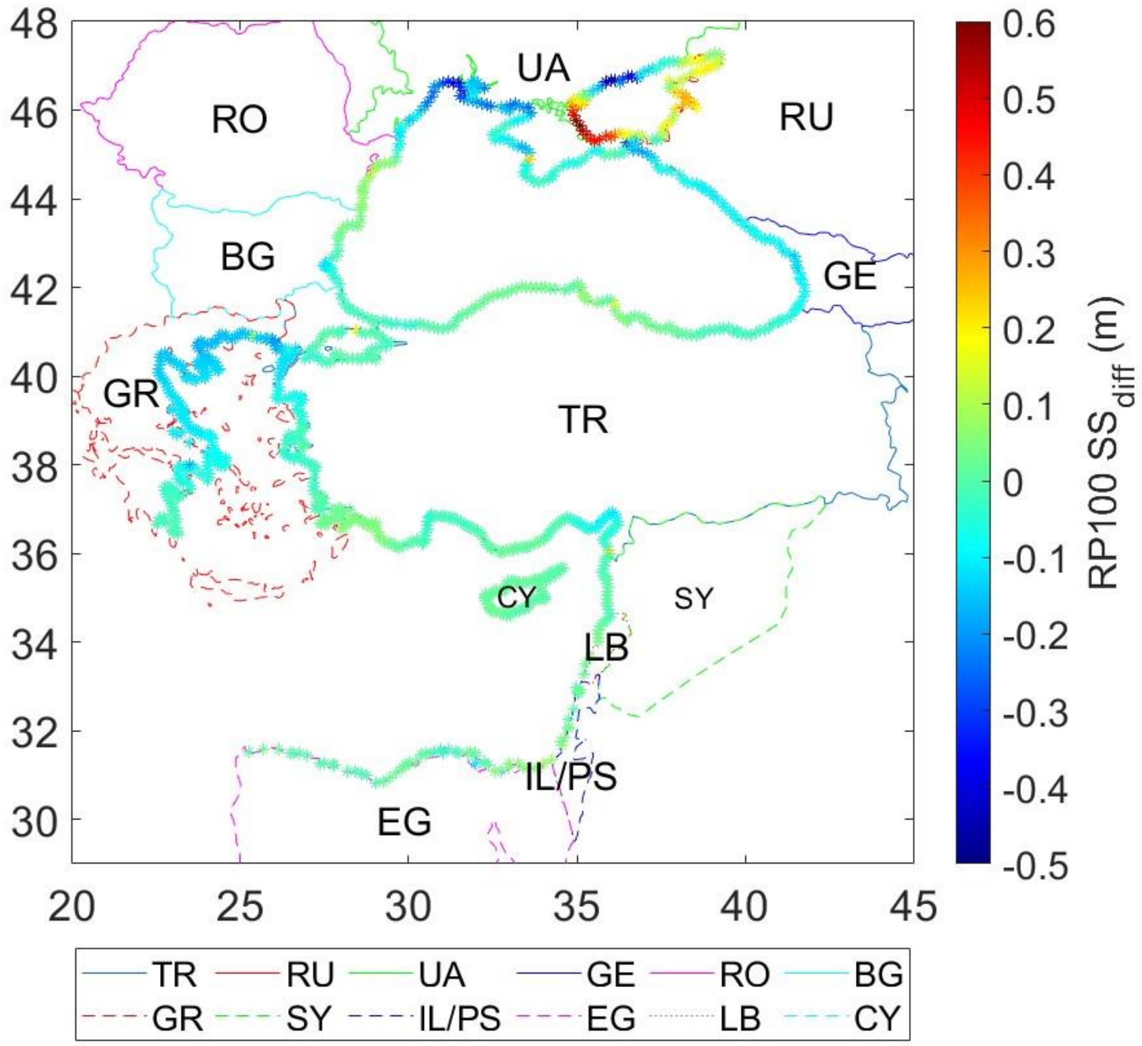

Figure 3.18. Difference of RP100 SS between the end-century and historical periods along the coastlines, adapted from Uzun and Otay (2025).

3.2. Wave Modeling

3.2.1. Calibration Results

To calibrate the wave model forced with the high-resolution DMI-HIRHAM5 RCM wind data, the C_{ds2} coefficient with the Komen scheme for whitecapping and wind input formulations was tested for 10 years between 1986 and 1995 for five different values, which are 0.8E-5, 2.36E-5, 3.0E-5, 3.5E-5, and 4.0E-5. The results of these five different simulations were compared with the ERA5 reanalysis wave data. Error statistics, including bias, ND, RMSE, MAE, SI, and HH index, were spatially evaluated for the Black Sea and the Sea of Azov.

Table 3.4. Differences of RP100 TWL and SS between the end-century and historical periods.

		TWL (mm)		**SS (mm)**	
	Country	**min**	**max**	**min**	**max**
Black Sea	BG	260	380	-110	50
	GE	240	290	-130	-70
	RO	360	440	-30	110
	RU	140	290	-210	-70
	TR-BS	290	420	-70	160
	UA	-70	430	-410	230
Azov Sea	RU	310	640	-30	290
	UA	-100	920	-480	590
Marmara Sea	TR-MS	330	450	-40	200
Aegean Sea	GR	220	480	-210	170
	TR-AS	330	450	-180	40
Mediterranean Sea	CY	370	450	0	30
	EG	340	520	-110	80
	IL/PS	360	390	10	70
	LB	380	400	-20	40
	SY	360	400	-20	20
	TR-MED	280	540	-110	230

Figure 3.19 shows the annual and seasonal means and 99th percentile of ERA5 H_s data in the calibration period. During the calibration period (1986–1995), the annual mean of ERA5 H_s reaches a maximum value of 1.1 m (Figure 3.19d), increasing to 1.3 m during winter (Figure 3.19b). In contrast, the average H_{99}, representing the 99th percentile of H_s, can reach up to 3.6 m over the same period (Figure 3.19a). The highest H_s values are observed in the southwestern part of the Black Sea, and lower values are observed in the

Azov Sea, the northwestern and southeastern regions of the Black Sea, both annual and seasonal evaluations.

Figure 3.20, Figure 3.21, Figure 3.22, Figure 3.23, Figure 3.24, and Figure 3.25 present the spatial error statistics of five different models for the means of annual H_s, H_{99}, and seasonal H_s in DJF, MAM, JJA, and SON, respectively. Table 3.5 includes the overall error statistics of the SWAN model's wave parameters compared to ERA5 reanalysis. As the C_{ds2} coefficient increases from 0.8E-5 to 4.0E-5, the bias for the annual H_s decreases from 0.6 m to -0.1-0.1 m while the ND approaches 0% for almost the entire sea (Figure 3.20). RMSE decreases from 0.3 m to 0.05 m, MAE from 0.16 m to approximately 0 m, SI from 0.6 to 0.05-0.1 m, and HH index from 0.9 to 0-0.1. Similarly, the error statistics for mean H_{99} in Figure 3.21 show a decrease and give the best result for a C_{ds2} value of 4.0E-5. However, extreme values, H_{99}, resulted in slightly higher overall error statistic values compared to those of annual mean H_s (Table 3.5). Nevertheless, Table 3.5 also proves that the calibration improved the wave model at the Black and Azov Seas by about a factor of 10. As a result of calibration in H_s and H_{99}, the wave model is very effectively improved in the Black Sea, while a negligible underestimation occurs in the Sea of Azov.

Figure 3.20 and Figure 3.21 show that H_{99} is overestimated more than the annual mean H_s. In other words, the extreme value performance of the wave model is more prone to overestimation. This was also observed in the seasonal analysis. As seen in Figure 3.22, winter has more extreme H_s values than other seasons. In spring (Figure 3.23), summer (Figure 3.24), and autumn (Figure 3.25), the maximum H_s bias was about 0.5 m, while in winter (Figure 3.22) it reached 0.9 m. Overestimation of extreme values was also observed in ND, RMSE, MAE, SI, and HH index values. In the case of C_{ds2} 4.0E-5, these error indicators reached the optimum state, showing slight overestimation and underestimation in the Black Sea and the Sea of Azov, respectively.

In the calibration process, the performance of the wave model with the different C_{ds2} values in terms of the T_m was assessed in addition to H_s and H_{99}. ERA5 reanalysis annual mean T_m data, shown in Figure 3.26, was utilized to calibrate the model, and the results were presented in Figure 3.27. According to Figure 3.26, the annual mean of T_m from ERA5 for the Black and Azov Seas varies between 2.2 and 3.6 s. The highest values are observed in the southwestern region of the Black Sea, whereas the lower values, below 3 seconds, are observed in the Sea of Azov and the northwestern coast of the Black Sea.

Figure 3.27 illustrates the spatial error statistics of the annual mean T_m between the SWAN results and ERA5 data, following a format similar to the H_s and H_{99} analyses. As the C_{ds2} coefficient increases, the maximum bias for the annual Black Sea mean T_m decreases from 0.3 s to 0.1 s, observed in deeper regions, while the negative bias in the Sea of Azov slightly increases, as shown in Figure 3.27. Basin-averaged RMSE, MAE, and HH index of T_m slightly improved while basin-averaged bias, ND, and SI did not. In addition to the spatially distributed error statistics, the purpose of analyzing Table 3.5 was to look at the basin-averaged results to decide where to stop the calibration.

Table 3.5 shows that as the C_{ds2} value increases, H_s and H_{99} still improve, albeit more slowly, but T_m worsens or does not improve further. Therefore, considering the basin-averaged error statistics of H_s, H_{99}, and T_m, an unweighted normalized decision matrix (Table 3.6) is constructed to choose the C_{ds2} value for the best-performing SWAN model forced with DMI-HIRHAM5 wind data. A normalized scoring approach, where each variable's error metrics are scaled from 1 (worst) to 5 (best), is applied to the error statistics. The models are ranked based on the unweighted average of these scaled scores. According to these ranking values, the model result with C_{ds2} value of 4.0E-5 is chosen as the best performing model with the ranking value of 4.61.

While calibrating the model, it was also examined how the annual θ_m changed according to the C_{ds2} coefficient. Figure 3.28 shows the ERA5 annual mean θ_m and the shortest distances between the wave model and ERA5 data according to the five C_{ds2} values. The black and magenta arrows in this figure show the directions of ERA5 θ_m and SWAN θ_m, respectively, while the colormap shows the shortest angular distance between these two directions. If the angle between these two directions is clockwise, it shows a positive difference, if it is counterclockwise, it shows a negative difference. As seen in Figure 3.28b-f, the annual θ_m shows an improvement with the higher C_{ds2} value. The noticeable improvements are observed especially northern coasts of the Black Sea. With the angular distance between -40° and 40°, the model with the C_{ds2} value of 4.0E-5 shows the best accuracy.

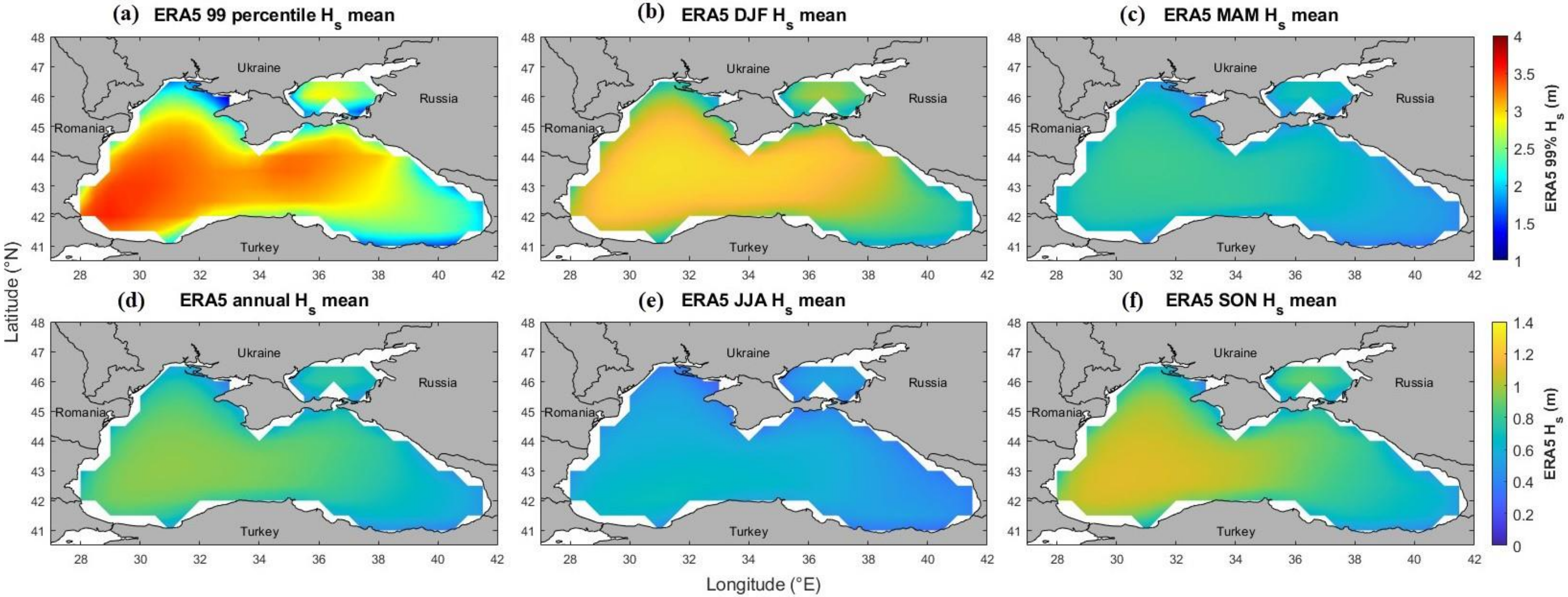

Figure 3.19. ERA5 annual means of (a) H_{99}, (b) H_s in winter, (c) H_s in spring, (d) annual H_s, (e) H_s in summer, and (f) H_s in autumn for 1986-1995.

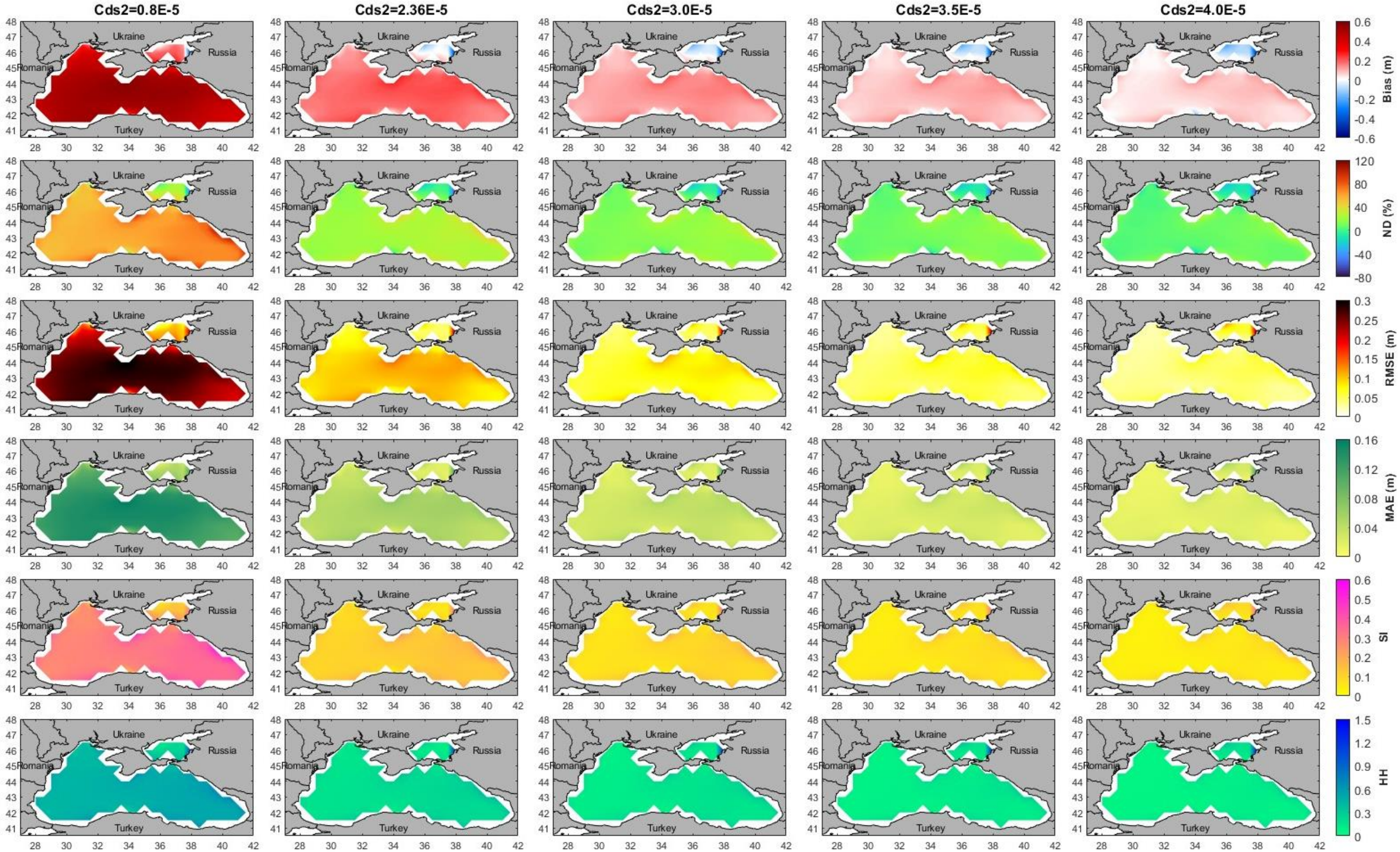

Figure 3.20. Bias, ND, RMSE, MAE, SI, and HH index between the annual means of H_s of five simulations and ERA5 for 1986-1995.

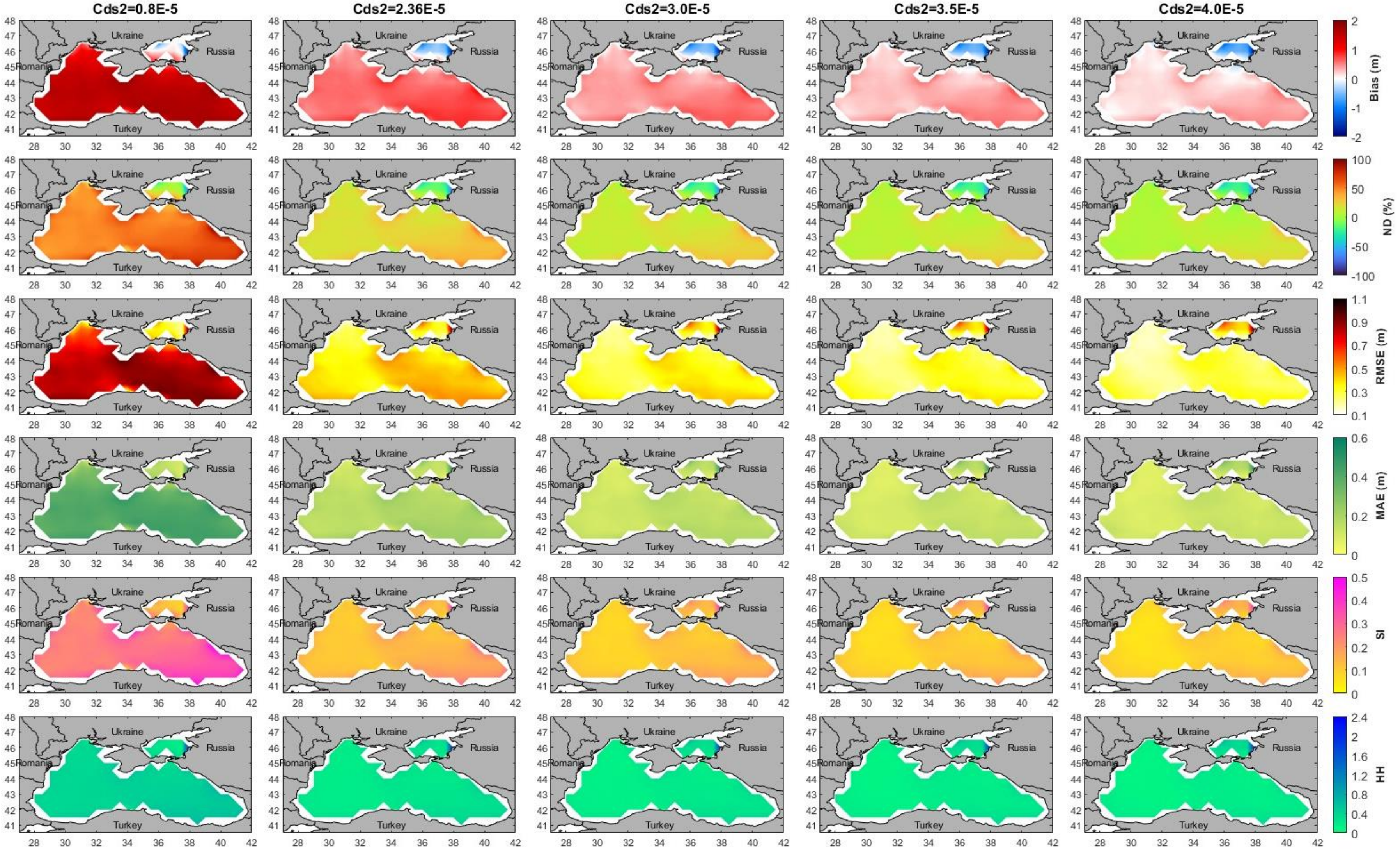

Figure 3.21. Bias, ND, RMSE, MAE, SI, and HH index between the annual means of H_{99} of five simulations and ERA5 for 1986-1995.

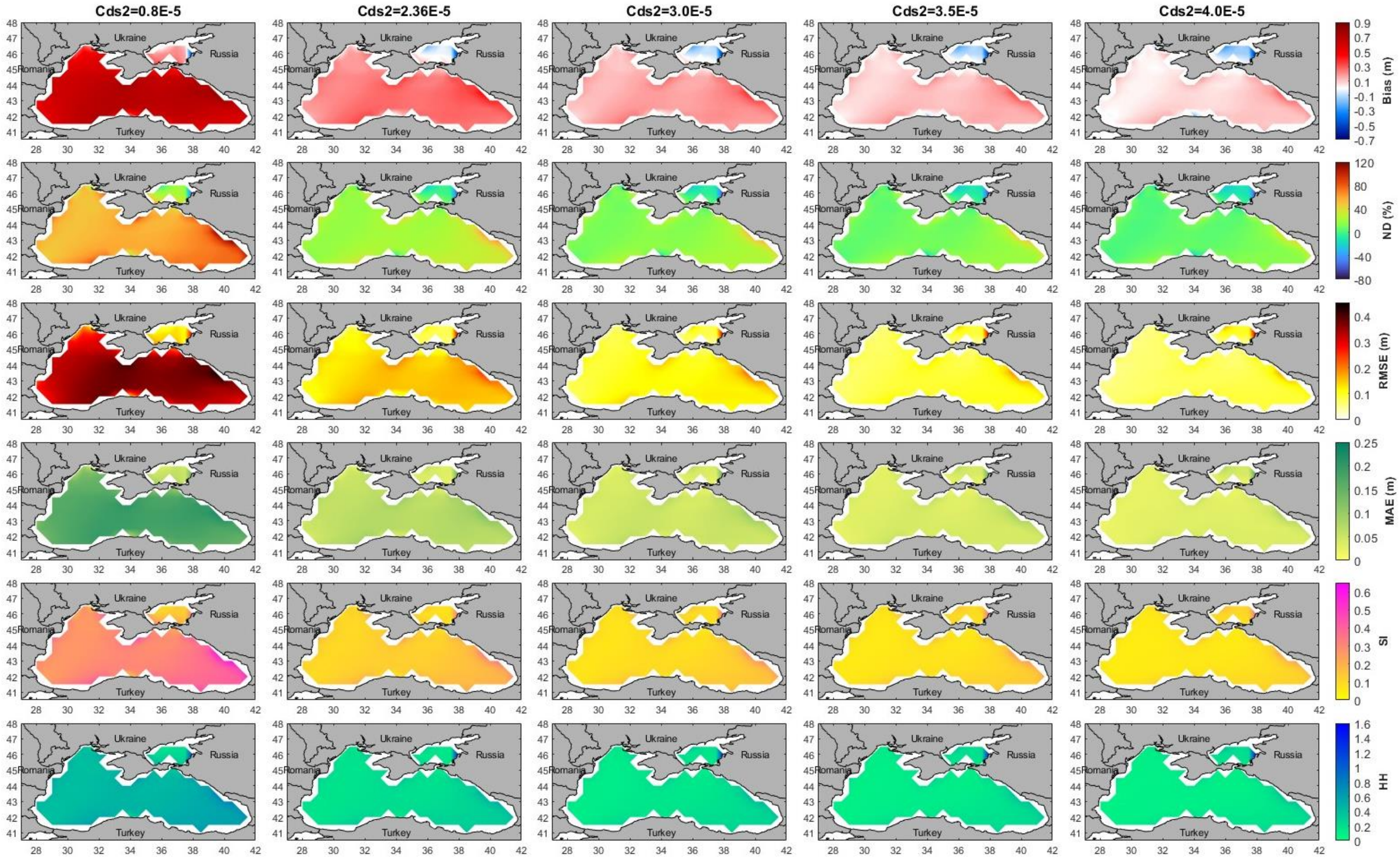

Figure 3.22. Bias, ND, RMSE, MAE, SI, and HH index between the DJF means of H_s of five simulations and ERA5 for 1986-1995.

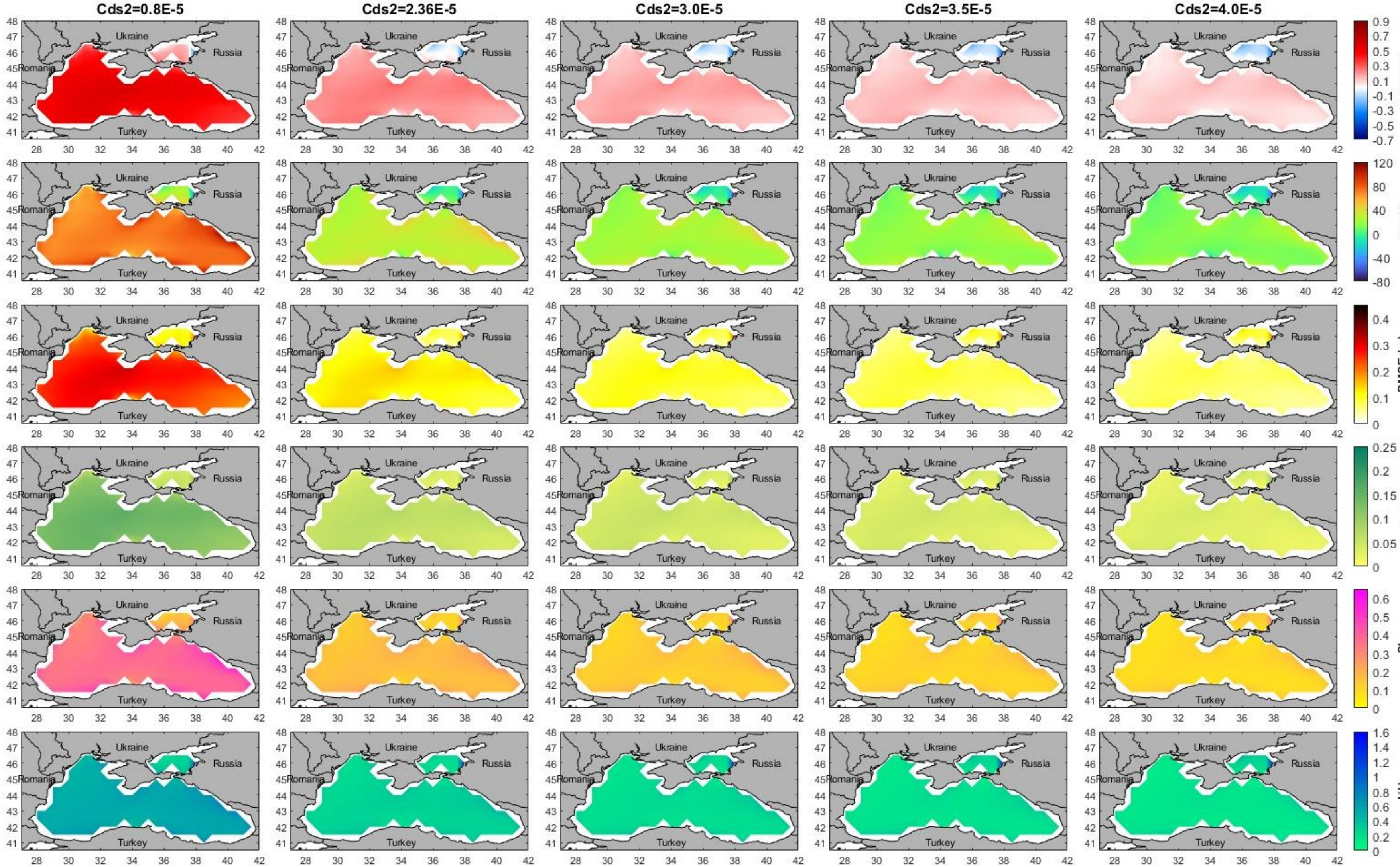

Figure 3.23. Bias, ND, RMSE, MAE, SI, and HH index between the MAM means of H_s of five simulations and ERA5 for 1986-1995.

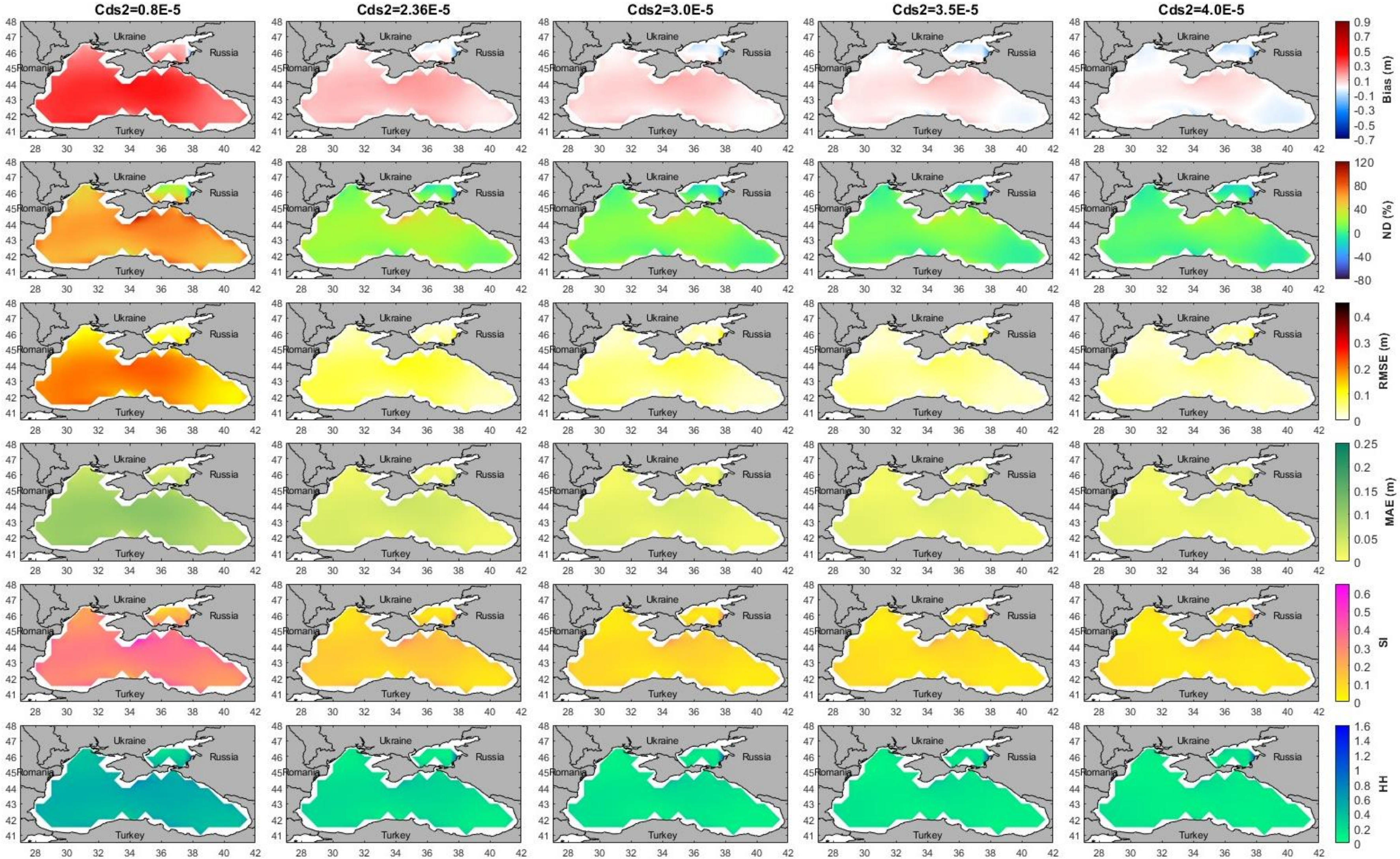

Figure 3.24. Bias, ND, RMSE, MAE, SI, and HH index between the JJA means of H_s of five simulations and ERA5 for 1986-1995.

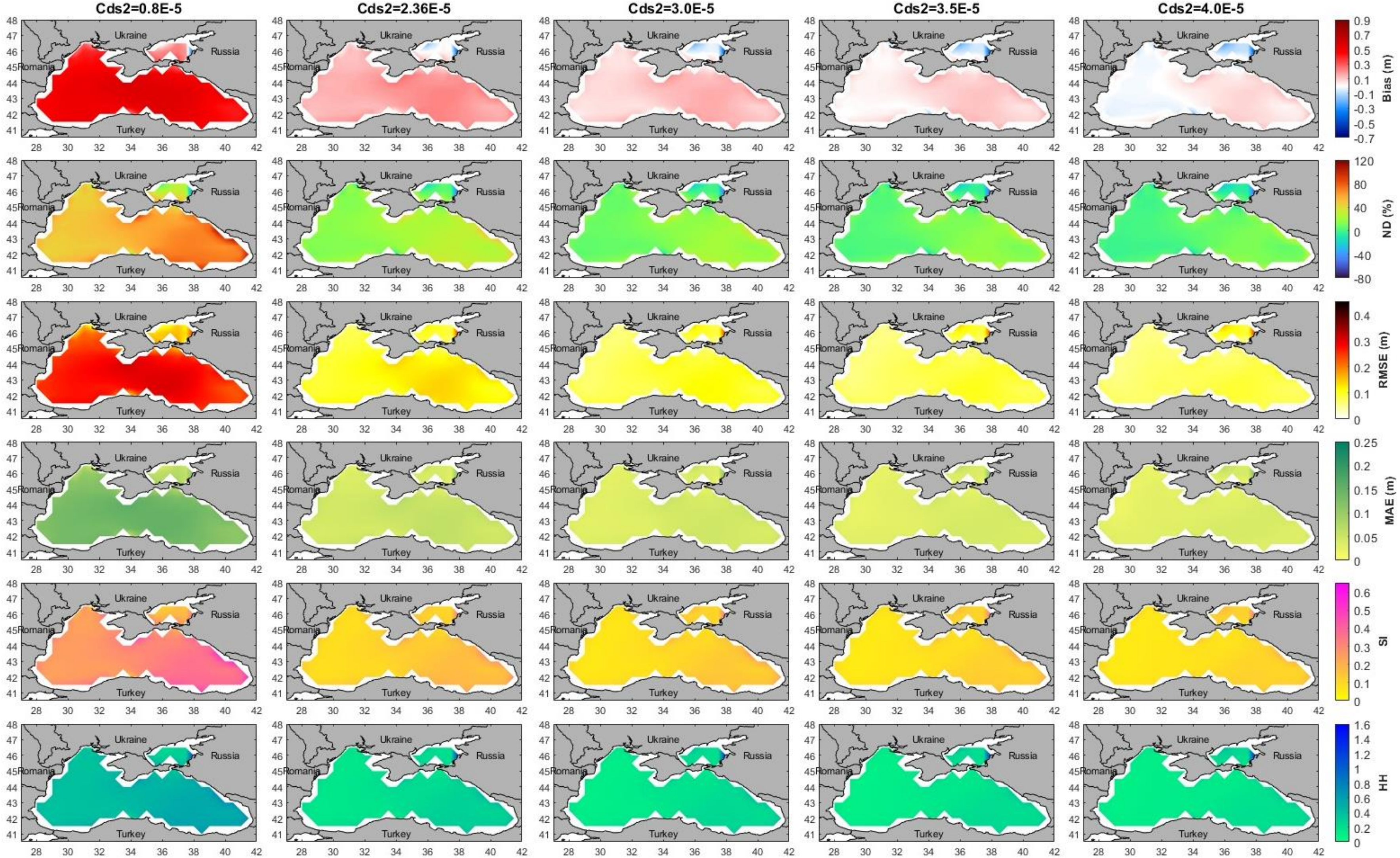

Figure 3.25. Bias, ND, RMSE, MAE, SI, and HH index between the SON means of H_s of five simulations and ERA5 for 1986-1995.

Table 3.5. Basin-averaged error statistic of SWAN model wave parameters compared to ERA5 reanalysis. The values in bold correspond to the best error metric values.

		C_{ds2} (E-5)	Bias (m or s)	ND (%)	RMSE (m or s)	MAE (m or s)	SI	HH Index
Calibration (1986-1995)	**H_s**	0.8	0.45	59.14	0.24	0.12	0.31	0.47
		2.36	0.16	21.60	0.09	0.05	0.12	0.22
		3.0	0.10	14.21	0.07	0.03	0.09	0.17
		3.5	0.07	9.62	0.05	**0.02**	0.07	0.14
		4.0	**0.04**	**5.74**	**0.04**	**0.02**	**0.06**	**0.11**
	H_{99}	0.8	1.35	50.06	0.77	0.38	0.28	0.44
		2.36	0.54	21.07	0.40	0.17	0.15	0.27
		3.0	0.37	14.81	0.34	0.14	0.12	0.23
		3.5	0.25	10.83	0.30	0.12	0.11	0.21
		4.0	**0.16**	**7.43**	**0.27**	**0.11**	**0.10**	**0.19**
	T_m	0.8	0.04	1.02	0.10	0.05	0.03	0.06
		2.36	**0.01**	**-0.10**	0.09	**0.04**	0.03	0.06
		3.0	**-0.01**	-0.62	**0.08**	**0.04**	0.03	**0.05**
		3.5	-0.02	-1.01	**0.08**	**0.04**	0.03	**0.05**
		4.0	-0.03	-1.38	**0.08**	**0.04**	**0.02**	**0.05**
Validation (1996-2005)	**H_s**	4.0	0.01	2.09	0.04	0.02	0.06	0.11
	H_{99}		0.17	7.23	0.24	0.10	0.09	0.18
	T_m		-0.10	-3.27	0.10	0.04	0.03	0.06

In summary, the wave parameters in the SWAN model with the default and small C_{ds2} values are generally overestimated. Improvement in the wave parameters was observed as the C_{ds2} coefficient increased, as illustrated by the annual and seasonal spatial error analyses and basin-averaged error statistics. The best-calibrated model for all error parameters was observed when the C_{ds2} value was 4.0E-5.

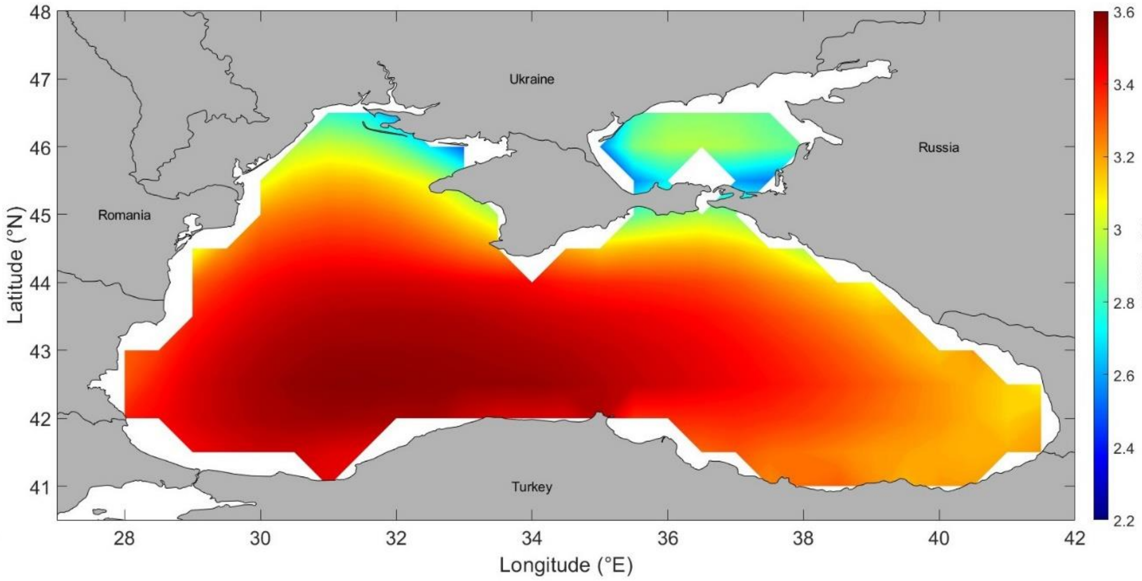

Figure 3.26. Mean T_m of ERA5 for 1986-1995.

3.2.2. Validation Results

To evaluate the calibrated wave model forced with the high-resolution DMI-HIRHAM5 RCM wind data, the C_{ds2} value of 4.0E-5 with the Komen scheme was tested for 10 years between 1996 and 2005. The results of the validation simulation were compared with the ERA5 reanalysis wave data. The error statistics were spatially evaluated for the Black Sea and the Sea of Azov.

Figure 3.29 shows the annual, 99th percentile, and seasonal H_s means of ERA5 wave data in the validation period. During the validation period (1996–2005), the annual mean ERA5 H_s reaches a maximum value of 1.2 m (Figure 3.29d), increasing to 1.4 m during winter (Figure 3.29b). In contrast, the average H_{99} can reach up to 3.5 m over the same period (Figure 3.29a). The highest and lowest H_s values are observed in the same regions as in the calibration period.

Figure 3.30 presents the spatial error statistics of the wave model results for the averages of annual H_s and seasonal H_s in DJF, MAM, JJA, and SON in the validation period. As mentioned in the calibration results, error statistics are slightly higher in winter. The bias values of the mean annual H_s range between -0.1 and 0.1 m. The bias is between -0.1 and 0.2 m in spring, summer, and autumn, while it is between -0.2 and 0.3 m in winter. ND, RMSE, MAE, SI, and HH index values range between -40-40%, 0-0.2 m, 0-0.1 m, 0-0.2, and 0-0.4 in seasonal and annual evaluations, respectively. In most of the study area, these error parameters are close to 0 except in the northern Azov Sea and the eastern coasts of the Black Sea. The coarse-resolution wind data can explain the higher error indicators in these regions. In Table 3.5, the overall error parameters are also shown. They are 0.01 m, 2.09%, 0.04 m, 0.02 m, 0.06, and 0.11 for the bias, ND, RMSE, MAE, SI, and HH index of the mean annual H_s, respectively, which are better than or the same as the calibration period's results with C_{ds2} 4.0E-5.

Table 3.6. Ranking of the basin-averaged error statistic using an unweighted decision matrix.

	C_{ds2} (E-5)	Bias	ND	RMSE	MAE	SI	HH Index	Avg Rank
H_s	**0.8**	1	1	1	1	1	1	1
	2.36	2	2	2	2	2	2	2
	3.0	3	3	3	3	3	3	3
	3.5	4	4	4	4	4	4	4
	4.0	5	5	5	5	5	5	5
H_{99}	**0.8**	1	1	1	1	1	1	1
	2.36	2	2	2	2	2	2	2
	3.0	3	3	3	3	3	3	3
	3.5	4	4	4	4	4	4	4
	4.0	5	5	5	5	5	5	5
T_m	**0.8**	1	2	1	1	1	1	1
	2.36	5	5	2	5	1	1	3
	3.0	5	4	5	5	1	5	4
	3.5	3	3	5	5	1	5	4
	4.0	2	1	5	5	5	5	4
	C_{ds2} **(E-5)**	**0.8**	**2.36**	**3.0**	**3.5**	**4.0**		
	Overall Rank	1.06	2.39	3.39	3.89	4.61		

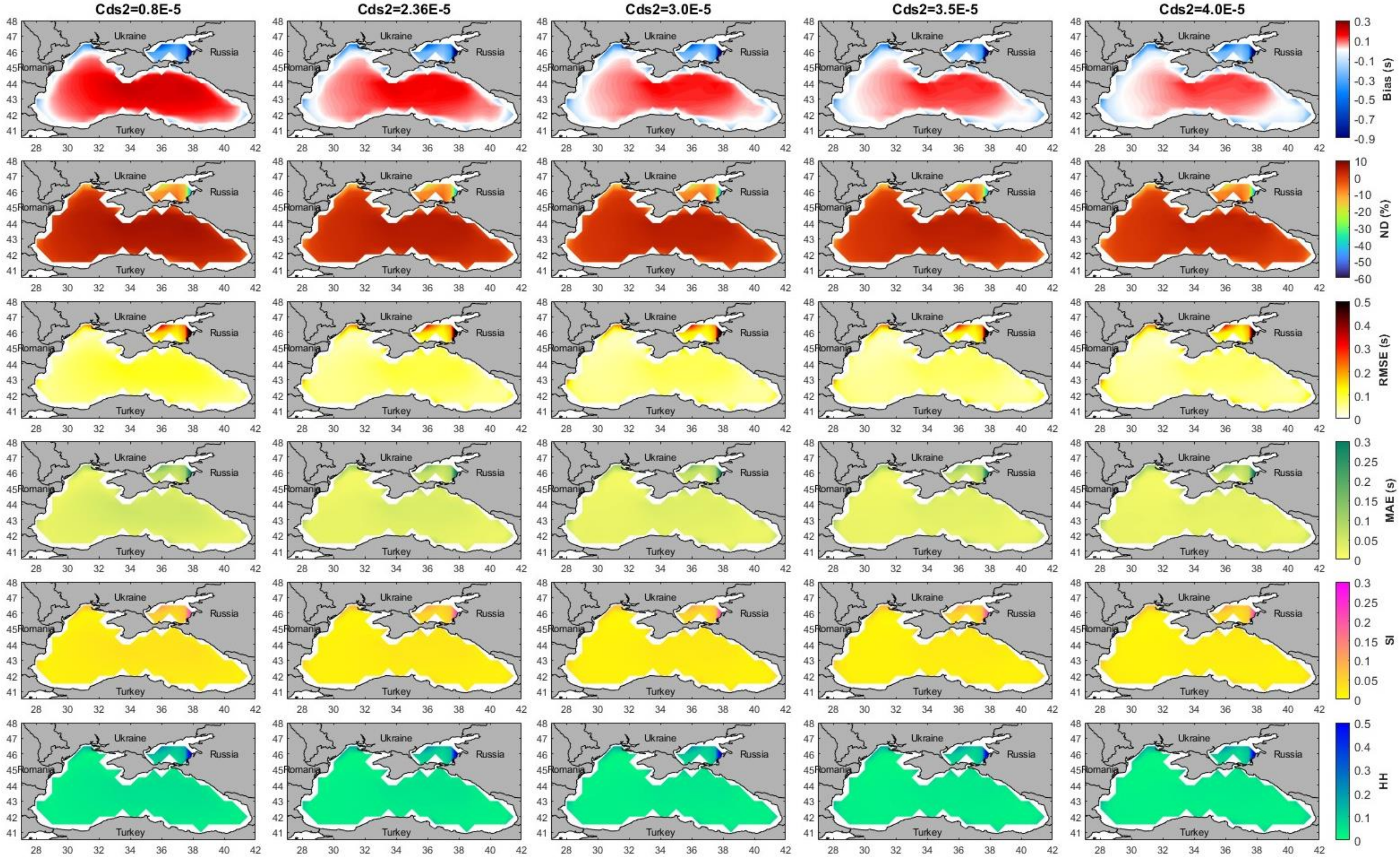

Figure 3.27. Bias, ND, RMSE, MAE, SI, and HH index between the mean T_m of five simulations and ERA5 for 1986-1995.

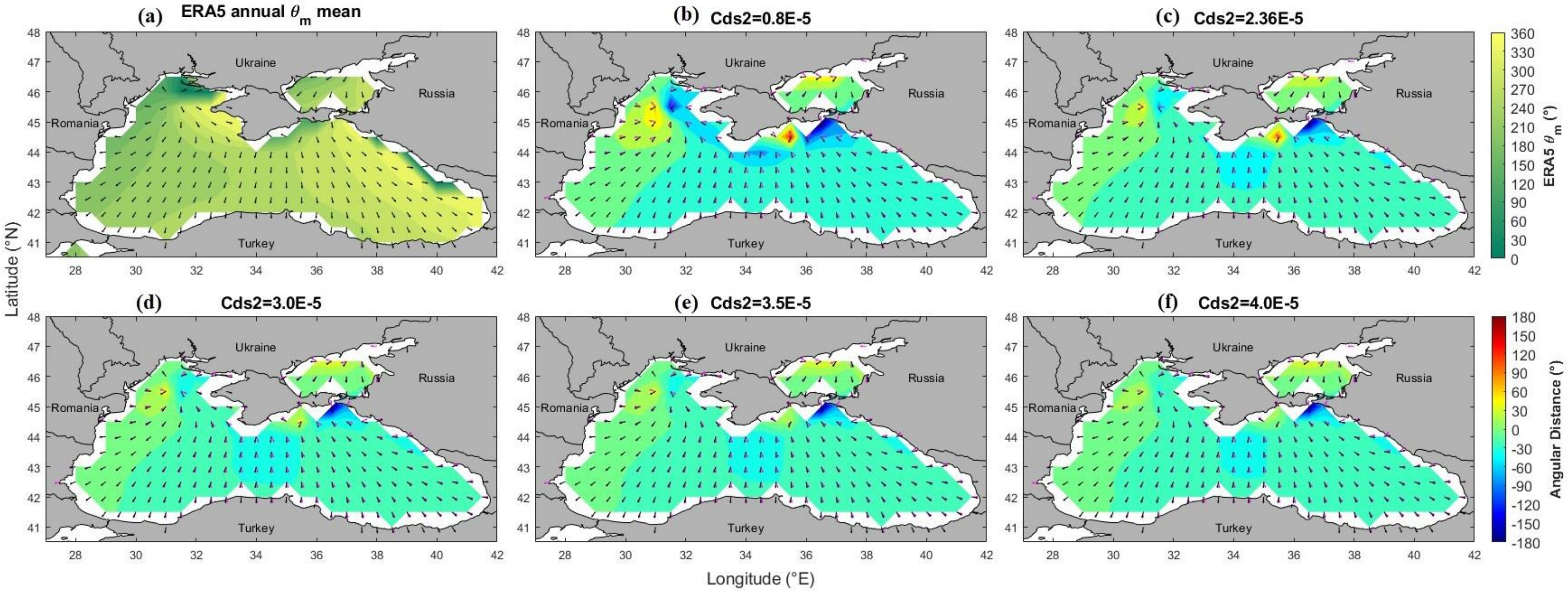

Figure 3.28. (a) ERA5 annual mean θ_m and the shortest angular distances of the model with C_{ds2} values (b) 0.8E-5, (c) 2.36E-5, (d) 3.0E-5, (e) 3.5E-5, and (f) 4.0E-5 compared to ERA5 for 1986-1995.

Figure 3.31 presents the spatial error statistics of the wave model results for the averages of annual H_{99} in the validation period. As mentioned in the calibration results, error statistics are slightly higher in H_{99} compared to the annual mean of H_s. The bias values of the annual mean H_{99} range between -0.5 and 0.5 m. ND, RMSE, MAE, SI, and HH index values range between -40-40%, 0-0.6 m, 0-0.3 m, 0-0.4, and 0-0.8, respectively. The overall error parameters are 0.17 m, 7.23%, 0.24 m, 0.10 m, 0.09, and 0.18 for the bias, ND, RMSE, MAE, SI, and HH index of the mean annual H_{99}, respectively, which are almost the same as the calibration period's results with C_{ds2} 4.0E-5 (Table 3.5).

The average ERA5 T_m data of the evaluation period, shown in Figure 3.32, was utilized to evaluate the calibrated model's T_m. The 10-year annual mean Tm from ERA5 for the Black and Azov Seas varies between 2 and 3.6 s. The highest values are observed in the southwestern region of the Black Sea, whereas the lower values, below 3 seconds, are observed in the Sea of Azov and the northwestern coast of the Black Sea. Figure 3.33 illustrates the spatial error statistics of the annual mean T_m between the SWAN results and ERA5 data. The bias ranges between -0.9 and 0.1 s and indicates overall underestimation except for the deeper regions. ND, RMSE, MAE, SI, and HH index values are between -20-10%, 0-0.4 s, 0-0.3 s, 0-0.2, and 0-0.4, respectively. The overall bias, ND, RMSE, MAE, SI, and HH index are -0.10 s, -3.27%, 0.10 s, 0.04 s, 0.03, and 0.06, respectively (Table 3.5).

The mean of annual ERA5 θ_m and the validation of the calibrated wave model, as the shortest angular distance between the SWAN result and ERA5 data, are shown in Figure 3.34. The black and magenta arrows in this figure show the directions of ERA5 θ_m and SWAN θ_m, respectively, while the colormap shows the shortest angular distance between these two directions. If the angle between these two directions is counterclockwise and clockwise, it shows negative and positive angular distances. As seen in Figure 3.34, the angular differences at most of the basin, ranging between -30° and 30°, are comparable to the calibration results, except the northern part of the Black Sea, which has the angular distances from -90° up to 90°.

As a result of the validation, the wave parameters in the calibrated SWAN model are generally consistent with the ERA5 reanalysis data. The best agreement was found for H_s, and a sufficient agreement was found for H_{99}, T_m, and θ_m. The discrepancies between the

SWAN model results and ERA5 reanalysis data can be attributed to the low resolution of the ERA data. Since the resolution of SWAN wave data are more than six times higher than that of ERA5, the effect of wave transformation processes, such as refraction and diffraction as the wave propagates to the shore, is better reflected in the SWAN model. In addition, the Azov Sea may not be well represented in the ERA data due to the lack of sufficient resolution.

3.2.3. Wave Projection Results

In the future period (2071-2100, FW30), wave projection was performed using DMI-HIRHAM5 RCM wind data and spatial and temporal TWL data (Yan et al. 2020b) produced using the same wind. Before the wave projection results, since the change in winds is one of the biggest factors affecting wave generation, the annual average and 99th percentile U_{10} changes between FW30 and PW20 were analyzed. The annual averages and 99th percentiles of the FW30 wave parameters were calculated and compared with those at PW20.

Figure 3.35 shows the annual mean and 99th percentile U_{10} and the changes between FW30 and PW20. During the FW30 period, the annual average U_{10} exhibits an increase of approximately 2%, while the 99th percentile U_{10} experiences a more pronounced rise of up to 20%. The highest 99th percentile U_{10} values, reaching speeds of 18 m/s, are observed in the western and central Black Sea. The strongest winds occur during the DJF and SON seasons in both periods.

In DJF, the annual and 99th percentile U_{10} averages show increases ranging from 2% to 10%. Conversely, SON generally displays a decline, with decreases between -2% and -10%. During MAM, the 99th percentile U_{10} increases by up to 12% in the western and central Black Sea regions, while a slight decrease of up to -8% is observed in the southeastern Black Sea. In JJA, the mean 99th percentile U_{10} is projected to rise by up to 10% in the FW30 period, though a decrease of up to -8% is anticipated in the southwestern and near-southwestern coastal areas.

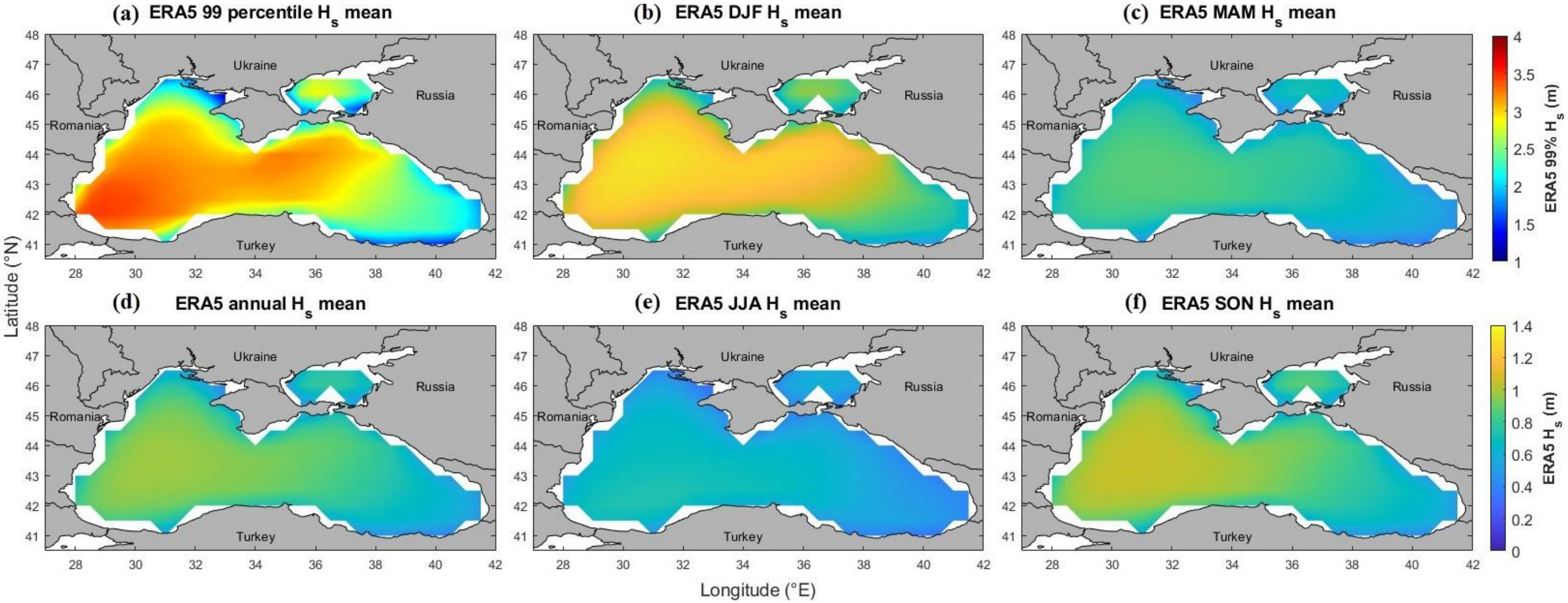

Figure 3.29. ERA5 annual means of (a) H_{99}, (b) H_s in winter, (c) H_s in spring, (d) annual H_s, (e) H_s in summer, and (f) H_s in autumn 1996-2005.

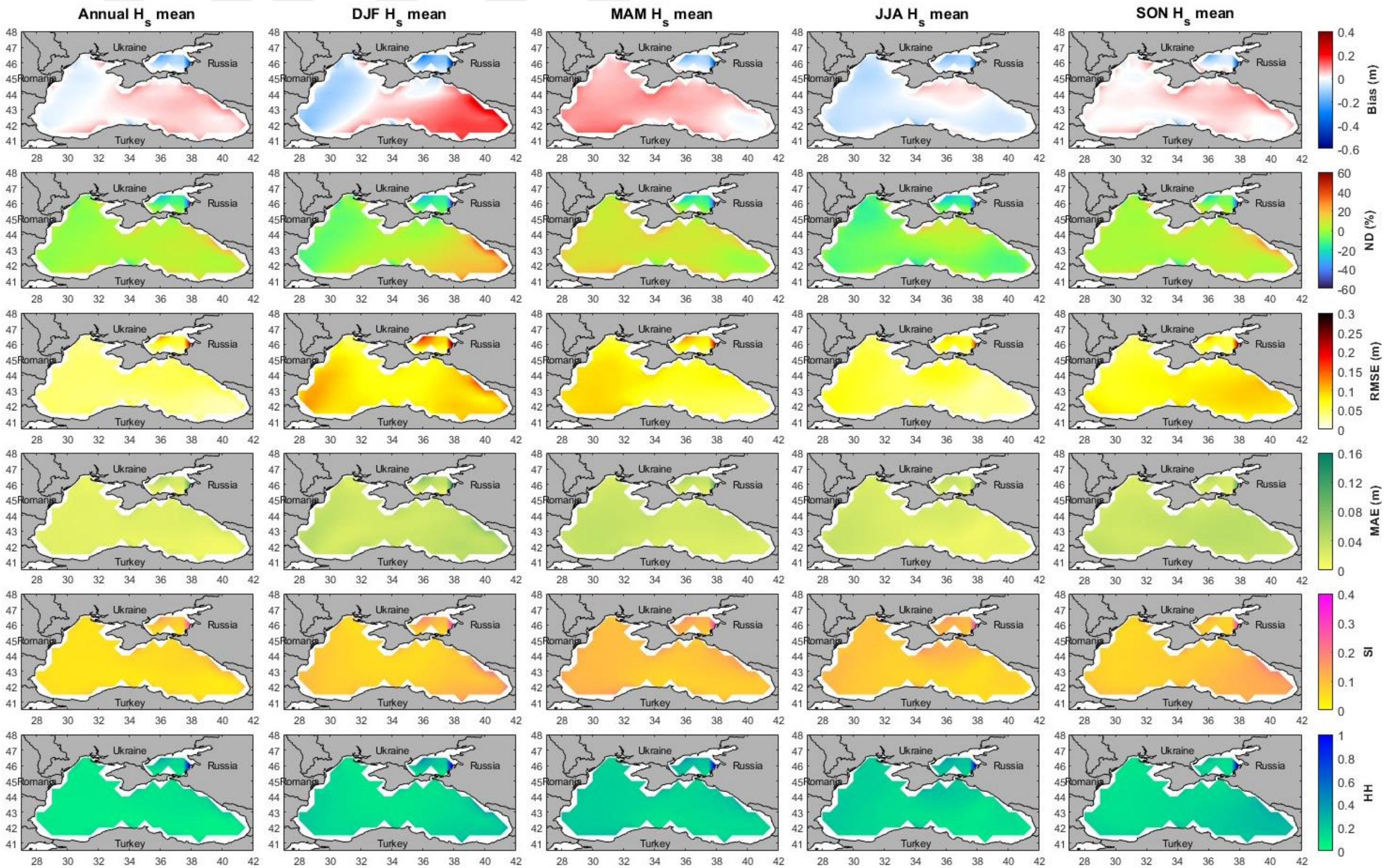

Figure 3.30. Bias, ND, RMSE, MAE, SI, and HH index of the means of annual and seasonal H_s for 1996-2005.

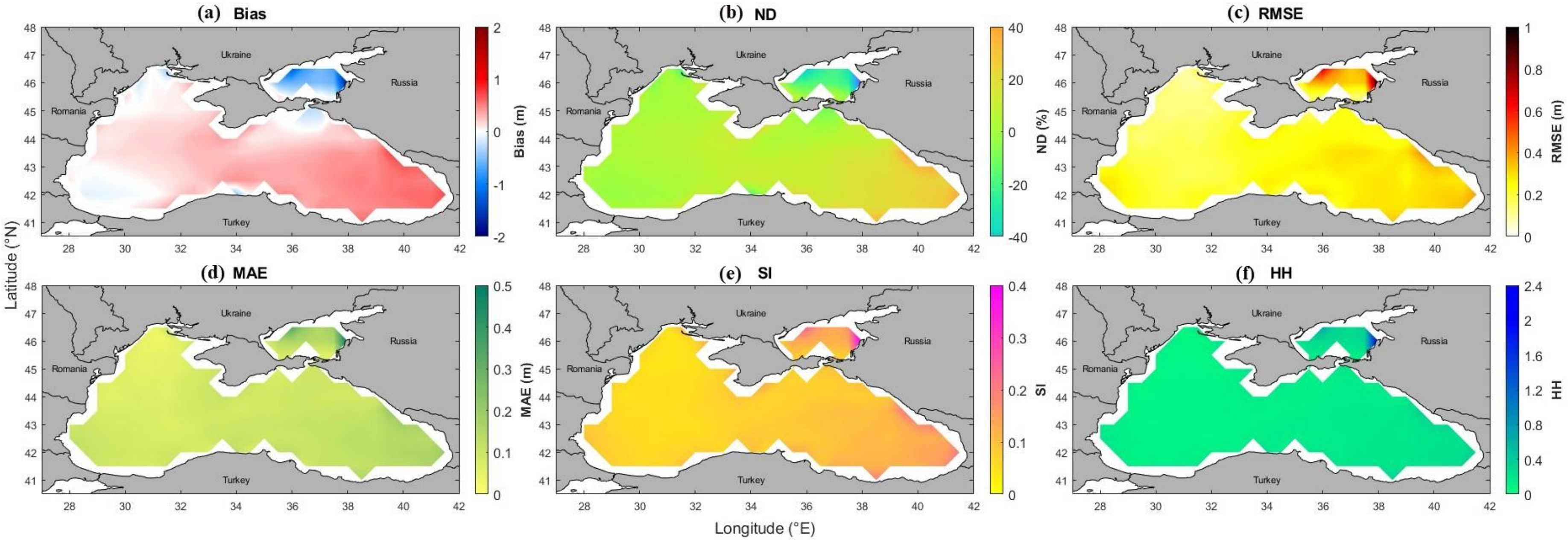

Figure 3.31. (a) Bias, (b) ND, (c) RMSE, (d) MAE, (e) SI, and (f) HH index between the H_{99} means of the simulation and ERA5 for 1996-2005.

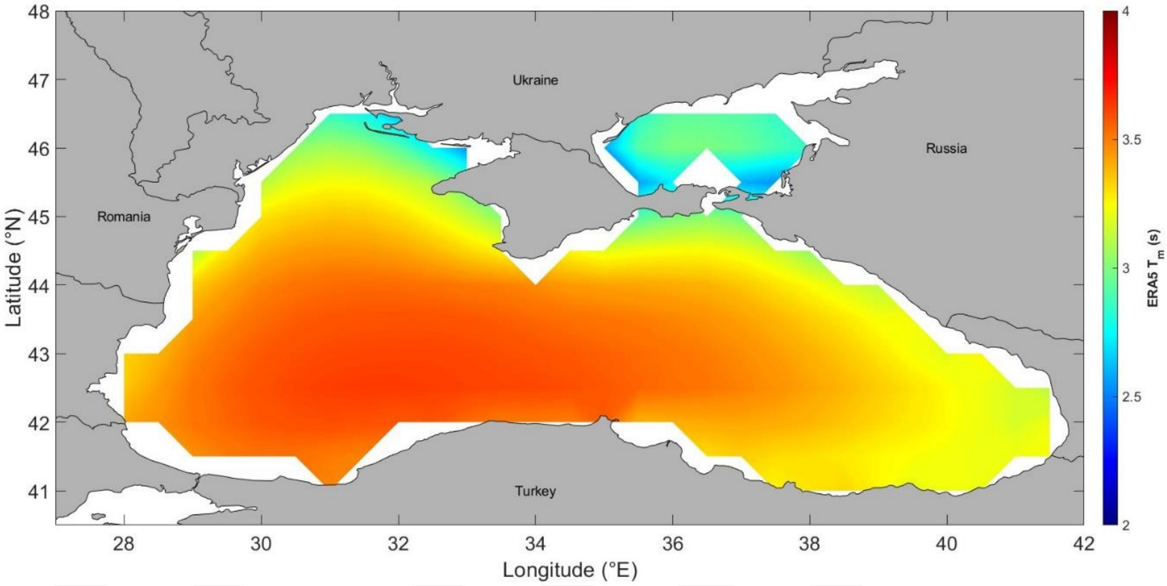

Figure 3.32. ERA5 annual mean T_m for 1996-2005.

While no significant changes are expected in the mean U_{10} values, notable shifts are projected in the extreme U_{10} values, highlighting the increasing variability and intensity of wind patterns in the FW30 period.

Figure 3.36 presents the annual average H_s for the PW20 and FW30 periods, along with the ND between the two periods on annual and seasonal scales. The maximum annual mean H_s is approximately 1 m during PW20, increasing to 1.2 m in FW30.

The most substantial increase occurs in summer, while a slight decrease is observed in autumn. A pronounced rise in H_s is also projected across the entire Sea of Azov during summer. In winter, an increase is notable in the western half of the Black Sea, whereas a slight decrease is evident along the southeastern nearshore. During spring, overall changes are minimal, though significant increases are observed along the Romanian and Ukrainian coasts of the Black Sea, as well as the eastern (Russian) and northwestern (Ukrainian) coasts of the Sea of Azov.

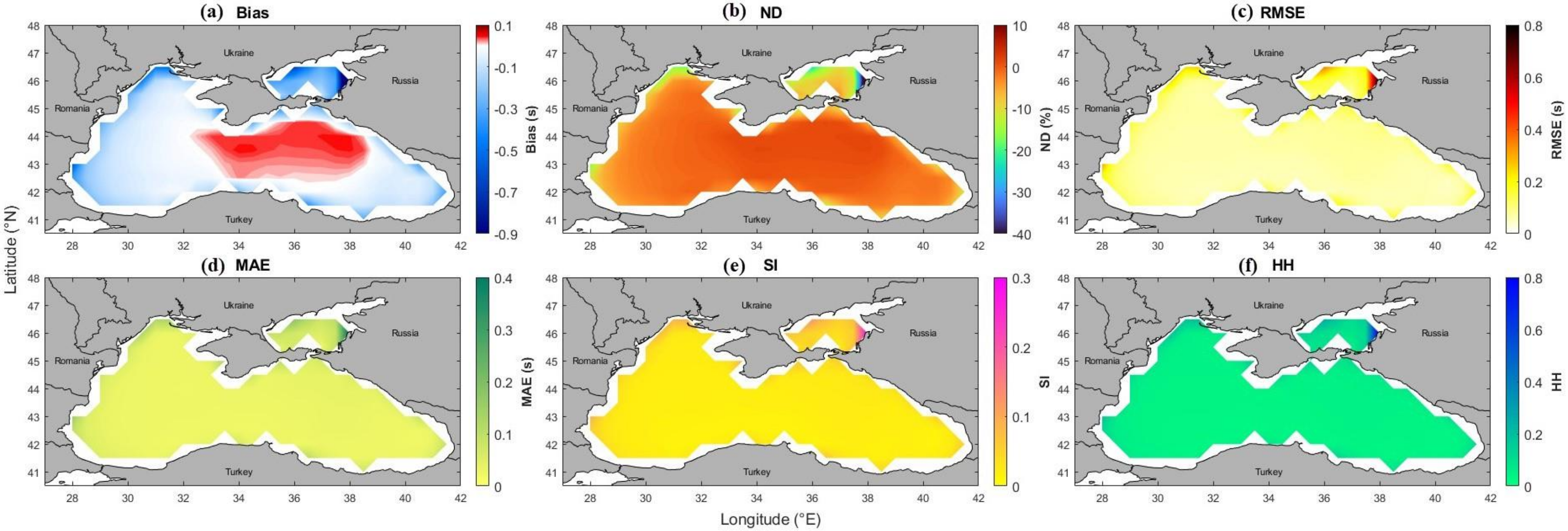

Figure 3.33. (a) Bias, (b) ND, (c) RMSE, (d) MAE, (e) SI, and (f) HH index between the T_m means of the simulation and ERA5 for 1996-2005.

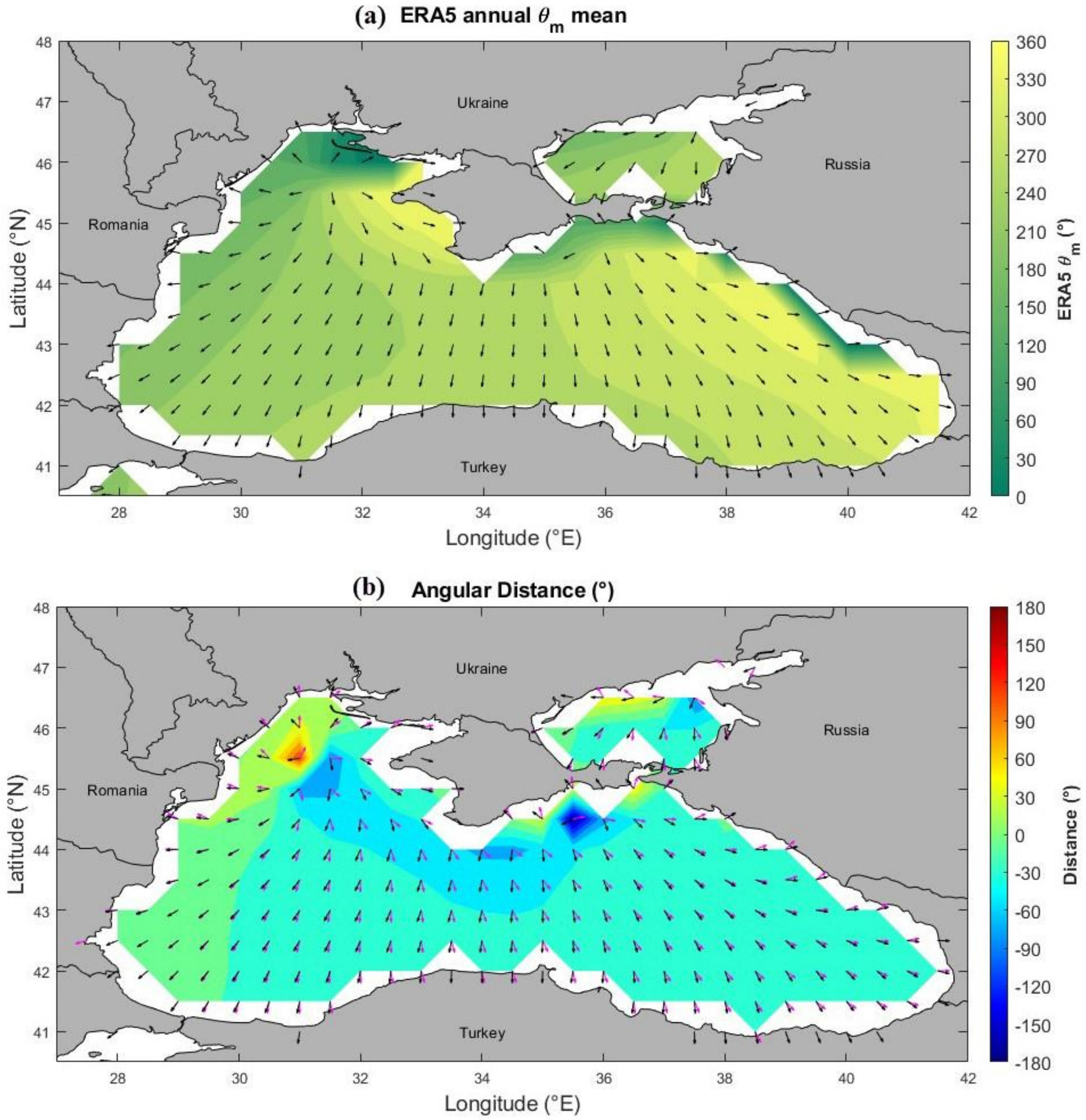

Figure 3.34. ERA5 annual mean θ_m and the shortest angular distances between the wave model and ERA5 for 1996-2005.

These increases observed in both annual and seasonal averages are primarily attributed to the projected rise in TWL. As future inundations incorporate existing land areas into submerged regions, these changes become a critical factor in wave projections, emphasizing a key finding of this study.

Figure 3.37 illustrates the annual H_{99} averages for PW20 and FW30, along with the ND between the two periods, presented on both annual and seasonal scales. The maximum annual H_{99} mean is approximately 3.5 m in PW20, increasing to 4 m in FW30. The annual H_{99} mean is projected to rise by 2–12%, with the most substantial seasonal increases occurring in summer and winter, reaching approximately 20%. Conversely, slight decreases of about -12% are observed in fall and spring. During summer, the increase in H_{99} is predominantly concentrated in the central and eastern Black Sea, whereas in winter, it is primarily evident in the central and western Black Sea. In autumn, significant decreases are observed along the eastern Black Sea nearshore, while in spring, similar reductions are evident in the eastern Black Sea nearshore and the Sea of Azov.

The anticipated rise in TWL also contributes to significant increases in H_{99} along the coasts of Romania, Ukraine, and Russia, as indicated by the dark red areas on the ND map. Additionally, regions predicted to be inundated due to the TWL increase and subsequently incorporated into the projected wave climate are more distinctly visible when comparing the annual H99 PW20 and FW30 figures (Figure 5.20) and capturing the expanded areas.

Figure 3.38 illustrates the annual and seasonal T_m and the ND between the PW20 and FW30 periods. The projected annual changes in T_m range between -2% and 2%, excluding areas projected to be inundated in the future. During MAM, no significant changes in T_m are anticipated, whereas in SON, a general decrease of up to -4% is expected. In JJA, a noticeable increase is observed, particularly in the Sea of Azov, where T_m is projected to rise by up to 8%. In DJF, an increase of up to 3% is expected in the western half of the Black Sea, while a decrease of up to -3% is projected along the nearshore areas of the eastern half.

Overall, no substantial changes in T_m are observed. However, Figure 3.38 highlights that areas along the shoreline exhibiting significant increases in both seasonal and annual analyses correspond to regions projected to be inundated in the future, as expected.

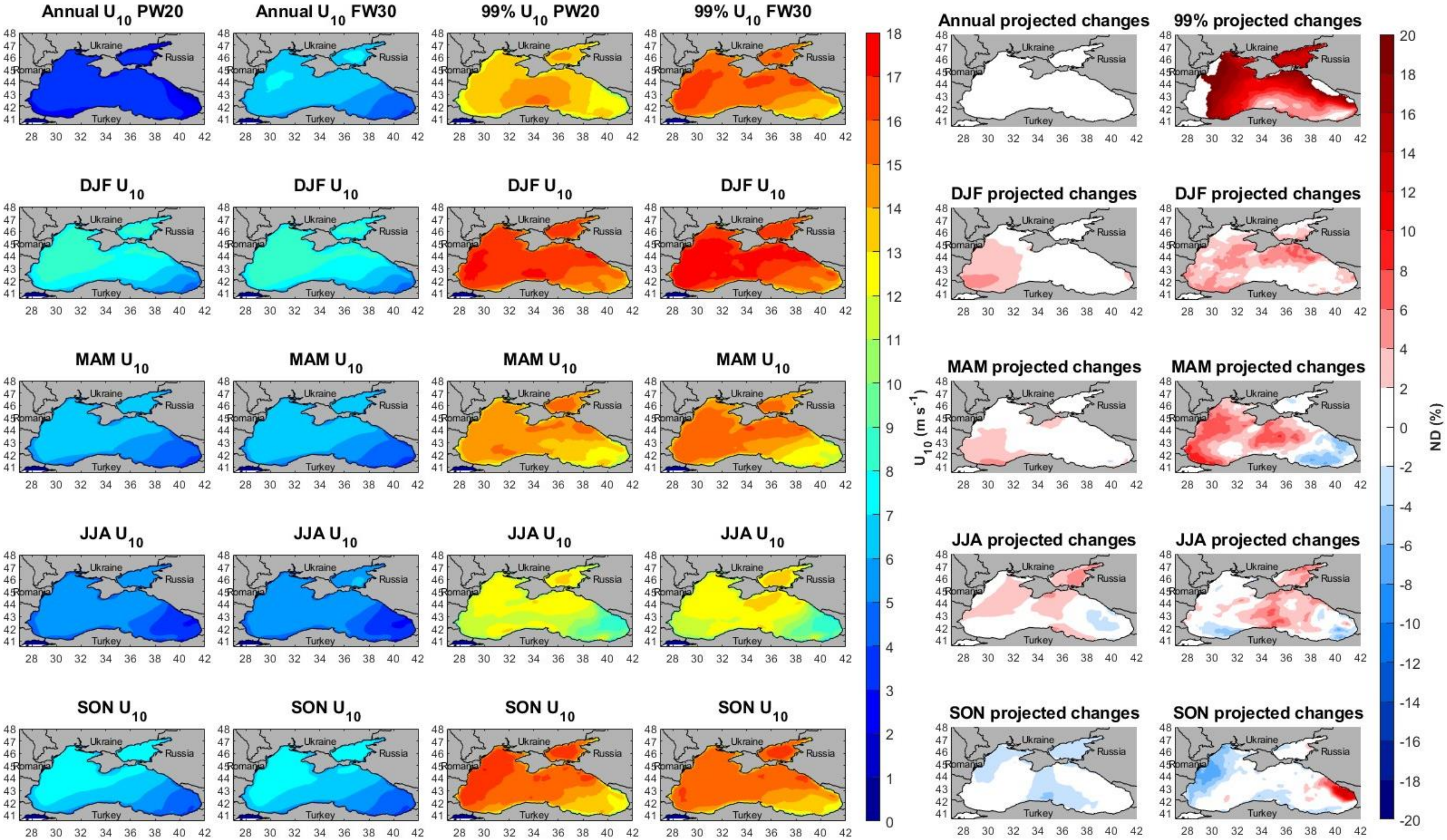

Figure 3.35. Annual mean and 99th percentile U_{10} in PW20 and FW30, and the changes between the two periods.

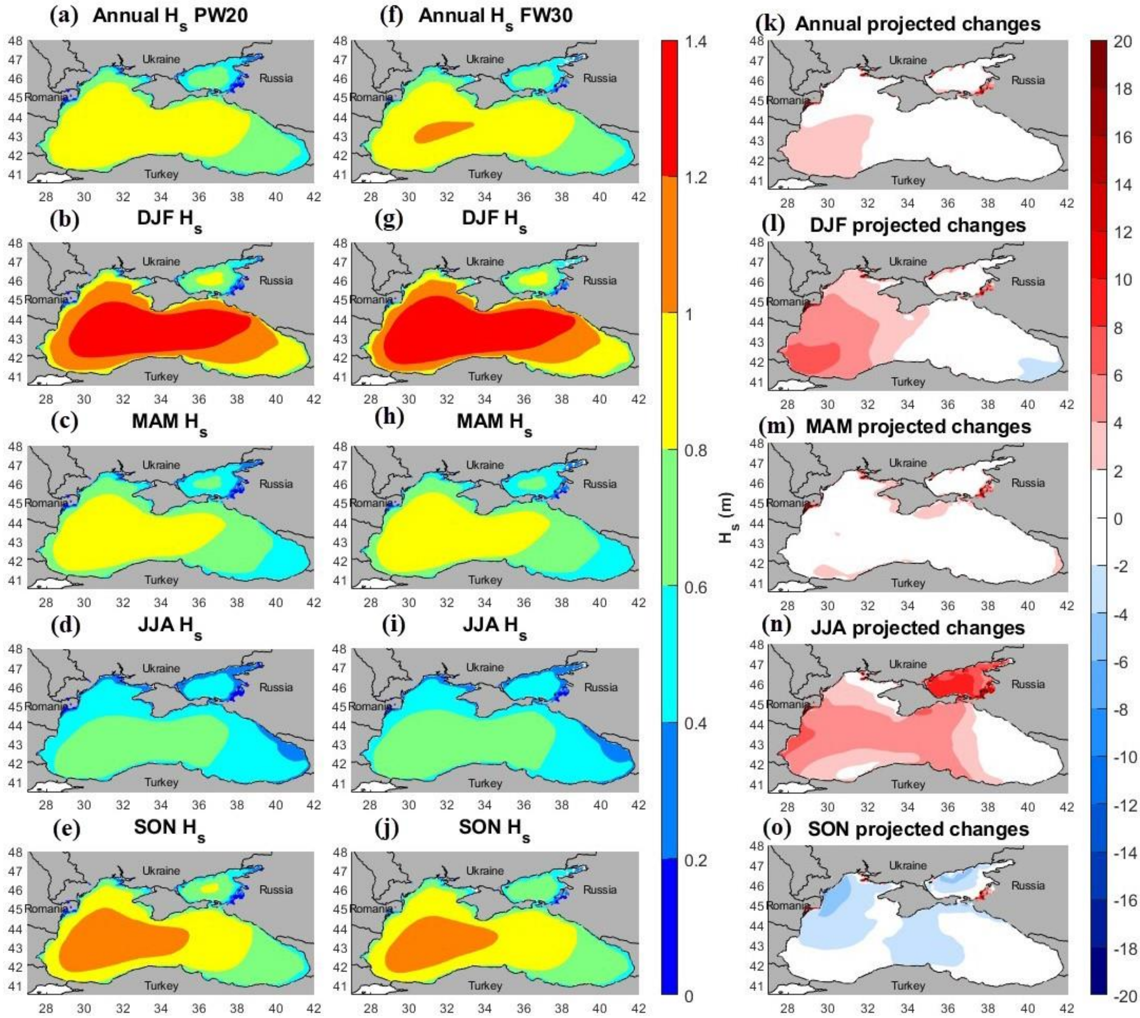

Figure 3.36. (a-e) Annual mean, winter, spring, summer, and autumn H_s in PW20, (f-j) annual mean, winter, spring, summer, and autumn H_s in FW30, and (k-o) annual mean, winter, spring, summer, and autumn ND of H_s between FW30 and PW20.

The annual and seasonal θ_m and the ND between PW20 and FW30 periods are shown in Figure 3.39. In this figure, positive changes are clockwise and negative changes are counterclockwise. When annual averages are examined, it is seen that the northern sector (north, northeast, northwest) wave directions are dominant throughout the Black Sea. Although the general direction is preserved between the past and future periods, direction deviations have occurred on a regional scale. In seasonal comparisons, it is noteworthy that more significant changes are experienced in wave directions, especially in winter and autumn. In winter, the θ_m in the Sea of Azov and the western Black Sea are regionally variable. The directions are more stable in spring and summer, but angular differences are observed in some local regions. In the autumn period, there are significant clockwise rotations in θ_m in the northwestern Black Sea.

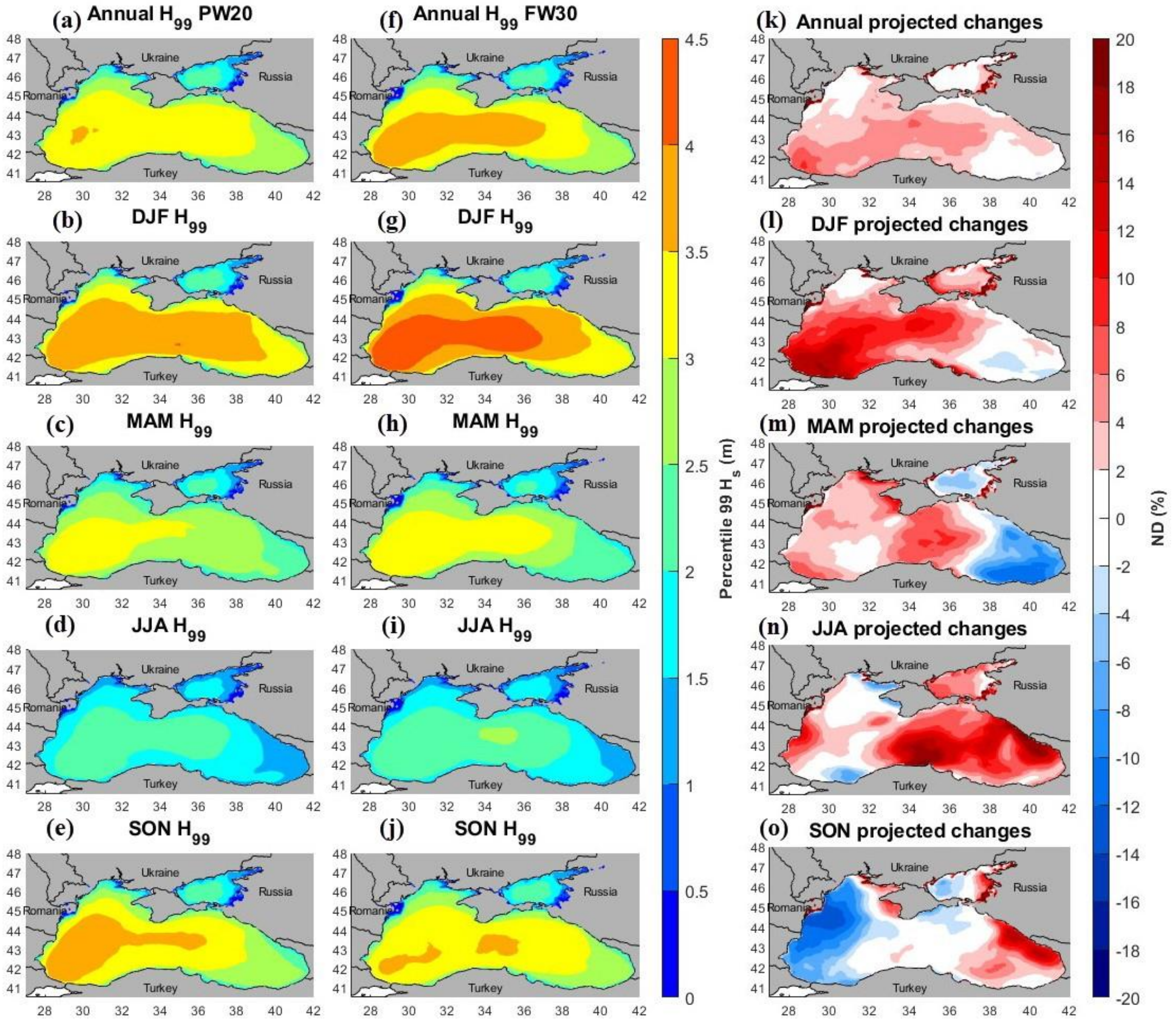

Figure 3.37. (a-e) Annual mean, winter, spring, summer, and autumn H_{99} in PW20, (f-j) annual mean, winter, spring, summer, and autumn H_{99} in FW30, and (k-o) annual mean, winter, spring, summer, and autumn ND of H_{99} between FW30 and PW20.

Wave direction is mainly influenced by the dominant wind patterns. If RCMs predict minimal changes in these dominant patterns, the resulting wave directions are likely to remain constant (Silva et al., 2020). Although climate change can affect wind speeds, it does not always lead to significant changes in wind direction, especially in regions where the large-scale atmospheric circulation remains unchanged. The general structure of large-scale atmospheric circulation patterns over the Black Sea is expected to be preserved in the future. However, changes in the seasonal intensity of these patterns, duration of activity, and frequency of the associated systems are anticipated. This may have significant effects on seasonal mean θ_m (Akpınar and Kömürcü, 2017).

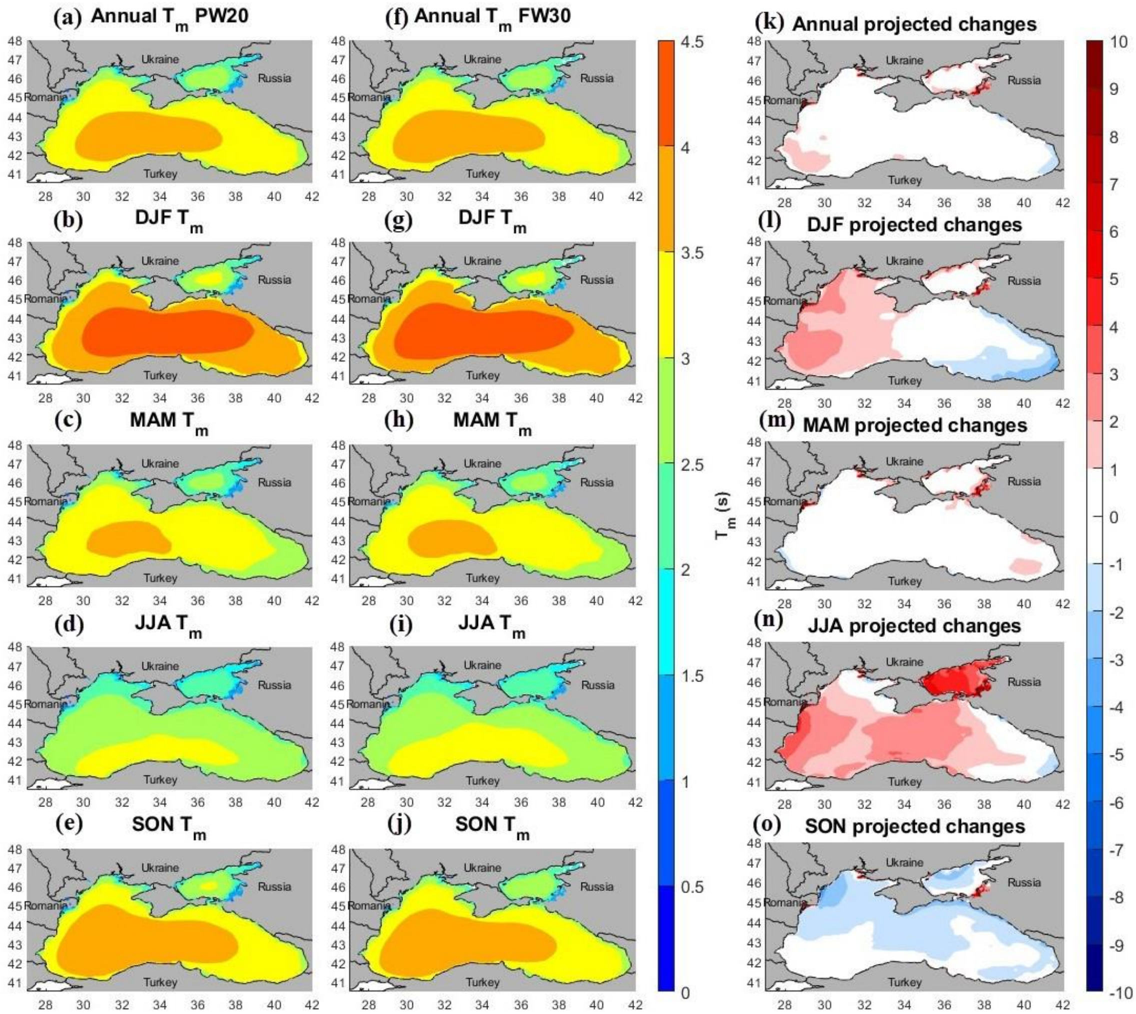

Figure 3.38. (a-e) Annual mean, winter, spring, summer, and autumn T_m in PW20, (f-j) annual mean, winter, spring, summer, and autumn T_m in FW30, and (k-o) annual mean, winter, spring, summer, and autumn ND of T_m between FW30 and PW20.

Figure 3.40 presents the trends of annual and seasonal mean H_s in the FW30 period calculated by the least squares regression method. The annual projected trend shows an increase of up to 0.15 cm/year in the northwestern nearshore area of the Black Sea. While it indicates a decreasing trend up to -0.3 cm/year in the southwestern Black Sea, this trend is between -0.05 and 0.05 cm/year in the remaining regions. In DJF, the mean H_s in the northwestern shores of the Black Sea and the Sea of Azov is expected to face a considerable increasing trend up to 0.4 cm/year. In the remaining regions, a decreasing trend up to -0.4

cm/year is observed. In MAM, an increasing trend of around 0.2 cm/year is anticipated in the Sea of Azov, while a mild increasing trend of around 0.15 cm/year is observed in the Black Sea. In JJA, a strong decreasing trend of -0.4 cm/year in the southwestern Black Sea and a slight increasing trend in the northern Black Sea shores are expected. In SON, while a general decreasing trend is dominant, an increasing trend of 0.2 cm/year is predicted only in the northwestern Black Sea coast. Since this analysis is made for the 30 years between 2071-2100, it can be concluded that in 2100, annual H_s means are expected to change between -9 cm and 4.5 cm compared to 2071, while for the seasonal H_s means, it is -12 cm and 12 cm.

Figure 3.41 presents the trends of annual and seasonal H_{99} mean in the FW30 period calculated by the least squares regression method. The annual projected H_{99} trend mostly shows a decreasing trend (up to -1 cm/year) except for a weak increasing trend (0.4 cm/year) in the western and northeastern regions of the Black Sea and the northern part of the Azov Sea. However, the seasonal projected H_{99} trends have stronger trends. In DJF, the increasing and decreasing trend locations are the same as the annual H_{99} trend, but greater in magnitude, with a decreasing trend of up to -2 cm/year and an increasing trend of up to 2 cm/year. In MAM, an increasing trend of 2 cm/year is anticipated in most of the study area, especially the western half of the Black Sea, except for the mid-eastern area of the Black Sea with a -0.6 cm/year trend. In JJA, trends of -0.4 cm/year and -0.6 cm/year in the southwestern and southeastern Black Sea regions and an increasing trend of up to 1 cm/year in the northern and central Black Sea and the Azov Sea are expected. In SON, a significant decreasing trend of up to -2 cm/year dominates the southwestern and southeastern Black Sea and the southern region of the Sea of Azov. However, in the central Black Sea, a trend of up to 1.6 cm/year is dominant. Since this analysis is made for the 30 years between 2071-2100, it can be concluded from Figure 3.41 that in 2100, annual H_{99} means are expected to change between -30 cm and 12 cm compared to 2071, while for the seasonal H_{99} means, it is -60 cm and 60 cm.

At the end of all analyses, it was observed that the range of variation of the mean values was much smaller than the extreme values. In addition, results analyzed on an annual basis predicted mild changes, while those analyzed on a seasonal basis predicted more dramatic changes, emphasizing the importance of the short-term assessment interval. Moreover, the consistency of the model is evident from the agreement between the changes in annual and seasonal U_{10} means in Figure 3.35 and the changes in H_s in Figure 3.36 and H_{99} in Figure 3.37.

3.3. Wave Runup and Coastal Flooding

3.3.1. Wave Runup Results

In this section, the spatial distribution of R_2, its temporal variation, and its relative contribution to the total water level are evaluated based on the SWAN model results in 2071-2100. The average conditions, 99th percentile, and RP100 are analyzed separately. In addition, the relationship between slope as discussed and R_2 and the R_2 trend in the FW30 period is examined.

The mean R_2 values show considerable spatial variability along the Black Sea and Sea of Azov coasts (Figure 3.42b). The data show that R_2 varies between 0.005 m and 2.96 m under average conditions, with a mean value of approximately 0.25 m. The highest mean R_2 values are observed along the western-central Black Sea coast of Türkiye, especially along the coastline between Zonguldak and Sinop. In this region, mean R_2 values are generally between 1.5–2.0 m, up to 2.9 m in some places. The bathymetry map in Figure 1.1c shows that although the continental shelf is not strictly narrow in this area, the slope is relatively high near the coast. In addition, the mean H_s is in the range of 0.9-1.1 m in this region (Figure 3.36), and the S06 formula reflects these conditions as high R_2. The slope data are also in the range of 0.06-0.09 in this region (Figure 3.42a), thus creating a cumulative effect originating from both waves and morphology.

In contrast, in the northeast of the Sea of Azov (e.g., Taganrog Bay), bathymetry is very shallow, average H_s is low (<0.4 m), and slope is mild; therefore, average R_2 values generally remain in the range of 0.05-0.2 m. Similarly, along the Bulgarian and Romanian coasts, the combination of a wide continental shelf, low slope, and moderate H_s (0.6-0.8 m) keeps average R_2 values limited.

Under the 99th percentile and RP100 scenarios representing extreme conditions, R_2 values increase even more. The maximum value is around 9 m for the 99th percentile R_2

(Figure 3.42d) and RP100 (Figure 3.42c). The highest and most widespread RP100 R_2 values are observed in the coastal area between Zonguldak and Sinop along the western-central Black Sea coast of Türkiye. As seen in Figure 3.42c, this coastline is represented by red tones under RP100 conditions, and R_2 values of 4-6 m are prominent over a wide area throughout the region, increasing the vulnerability of the region in terms of flood potential.

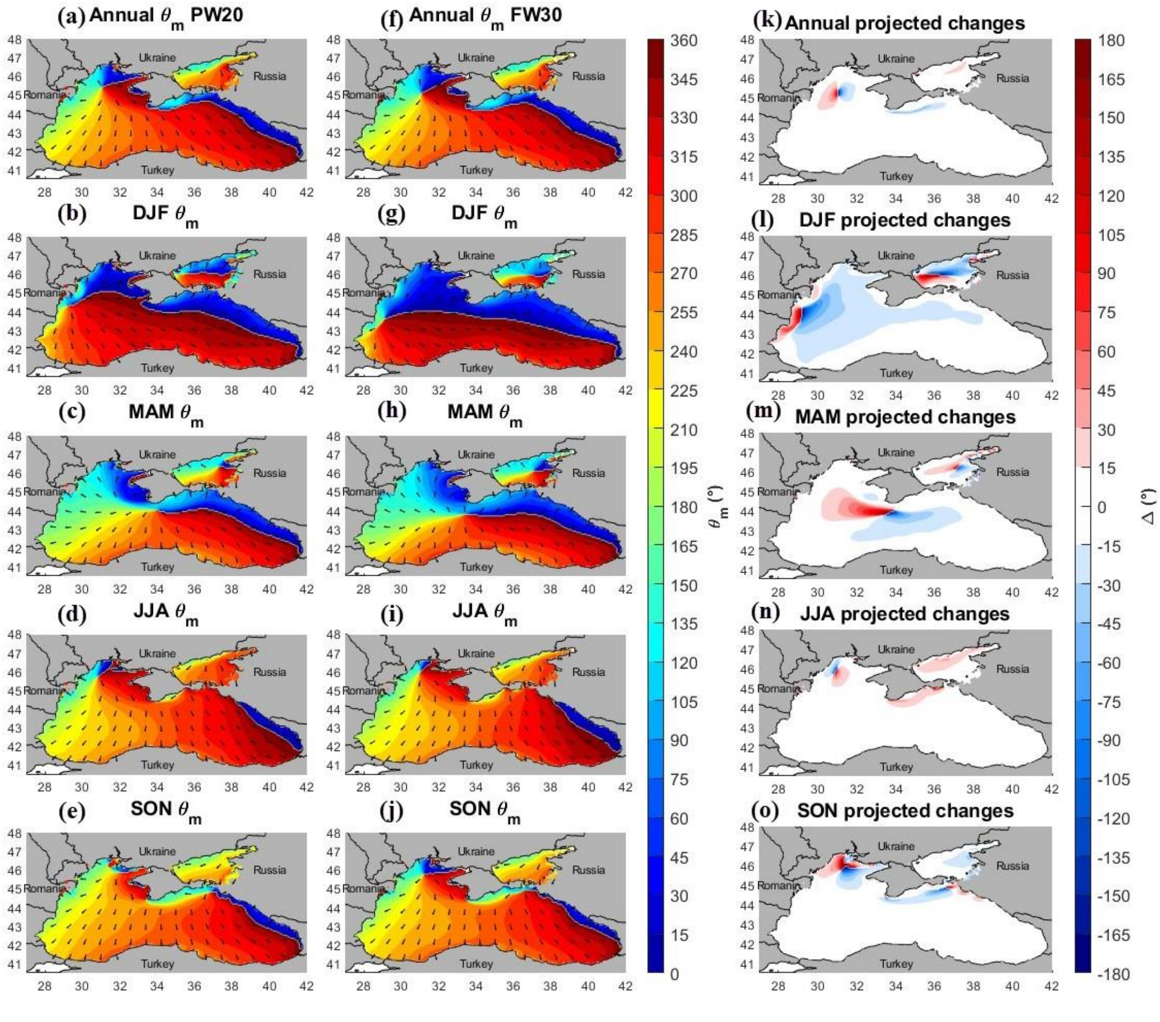

Figure 3.39. (a-e) Annual mean, winter, spring, summer, and autumn θ_m in PW20, (f-j) annual mean, winter, spring, summer, and autumn θ_m in FW30, and (k-o) annual mean, winter, spring, summer, and autumn ND of θ_m between FW30 and PW20.

In addition, R_2 values of 3-4 m have been observed locally on the Eastern Black Sea coast of Türkiye (especially between Rize and Hopa), in the southeast of the Crimean Peninsula, and some parts of the Black Sea coast of Russia (between Novorossiysk and Tuapse). In these areas, the continental shelf is narrow (Figure 1.1c), the slope is high (Figure

3.42c), and the H_{99} is relatively high, ranging between 2.5-3.5 m (Figure 3.37). The combination of these physical conditions causes the wave runup to reach its maximum in extreme storm conditions.

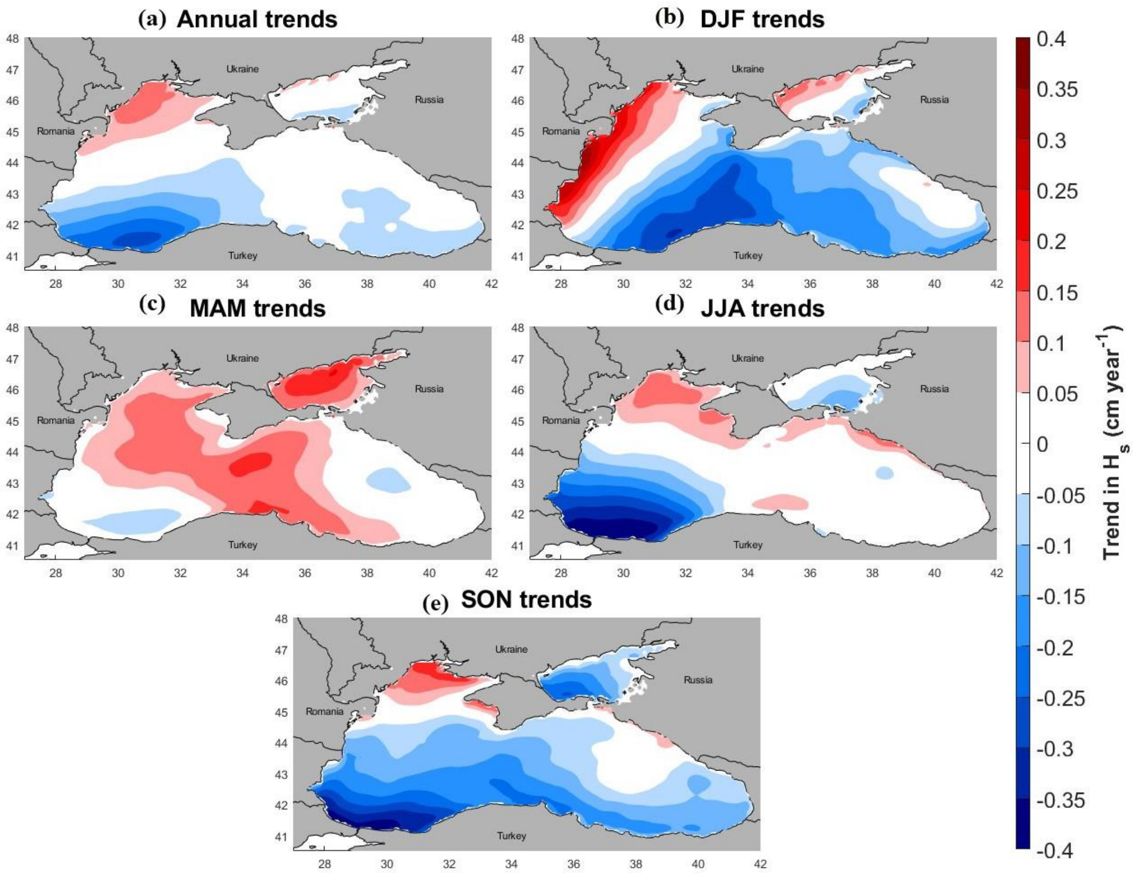

Figure 3.40. (a) Annual, (b) winter, (c) spring, (d) summer, and (d) autumn trends of the annual mean H_s in the FW30 period.

The temporal change of the runup component was analyzed with linear trends for the FW30 period. In this analysis, only statistically significant trends ($p < 0.05$) were taken into account (Figure 3.43). Slope values are expressed in millimeters/year. According to the results, R_2 values show a negative trend in a significant part of the Black Sea, with annual average decrease values concentrated between -0.5 and -2.0 mm/year. Significant decreases were detected, especially in the western-central Turkish coasts (e.g., between Zonguldak and Sinop) and in a large part of the eastern Turkish coasts (Trabzon, Rize surroundings). Although local positive trends are found in very limited regions, such as around Hopa, these increases are spatially narrow and weak in magnitude. Some parts of the southeastern Crimea and the northeastern Black Sea coast of Russia, particularly between Tuapse and Novorossiysk, exhibit statistically significant increasing trends in R_2. In these regions, the rate of increase is approximately 2 mm/year, which is one of the highest detected trends in the entire domain.

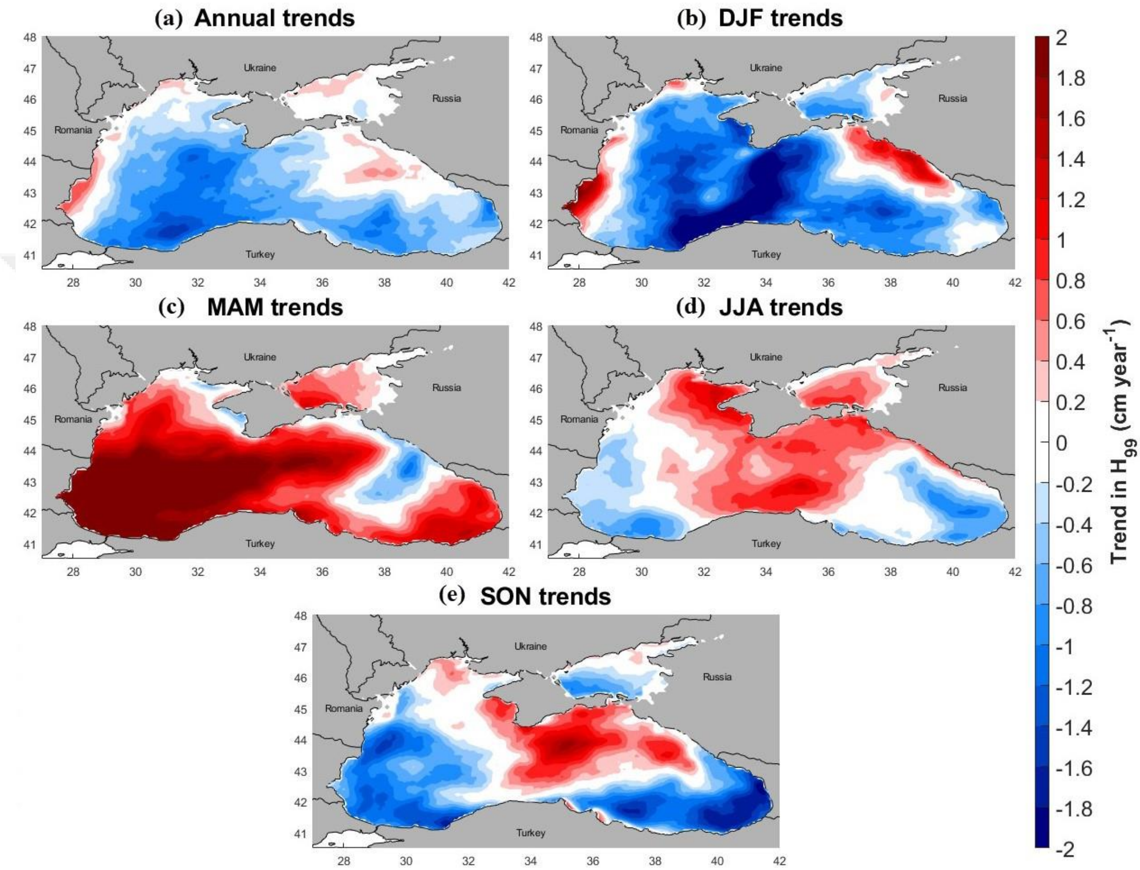

Figure 3.41. (a) Annual, (b) winter, (c) spring, (d) summer, and (d) autumn trends of the annual mean H_{99} in the FW30 period.

Statistical significance is the measurement of the probability that the slope coefficient is different from zero in the regression analysis. The p < 0.05 threshold used here indicates that the probability of the slope being random is less than 5%; therefore, slopes below this threshold are considered significant at the 95% confidence level. Therefore, only the points that meet this confidence threshold are shown and interpreted in Figure 3.43.

3.3.2. ESL Results

In this section, the contribution of the R_2 on the TWL is evaluated; the spatial distributions of TWL and ESL, their comparison in extreme conditions, and the ratio of R_2 are analyzed.

The average ESL and TWL values calculated along the Black Sea and the Sea of Azov are quite close to each other and exhibit similar spatial distributions in large areas. Since ESL is obtained by directly adding the R_2 component to TWL by a linear summation, there is no difference in the sea or open water; the difference is activated only along the coastline (Figure 3.44). Therefore, the amount of increase in ESL relative to TWL along the coast directly reflects the magnitude of R_2 at that point. In particular, along the entire southern Black Sea coast, the Bulgarian coast, the southern coast of the Crimean Peninsula, the Russian Black Sea coast, and the northern part of the Georgian coast, the average ESL values range from about 0.8 to 3.2 m. The R_2 component added to TWL in these coastal areas causes a significant increase in the TWL value; This situation reveals how important R_2 is in flood calculations.

The ratio of R_2 to TWL is also one of the critical outputs of the study. This ratio does not indicate how large a component R_2 is, or how much it contributes to TWL, but how much it increases TWL (Figure 3.45). This calculation was made based on the ratio of R_2 to TWL in percentage. According to the results, as it can also be concluded from Figure 3.44, along the entire southern Black Sea coast, the Bulgarian coast, the southern coast of the Crimean Peninsula, the Russian Black Sea coast, and the northern part of the Georgian coast, the R_2 contribution can reach 100% of TWL. In other words, not including R_2 in TWL calculations in these regions means leaving out half of the ESL. In contrast, on the coasts of the Sea of Azov, Romania, most of the Georgian coasts, and the Ukrainian Black Sea coasts, this ratio remains below 20% in most places. This shows that the relative effect of R_2 is low in these regions, which are the critical areas concerning the SS values (Figure 3.14).

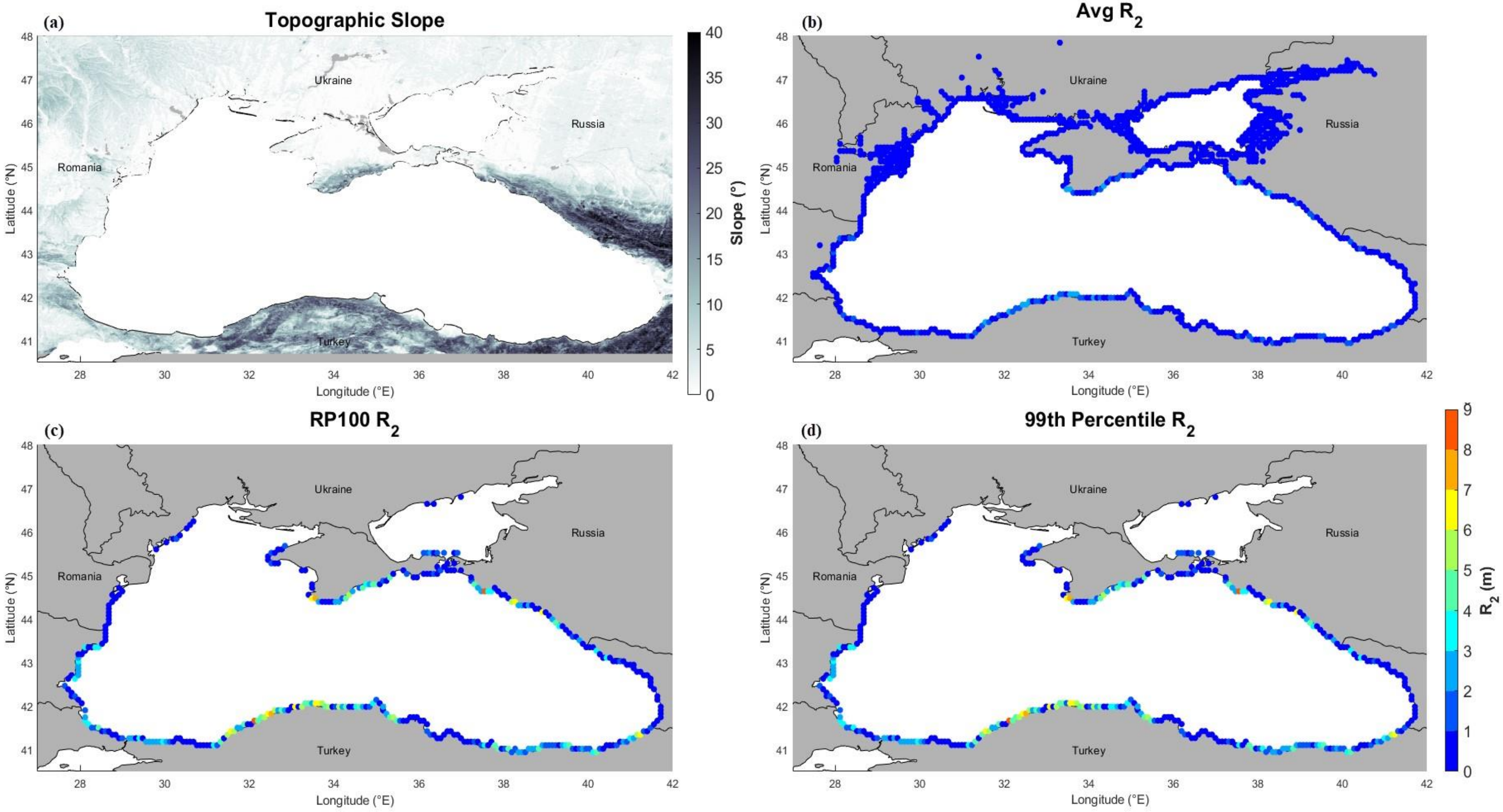

Figure 3.42. (a) Topographic slope, (b) the annual mean, (c) RP100, and (d) 99th percentile runup in FW30.

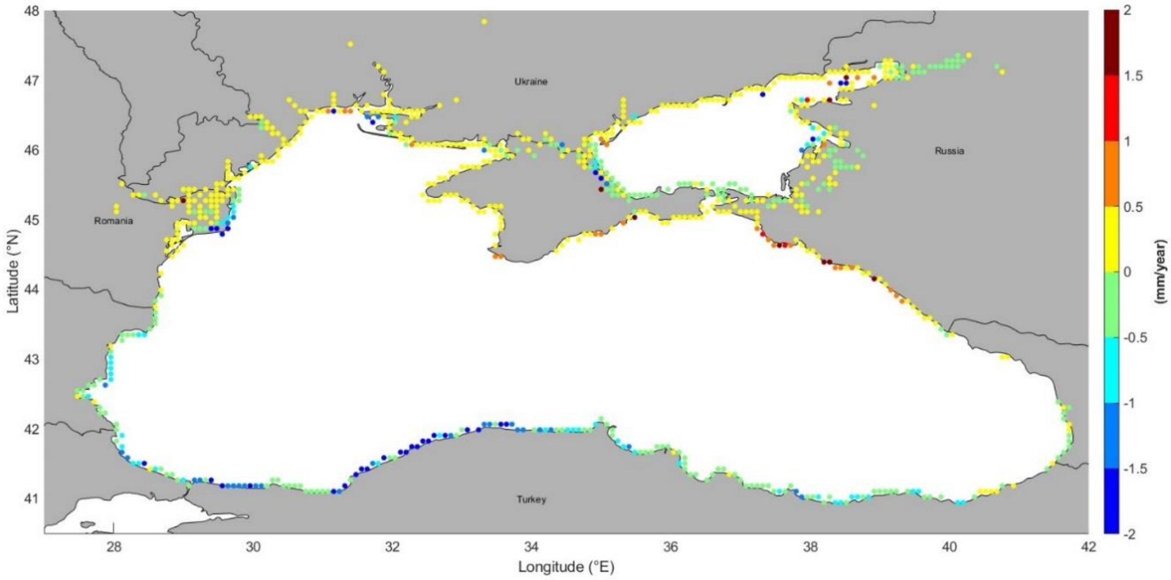

Figure 3.43. The statistically significant R_2 trends ($p < 0.05$) in the FW30 period.

In extreme conditions, the difference between ESL and TWL becomes more pronounced (Figure 3.46). The difference between ESL and TWL under RP100 conditions varies spatially along the coast. In some coastal areas, the R_2 contribution exceeds 5 m, significantly increasing ESL and directly affecting the flood level. Especially in places such as the Zonguldak–Sinop line, the eastern Turkish coast, and the southeast of Crimea, the R_2 contribution exceeds 5 m. Similarly, the 99th percentile scenario also revealed significant differences in these regions. These contributions reveal once again that R_2 becomes the main component determining the flood level in the microtidal Black Sea coast in the coastal areas where SS is relatively limited.

3.3.3. Coastal Flooding Results

In this section, the flood areas formed depending on the average and RP100 water levels are evaluated. Flood analyses were performed for both TWL and ESL, to which wave contribution is added. Only flood maps based on ESL are presented in the thesis, and the maps belonging to TWL are used only for comparison purposes. Thus, the effect of the wave runup component on the flood area can be isolated more clearly.

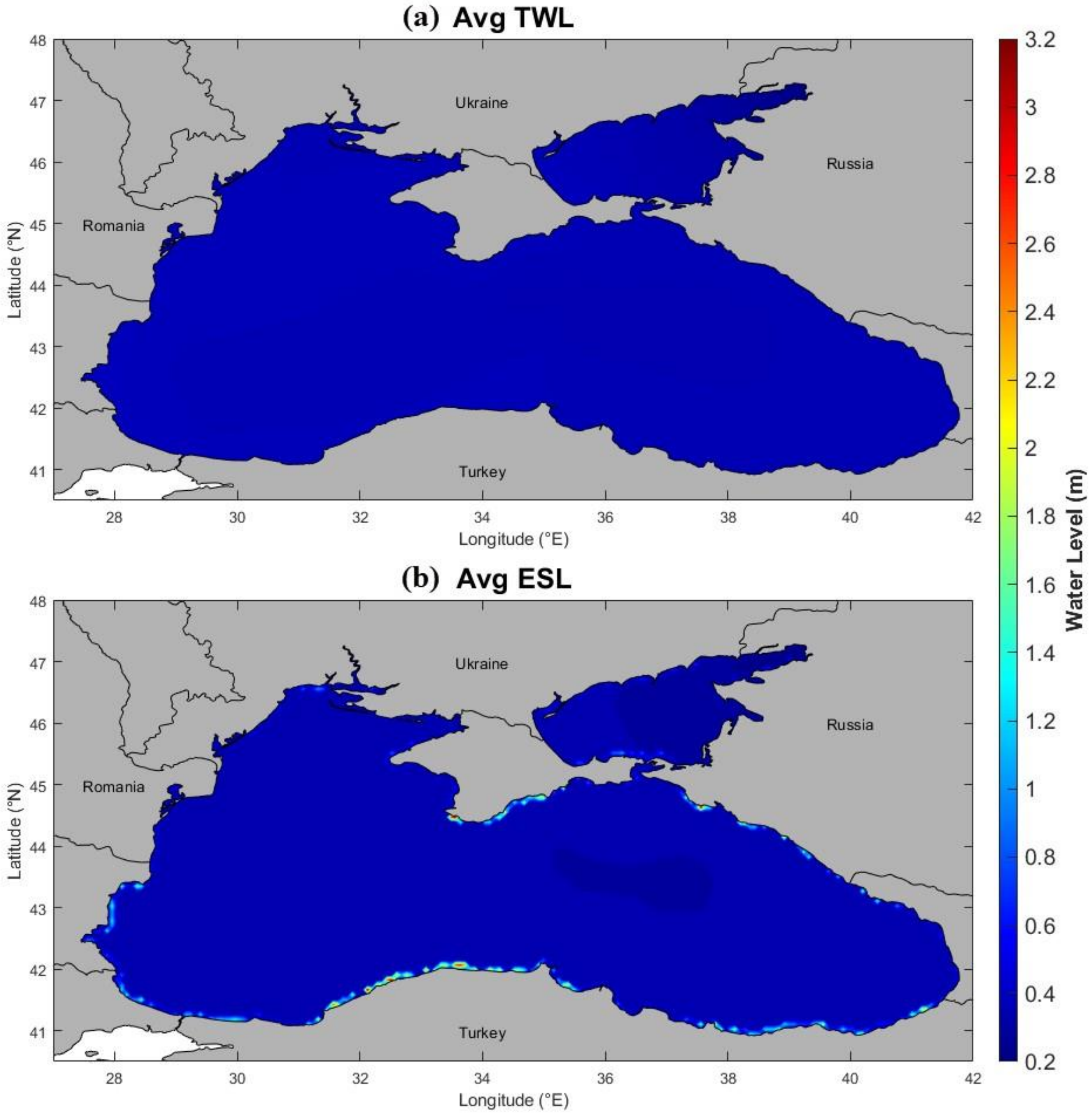

Figure 3.44. The average (a) TWL and (b) ESL.

Flood calculations are performed with the raster-based "bathtub" method, and the total water levels calculated with the digital surface height on the shore are compared on a pixel basis, and flood areas are extracted vectorially. In addition, only areas with a land slope greater than zero (slope > 0) are included in the flood analysis, preventing sea cells from being mistakenly determined as flood areas.

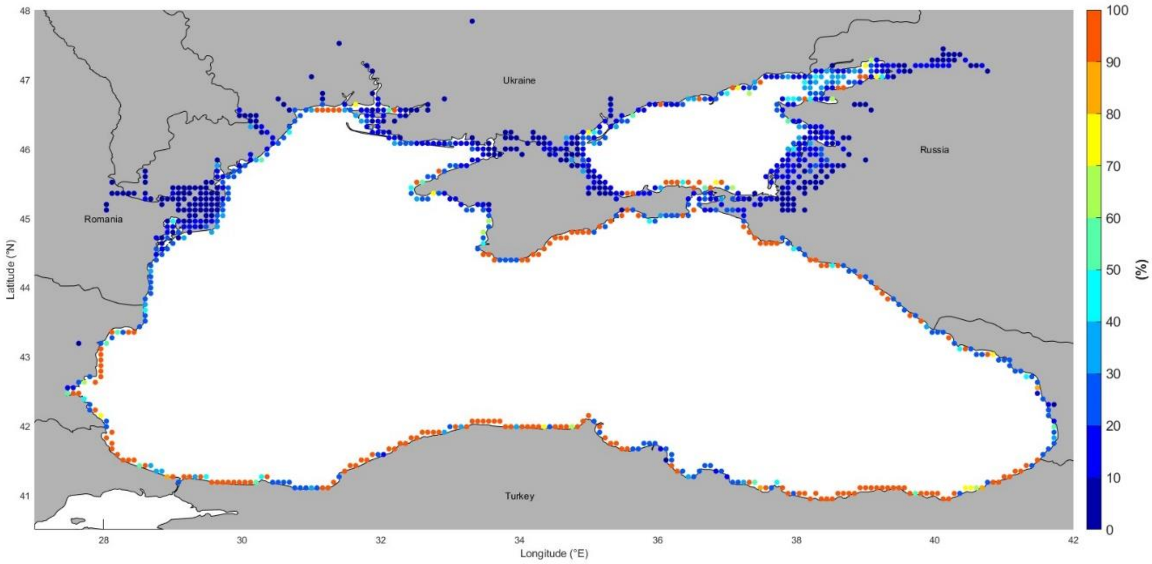

Figure 3.45. The ratio of R_2 to TWL in percentage.

While the flood area calculated according to the average TWL value is 6873.87 km², this area increases to 7514.30 km² when ESL is taken into account (Figure 3.47a). An increase of approximately 640 km² is observed numerically. However, this increase does not occur as a wide and homogeneous distribution, but rather as small-scale differences in various coastal areas. Visual comparisons show that the general flood patterns in the TWL and ESL maps are largely similar, but in some regions, the ESL spreads more towards the landward side. These differences are especially evident, albeit limited, in low-elevation deltas and low-sloping coastal areas. However, in some coastal areas, despite the high R_2 contribution, no flooding occurs even below the ESL. This situation has been observed especially in the southern Black Sea coast. In such regions, the high slope prevents the ESL from advancing into the land due to the steep coastal topography (Figure 3.42a). This finding clearly shows that not only the water level but also the coastal slope is decisive in the flood distribution. The average slope map (Figure 3.47a) used to support this interpretation provides important clues.

In the RP100 case, the flood area according to TWL is 12,548.36 km², while this value increases to 12,734.82 km² according to ESL (Figure 3.47b). This means an increase of approximately 1.5%. Although the numerical increase is limited, the effect of this increase is quite large, especially on low-lying deltas such as Romania and Ukraine. In such areas, even a small vertical water level increase can mean a large horizontal flood area.

In general, although the inclusion of ESL does not create a huge change in the total flood area, it creates significant differences in spatial patterns. This situation reveals that wave effects must also be taken into account in coastal flood analyses. However, one of the main reasons for the limited effect of ESL is that the coastal slope is quite high in many parts of the Black Sea coast. This steep topographic structure limits the spread of flooding towards the landward side, even if the sea level rises.

These results show that the inclusion of the runup component makes a significant contribution to flood hazard assessments; however, this effect varies according to coastal topography and regional characteristics. While the runup contribution can seriously affect the flood area, especially in low-slope coastal areas, this contribution is often limited in steep coastal areas. This finding reveals that not only the water level but also the coastal morphology must be taken into account in flood hazard analyses.

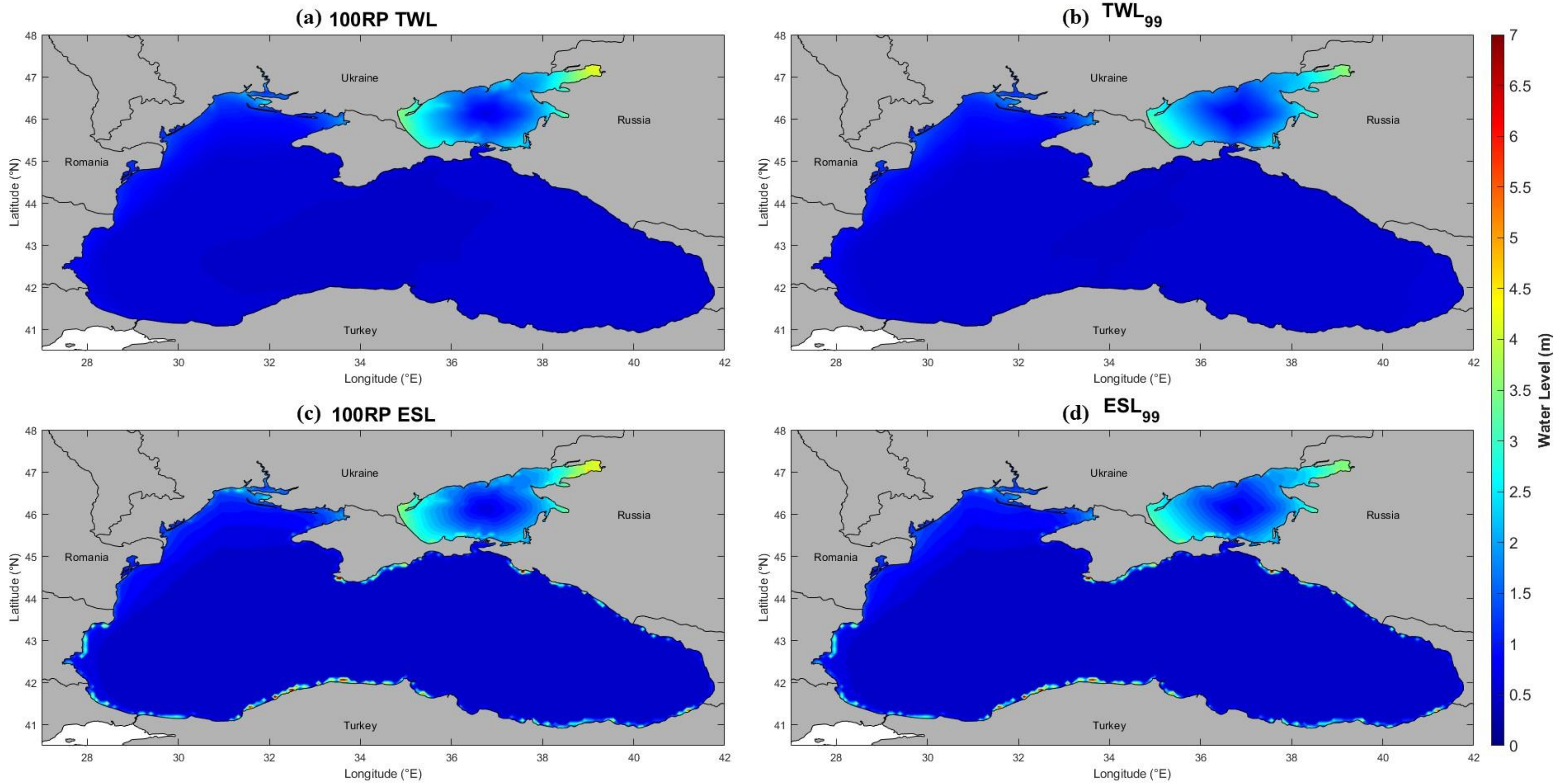

Figure 3.46. The maps of (a) 100RP TWL, (b) 99th percentile TWL, (c) RP100 ESL, and (d) 99th percentile ESL.

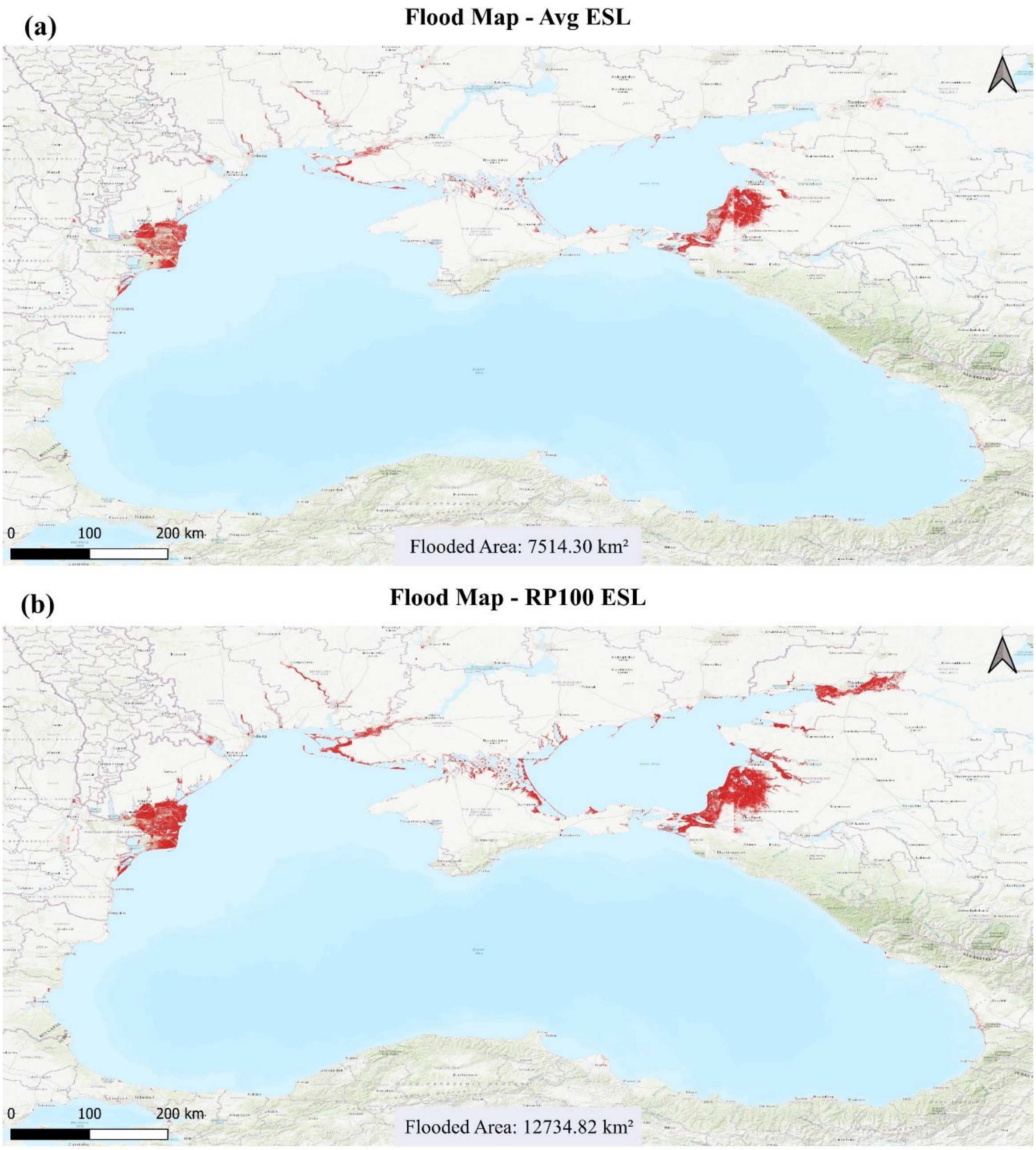

Figure 3.47. Coastal flood map with the (a) average and (b) RP100 ESL.

4. DISCUSSION

4.1. Interpretation of TWL and SS Trends

The first stage of this study statistically analyzes the future sea level behavior across a subregion that overlaps six CORDEX domains, focusing on the Black, Marmara, Aegean, and Mediterranean seas. Indicators such as Pearson's correlation coefficient, percentage change, linear least squares trends, PD, water level anomalies, and tidal characteristics were evaluated using EURO-CORDEX data, which is the only available source offering physical ocean variables for this region. Among the four basins, the Marmara Sea exhibits the lowest TWL, SS, and TE values, while the Black, Aegean, and Mediterranean seas are more prone to extreme SS and TWL (Figure 3.14 and Figure 3.15). Notably, RP100 SS reaches up to 590 mm higher than today's value along the coasts of the Azov Sea (Figure 3.18). The Black Sea also shows the highest increase rates for TWL, TE, and SS, with values reaching 29.3 mm/year (Table 3.2). In contrast, SS and TE appear to play more balanced roles in shaping future TWL in the Aegean and Mediterranean basins.

SS refers to a temporary rise in sea level caused by episodic storm events. It is governed by a combination of physical processes, including air pressure gradients, wind stress, Coriolis force, wave setup, and storm duration. SS changes can be assessed both spatially and temporally. From a spatial perspective, coastal zones with broad continental shelves and shallow bathymetry tend to experience enhanced SS compared to neighboring deeper areas (Park and Suh, 2012; Munroe and Curtis, 2017; Poulose et al., 2018; Irani et al., 2024). Temporally, SS variations reflect the differences in surge magnitude between historical and future time frames, largely driven by projected changes in MSL and wind dynamics under climate change.

The projected extreme SS values (RP100, RP10, and RP1) show spatial amplification along the southwestern Azov Sea coast. This pattern is explained by the joint influence of increasing MSL and intensified onshore winds, with the latter playing a dominant role (Rusu, 2019). Although rising MSL generally tends to suppress SS (Dean and Dalrymple, 2001;

Ragno et al., 2023), the concurrent increase in onshore wind speeds in this region overrides that effect, resulting in a net rise in SS levels.

Conversely, future projections indicate decreasing SS trends in shallow coastal zones to the north of the Black, Aegean, and Azov seas. The northern coastlines of the Azov Sea, the Ukrainian Black Sea coast, and the Thracian coast of Greece are expected to exhibit lower future RP10 and RP100 SS values (Figure 3.14). These reductions are attributed to a combination of projected hydrographic and atmospheric changes. Due to their existing shallow topography, these areas already experience elevated SS values, but future increases in MSL and offshore wind speeds, while wind directions remain seaward (Katopodis et al., 2021), are expected to mitigate SS further.

The findings underscore the strong spatial dependence of SS and TWL and the need to revisit future design water levels for coastal infrastructure. Vousdoukas et al. (2017) noted that changes in tidal dynamics have minimal influence in the eastern Mediterranean and Black Sea region, although MSL and MHHW are projected to increase uniformly due to global sea-level rise (Figure 3.12 and Figure 3.13).

Since no other dataset currently provides equivalent temporal and spatial resolution for this subregion, direct comparisons are limited. However, parallel results have been found in recent studies for other areas of the world. For instance, Wood et al. (2023) identified considerable increases in SS and TWL in the South China Sea, while Pein et al. (2023) reported increased TE and MSL values in the southern North Sea and the Elbe estuary.

It is important to emphasize that while the statistical analysis section focuses on SS dynamics, the role of wave contributions to TWL remains critical, especially in locations where the continental shelf is narrow. Wave setup and runup typically amplify in such areas, potentially intensifying the risk along coasts that otherwise appear less vulnerable to SS alone (Albert et al., 2016; Arns et al., 2017; Melet et al., 2018; Sahoo et al., 2021). The Mediterranean, Marmara, Black, and Aegean seas are particularly sensitive due to their narrow continental shelves. Therefore, the results presented in Section 3.1 represent a foundational step in assessing coastal hazard dynamics at a subregional scale, an aspect often overlooked in large-scale global and regional analyses.

4.2. Numerical Wave Modeling and Wave Runup in the Black Sea

In this section, the results of numerical wave modeling conducted in the Black Sea are evaluated. In the study, the SWAN model was run with high-resolution wind data with the RCP4.5 scenario for the period 2071-2100, and the shoreline, water level, and, as a result, the active nodes were updated at each time step to spatially project future changes in wave. In this context, H_s values obtained were analyzed at seasonal and annual scales; annual 99th percentile values were interpreted.

Annual mean H_{99} results reveal that extreme wave conditions are widespread over large areas, especially in the western parts of the Black Sea, the Romanian and Bulgarian coasts, as well as the Zonguldak-Sinop line of Türkiye. H_{99} values in these coasts reach 3.5-4.0 m in places (Figure 3.37). This situation can be associated with the strengthening of wave development due to the long fetch distances and increases in the wind speed (Figure 3.35), although they have wider continental shelves. In contrast, although locally high H_{99} values (3.0–3.5 m) are observed on the eastern Black Sea coast (e.g., around Hopa) and the Georgian coast, these values are spread over more limited areas. The southern coast of the Crimean Peninsula also shows locally remarkable H_{99} values. However, these regions do not produce risks as widespread as the western Black Sea.

Seasonal analysis of H_{99} revealed that wave dynamics vary regionally throughout the year. In spring (MAM) and winter (DJF), increasing H_{99} are prominent in the middle and western Black Sea, while in autumn (SON), decreasing trends are dominant in these areas. In summer (JJA), the increase is observed in the middle and eastern Black Sea (Figure 3.37). This change is associated with seasonal wind speed variations and coastal orientation. It is also noteworthy that the annual mean H_s values (Figure 3.36) do not show changes as prominent as the annual mean H_{99} values, which indicates the changes in the extreme conditions rather than the mean conditions.

The Zonguldak–Sinop coastline is among the regions with both high H_s values and significant R_2 contributions (Figure 3.42) in the model results. The medium-high range of coastal slopes here, combined with the narrowing shelf, increases the wave runup potential. This observation supports the narrow continental shelf–high wave contribution relationship proposed by Albert et al. (2016) and Arns et al. (2017). Furthermore, in the northern part of the Black Sea (Ukrainian coast), the H_s values are generally stable. The flatness of the coastal topography limits wave development here, which is consistent with the literature.

A major methodological advancement of this study is the dynamic update of the computational grid nodes in the wave model based on the time-varying shoreline positions and sea level changes. This study represents a novel implementation within the wave modeling literature, where active computational nodes in a spectral wave model (SWAN) are adjusted throughout the simulation period to reflect the spatiotemporal evolution of shoreline and water level. Previous climate change–driven wave projections for the Black Sea have relied on fixed bathymetry and static coastal boundaries (e.g., Rusu, 2020; Çakmak et al., 2023; Chirosca and Rusu, 2025), limiting their ability to capture dynamically shifting coastal conditions. The methodology proposed here enables a more realistic representation of nearshore wave processes, particularly in regions with low-lying terrain or substantial sea level rise, and provides enhanced reliability in projecting future coastal hazards.

Another methodological advancement is that while in many studies in the literature (e.g., Vousdoukas et al., 2017, Gomes da Silva et al., 2020; Kim et al., 2023; Stockdon et al., 2023), wave setup and runup contribution are modeled with constant slope or morphological assumptions, in this study, a more precise runup calculation was carried out with slope values depending on the coastline that change over time. This approach offers an “improved” framework compared to classical “first-order estimate” models.

As a result, when evaluated together with the wave dynamics in the Black Sea, continental shelf structure, changes in wind and water level, and coastal topography, it reveals the necessity of integrating multiple components affecting coastal floods. The detailed modeling and analysis applied in this study provide significant contributions to the creation of realistic coastal hazard maps for regional decision makers.

4.3. ESL and Coastal Flooding

ESL projections and associated flood mapping in this study reveal crucial insights into the compound nature of coastal hazards under climate change in the Black Sea. ESL was obtained by adding the predicted TWL and the R_2 component. Following that, ESL was further used to derive the flood extents based on the bathtub approach, where this level is compared with the DEM. For the Black Sea, the spatial patterns of the flood-prone areas along the coast, the effect of wave contribution on flood propagation, and the role of geomorphological constraints, such as slope/topography, are discussed.

When the flood areas based on average TWL and ESL are compared, ESL creates an additional flood area of approximately 640 km² under average conditions (Figure 3.47a). However, this increase is not regular and continuous along the coast. In particular, in flat areas such as low-lying deltas in Romania and Ukraine, a limited inflow is observed. In the RP100 scenario, this difference is smaller at 186.46 km², but although it increases at a lower rate (~1.5%), the flood impact in critical areas may be more widespread and intense (Figure 3.47b). This is because the topographic features of the coastline determine the advance of water more suddenly and effectively in extreme events.

A striking finding is that in some regions, despite the high R_2 values, no flood areas are observed. For example, on the Western Black Sea coast of Türkiye, between Zonguldak and Sinop, no floods are observed despite the high R_2. The main reason for this is the steepness of the coastal slope in these areas (Figure 3.42a). Despite the high ESL levels, the inward inflow of water remains limited. This shows how critical the coastal slope is in determining the flood extent.

The spatial distribution of ESL values also provides important findings. ESL values along the southern Black Sea coast, Bulgarian coast, southern Crimean Peninsula, Russian coast, and northern Georgia vary between 0.8–3.2 m and can be 1 m higher than TWL (Figure 3.44). In some coastal segments, such as the Zonguldak–Sinop line and southeastern Crimea, ESL exceeds 5 m under RP100 conditions (Figure 3.46).

Past flood events highlight the necessity of considering ESL in future coastal hazard assessments. For instance, the 2021 western Black Sea flood in Türkiye (Bartın, Kastamonu, Sinop) (Yılmaz, 2022) caused over 80 fatalities and widespread damage following coinciding wave activity and storm-induced sea level anomalies. Similarly, the 2012 flood in Russia’s Krasnodar region and the 2014 Tsarevo flood in Bulgaria led to significant casualties and losses. These events, often involving high waves and elevated water levels, demonstrate that even moderate MSL components can lead to severe impacts when combined with storm-driven extremes.

The continental shelf width also plays an important role in understanding the effects of different sea level components. While wave-induced runups are greater on narrow continental shelves (Albert et al., 2016; Arns et al., 2017), wide shelves increase the effect of SS (Park and Suh, 2012). This dual effect explains, for example, the dominance of storm surge on the northwestern coast of the Black Sea and wave impact on the southern and eastern coasts.

As a result, accurate estimation of regional flood hazard depends not only on sea level estimates but also on the integration of dynamic coastal morphology, slope, continental shelf structure, and wave contributions. The method used in this study goes beyond classical first-order estimate approaches and provides a more physically consistent flood hazard assessment by processing time-varying shoreline and slope information at high resolution.

4.4. Integrated Interpretation of ESL Components and Module Interactions

In the context of coastal hazards, the approach followed in this study aimed to bring together models and processes operating at different scales to assess ESL events in a more realistic and coastal-specific manner. This integrated structure is based not only on the output of a single physical process, but also on the combined consideration of components such as SS, TE, R_2, and spatiotemporal sea level variations. These modules, which are evaluated separately in the discussion sections, are processes that systematically affect each other and jointly shape the final ESL estimates.

First, in the study, TWL trends and SS trends were determined, and the main risk areas on the coast were identified. This analysis was not limited to the assessment of past trends alone, but also formed the basis for the creation of probability-based hazard maps for future project periods. However, this pure data-based analysis alone is insufficient to adequately explain coastal flood potential, because unless the coastal morphology is completed by processes such as wave setup and runup, the potential of water to reach the shore and move inland cannot be modeled. Therefore, in the second step, the wave characteristics were determined in both the open sea and near-shore regions using the SWAN model, which was structured specifically for the region.

The wave model results provided not only the open sea conditions but also the main inputs required for the runup calculations on the shore. At this point, one of the most innovative aspects of the study comes into play: The dynamic shoreline-based modeling. Unlike traditional applications, the SWAN model was run by redefining the shoreline according to the TWL data analyzed at each time step. In this way, the land-sea boundary advanced or retreated over time depending on the increases in the water level; the active calculation area (wet grid) of the model was constantly updated. Thus, instead of assuming only a fixed bathymetry and coastal geometry, the change of the shoreline over time was taken into account. This approach allowed for a more realistic representation of the transport of wave energy along the coast, especially in low-slope coastal areas susceptible to floods.

In addition, wave runup calculations were performed by integrating not only the wave parameters simulated for the projection period but also indirectly the time-dependent TWL data, and directly the coastal slope was updated depending on the shoreline at each time step. This bidirectional dynamic approach reveals the originality of the study in both wave modeling and coastal response calculation.

In the last stage, the outputs of all these components were brought together in a GIS environment, and flood areas at different locations along the coast were mapped. This comprehensive process provides not only a surface flood forecast but also a process-based hazard assessment by enriching the trends obtained from TWL and SS analyses with wave models and correlating them with coastal topography. Especially when the slope of the coast, wave energy, and current sea level are evaluated together, situations such as the absence of flooding in some regions despite high runup values (e.g., on high-sloping coasts) or the occurrence of flooding despite low TWL values (e.g., on wide plains) become more explainable.

As a result, this study presents the effects of future extreme sea level events on the coast more realistically by considering different physical components in an integrated and interactive structure rather than a modular one. Thanks to this structure, it is understood how processes such as TWL, runup, and SS, which are traditionally evaluated separately, work together, and the interpretability of the results increases.

4.5. Practical Implications for Coastal Hazard and Design

In coastal engineering applications, even when flood limits are not exceeded, the physical effects of ESL events, structural loads, and non-destructive flood effects play an important role. These effects are particularly related to dynamic processes such as wave runup and overtopping. They are also critical factors to be considered in the design of coastal structures.

Wave runup is the rise in water level created by waves reaching the shore, and this rise can create significant loads on structures. Especially on the shores with steep slopes, the runup height can reach several meters (e.g., Zonguldak-Sinop coast), which is a factor to be considered in the design of structures. Shankar and Jayaratne (2003) investigated the effects of wave runup and overtopping on coastal structures, highlighting the impact of these processes on the durability and stability of the structures.

Wave overtopping is the process of waves passing over coastal structures and passing behind them, which can lead to water accumulation and potential damage in the areas behind the structures. Van der Meer and Bruce (2014) stated that wave overtopping is an important parameter to be considered in the design of coastal structures.

ESL events, even if they do not directly cause flooding, can have various non-catastrophic effects in coastal areas. These effects include beach erosion, infrastructure damage, and ecosystem degradation. In particular, wave runup and overtopping are the main causes of such effects in coastal areas. Tebaldi et al. (2021) examined the effects that ESL events may have on coastal areas and emphasized the importance of these processes in terms of coastal management and planning.

In this context, various strategies are proposed to minimize the effects of ESL events and increase the resilience of structures in coastal engineering practices. These include comprehensive risk assessments, adaptive design approaches, and nature-based solutions (Hinkel and Nicholls, 2020). In particular, considering the effects of dynamic processes such as wave runup and overtopping in the design of coastal structures is important in terms of increasing the resilience of structures and minimizing potential damage.

As a result, the physical effects of ESL events on coastal structures, structural loads, and non-destructive flood effects are critical factors to be considered in coastal engineering practices. Understanding these processes and developing appropriate design strategies will contribute to the creation of sustainable and resilient infrastructures in coastal areas.

5. CONCLUSION

This thesis presents a holistic approach to assessing coastal flood hazards under future climate scenarios. TWL, wave dynamics, wave runup, and their effects on ESL projections and coastal flood analyses were evaluated together. The study spatially analyzed future coastal flood hazard with a dynamic analysis framework shaped by high-resolution wave modeling and temporal sea level changes, specific to the Black Sea. In particular, the "dynamic shoreline-based modeling" approach stands out as one of the most original contributions of the study; it ensures that both wave model and runup calculations are made on the shoreline updated according to the TWL at each time step. This method goes beyond classical fixed shore assumptions and increases physical consistency in coastal flood assessments. The main findings obtained in this context are as follows:

- The statistical analysis revealed that SS, TE, and TWL trends exhibited different patterns among the four regional seas. Significant SS increases were observed in the Black Sea, with maximum SS trends reaching 11.6 mm/year. TWL trends were especially prominent in the Black Sea (up to 15.5 mm/year) and the Eastern Mediterranean (up to 0.8 mm/year). In contrast, SS trends were weak in the Marmara Sea (maximum 2.2 mm/year) and even negative in the Aegean Sea (down to –3.5 mm/year).

- The Black Sea showed more distinct and statistically significant results in terms of storm surge trends compared to the Marmara, Aegean, and Eastern Mediterranean seas.

- Future wave modeling results revealed spatial differences in wave height approaching the shore; increasing trends were especially prominent in the central and western parts of the Black Sea, with projected increases up to 20% in the H_{99}.

- ESL values calculated by combining TWL and wave runup showed that high wave effects were possible even though no flooding occurred in some regions. For instance, along the Turkish coast between Zonguldak and Sinop, ESL values exceeded 5 m under RP100 conditions, yet flooding was not observed due to the steep coastal slope.

- It was observed that SS was more pronounced in regions with wide continental shelves and low slopes. For example, the southwestern Azov Sea, characterized by very shallow bathymetry and mild slopes, exhibits projected RP100 SS increases of up to 590 mm by the end of the century. This amplification results from the accumulation of surge energy in shallow waters where bottom friction limits inland flow. The western and northwestern coasts of the Black Sea share similar characteristics and are likewise sensitive to such surge dynamics.

- Wave runup height is higher on narrow, sloping coasts. In contrast, along the Romanian coast where the continental shelf is wide and slope is low, wave energy dissipates early, and average runup values remain between 0.6–0.8 m, even under moderate wave conditions. RP100 runup is also expected to remain relatively low compared to steep-slope regions.

- The rise in sea level not only expanded the flooded area but also changed how the coastal slope affected runup. As a result, runup reached farther inland, especially on low-slope coasts, where the impact became more widespread and dangerous.

- The spread of ESL values depends not only on SLR but also on wave contribution, coastal slope, and coastal morphology. ESL-based flood mapping showed up to 640 km^2 of additional inundation under average conditions compared to TWL-based estimates.

- Different dominant processes are striking among the countries bordering the Black Sea. While the SS effect is more prominent on the western and northern coasts (Romania, Ukraine, Russia), the wave runup effect is more prominent on the southern coasts (Türkiye, Georgia). In the Ukrainian and Russian coasts, the spatial distribution of these processes is heterogeneous due to the morphological structure and coastal slope.

- In the Turkish and Crimean coasts, the local contribution of wave runup to TWL can reach 100%. In other words, not including runup in TWL calculations in these regions means leaving out half of the ESL. In contrast, in Romania and Ukraine, the relative impact of runup remains mostly below 20%, with ESL dominated by SS.

- Flood propagation analyses conducted on the Black Sea coasts have revealed different hazard profiles on a country basis. In the Turkish coasts, despite the high ESL values due to the high slope, flood areas have remained limited. In the western Black Sea, flood potential has increased due to the lower slope and low coastal morphology. In the Bulgarian and Romanian coasts, the wide continental shelf and low topographic elevation have played a role in increasing flood areas. While regional differences are striking on the Ukrainian coast, flood propagation on the Russian Black Sea coast has been morphologically more limited. In the Georgian coast, flood areas have formed near the coast in areas where wave effects are high. These results show that flood hazard is directly dependent not only on the ESL level but also on the coastal topography and slope structure.

- The developed dynamic shoreline approach stands out as an innovative tool in terms of both wave energy transfer to land and spatial modeling of flood hazards.

While the proposed framework has demonstrated high applicability and innovation, certain limitations must be acknowledged. The use of a single emission scenario and regional model restricts the scope of the uncertainty analysis. The empirical runup formula (Stockdon et al., 2006), though widely adopted, may not fully capture the variability across different coastal morphologies. Additionally, the components of ESL were modeled sequentially rather than in a fully coupled hydrodynamic system, which may overlook some nonlinear interactions. The 100-year return levels estimated using GEV distributions are based on only 30 years of annual maxima, which may introduce uncertainty in the upper tail of the distribution, especially in areas with high interannual variability. Moreover, wave projections, runup calculations, ESL estimates, and flood extent mapping were conducted only for the end-century period (2071–2100), limiting the temporal scope of dynamic shoreline-based assessments. These factors, however, do not undermine the key findings but instead highlight areas for refinement in future research.

5.1. Recommendations for Future Work

The methodological framework developed in this thesis has provided remarkable progress, especially with the dynamic shoreline approach and component-based ESL modeling. However, some limitations and omissions create potential areas for future research. The following suggestions include future directions that can address these limitations and take the study further:

- In this study, flood areas were modeled only based on sea-oriented effects. In the future, developing models for compound flood events where river runoff, precipitation, and coastal effects are considered simultaneously may provide more accurate and holistic estimation of complex coastal hazards.

- Although dynamic shoreline was used, working with coupled morphodynamic models that directly account for time-varying coastal erosion or morphological transformations may further advance flood propagation estimations.

- Runup calculations were performed on commonly used parametric formulations (Stockdon et al., 2006) in this thesis. Classifying the coastal typology along the entire coast and selecting and applying the most appropriate empirical formula for each type (Gomes da Silva et al., 2020) will increase the accuracy of flood estimates. Comparison of these results with fully physically based hydrodynamic models, at least on a local-scale study, may be useful to test the reliability of the approach used.

- Comparison with fully physical models based on computational fluid dynamics (CFD) on a local-scale study allows for evaluating the performance of the model in coastal flooding in terms of accounting for drainage, flow direction, and terrain-specific effects.

- The impacts of coastal flooding are not limited to physical distribution areas. Integrated risk maps can be created for future social and economic damage estimates, considering infrastructure, settlement, and ecosystem sensitivities.

- In the present study, the nonlinear relationship between SS and TE was taken into account. However, the potential nonlinear interaction between SS and wave effects was not taken into account. It is important to investigate methods that can handle this interaction together and test them with appropriate models (e.g., coupled surge-wave models).

- Wave projections, runup calculations, ESL estimation, and flood mapping were conducted only for the end-century period (2071–2100). Future studies can expand the temporal coverage by including mid-century and/or near-future periods to investigate the progression of coastal hazards under different stages of climate change.

- In this thesis, only a single climate dataset was used for projection. Multi-scenario and multi-model comparisons can contribute to uncertainty analysis and provide more robust information to decision makers. Separate calibration for each wind input is the most critical step in this process.

- The number of regional sea level projection data with high spatial and temporal resolution should be increased with multi-scenario and multi-model comparisons. Increasing the availability of such data is especially necessary for improving uncertainty analyses, refining ESL estimates, and obtaining dynamic shoreline-based multi-model (ensemble) results.

- Validation of model outputs has been limited to past flood events. Using real coastal measurements (e.g., runup cameras, radar data, LiDAR) and field data in future studies can improve model performance.

- In regions with extensive flood spread or high runup values without overtopping, detailed local-scale feasibility studies should be conducted. Evaluating existing structures, infrastructure conditions, and coastal typology can inform region-specific mitigation strategies.

REFERENCES

Akpınar, A., B. Bingölbali, and G. P. Van Vledder, 2016, "Wind and Wave Characteristics in the Black Sea Based on the SWAN Wave Model Forced with the CFSR Winds", *Ocean Engineering*, Vol. 126, pp. 276–298.

Akpınar, A., G. P. Van Vledder, M. İ. Kömürcü, and M. Özger, 2012, "Evaluation of the Numerical Wave Model (SWAN) for Wave Simulation in the Black Sea", *Continental Shelf Research*, Vol. 50–51, pp. 80–99.

Albert, S., J. X. Leon, A. R. Grinham, J. A. Church, B. R. Gibbes, and C. D. Woodroffe, 2016, "Interactions Between Sea-Level Rise and Wave Exposure on Reef Island Dynamics in the Solomon Islands", *Environmental Research Letters*, Vol. 11, No. 5.

Almar, R., R. Ranasinghe, E. W. J. Bergsma, A. Dastgheib, J. A. Jiménez, and A. Melet, 2021, "A Global Analysis of Extreme Coastal Water Levels with Implications for Potential Coastal Overtopping", *Nature Communications*, Vol. 12, No.1.

Alpar, B., 2009, "Vulnerability of Turkish Coasts to Accelerated Sea-Level Rise", *Geomorphology*, Vol. 107, No. 1-2, pp. 58–63.

Amarouche, K., A. Akpınar, and R. E. Çakmak, 2020, "Assessment of Storm Events Along the Algiers Coast and Their Potential Impacts", *Ocean Engineering*, Vol. 210.

Amarouche, K., A. Akpınar, M. B. Soran, S. Myslenkov, A. G. Majidi, M. Kankal, and V. Arkhipkin, 2021, "Spatial Calibration of An Unstructured SWAN Model Forced with CFSR And ERA5 Winds for the Black and Azov Seas", *Applied Ocean Research*, Vol. 117.

Arns, A., S. Dangendorf, J. Jensen, S. Talke, J. Bender, and C. Pattiaratchi, 2017, "Sea-Level Rise Induced Amplification of Coastal Protection Design Heights", *Scientific Reports*, Vol. 7, No. 1.

Arns, A., T. Wahl, S. Dangendorf, and J. Jensen, 2015, “The Impact of Sea Level Rise on Storm Surge Water Levels in the Northern Part of the German Bight”, *Coastal Engineering*, Vol. 96, pp. 118–131.

Aucelli, P. P. C., G. Di Paola, A. Rizzo, and C. M. Rosskopf, 2018, “Present Day and Future Scenarios of Coastal Erosion and Flooding Processes Along the Italian Adriatic Coast: The Case of Molise Region”, *Environmental Earth Sciences*, Vol. 77, No. 10.

Aydoğan, B., T. Görmüş, B. Ayat, and T. Çarpar, 2021, “Analysis of Potential Changes in the Black Sea Wave Power for the 21st Century”, *Renewable Energy*, Vol. 169, pp. 512–526.

Ballesteros, C., J. A. Jiménez, and C. Viavattene, 2018, “A Multi-Component Flood Risk Assessment in the Maresme Coast (NW Mediterranean)”, *Natural Hazards*, Vol. 90, No. 1, pp. 265–292.

Başaran, B., and H. A. A. Güner, 2021, “Effect of Wave Climate Change on Longshore Sediment Transport in Southwestern Black Sea”, *Estuarine, Coastal and Shelf Science*, Vol. 258.

Battjes, J. A., and J. P. F. M. Janssen, 1978, “Energy Loss and Set-Up Due to Breaking of Random Waves”, *Proceedings of the 16th International Conference on Coastal Engineering*, American Society of Civil Engineers, Hamburg, Germany, pp. 569–587.

Bellotti, G., L. Franco, and C. Cecioni, 2020, “Regional Downscaling of Copernicus ERA5 Wave Data for Coastal Engineering Activities and Operational Coastal Services”, *Water*, Vol. 13, No. 6.

Bernatchez, P., and C. Fraser, 2012, “Evolution of Coastal Defence Structures and Consequences for Beach Width Trends, Québec, Canada”, *Journal of Coastal Research*, Vol. 28, No. 6, pp. 1550–1566.

Bingölbali, B., A. Akpınar, H. Jafali, and G. P. Van Vledder, 2019, “Downscaling of Wave Climate in the Western Black Sea”, *Ocean Engineering*, Vol. 172, pp. 31–45.

Booij, N., R. C. Ris, and L. H. Holthuijsen, 1999, “A Third-Generation Wave Model for Coastal Regions: 1. Model Description and Validation”, *Journal of Geophysical Research: Oceans*, Vol. 104, No. C4, pp. 7649–7666.

Boumis, G., H. R. Moftakhari, and H. Moradkhani, 2023, “Coevolution of Extreme Sea Levels and Sea-Level Rise under Global Warming”, *Earth’s Future*, Vol. 11, No. 12.

Brunnabend, S. E., H. A. Dijkstra, M. A. Kliphuis, H. E. Bal, F. Seinstra, B. van Werkhoven, J. Maassen, and M. van Meersbergen, 2017, “Changes in Extreme Regional Sea Level under Global Warming”, *Ocean Science*, Vol. 13, pp. 47–60.

Brunnabend, S. E., J. Schröter, R. Rietbroek, and J. Kusche, 2015, “Regional Sea Level Change in Response to Ice Mass Loss in Greenland, The West Antarctic And Alaska”, *Journal of Geophysical Research: Oceans*, Vol. 120, pp. 7316–7328.

Calafat, F. M., M. Marcos, and G. Jordà, 2022, “Trends in Storm Surge Extremes Match the Rate of Sea-Level Rise”, *Nature*, Vol. 603, pp. 104–109.

Carvalho, K. S., and S. Wang, 2019, “Characterizing the Indian Ocean Sea Level Changes and Potential Coastal Flooding Impacts under Global Warming”, *Journal of Hydrology*, Vol. 569, pp. 373–386.

Casas-Prat, M., and X. L. Wang, 2020, “Projections of Extreme Ocean Waves in The Arctic and Potential Implications for Coastal Inundation and Erosion”, *Journal of Geophysical Research: Oceans*, Vol. 125, No. 8.

Cavaleri, L., and M. Rizzoli., 1981, “Wind Wave Prediction in Shallow Water: Theory and Applications” *Journal of Geophysical Research: Oceans*, Vol. 86, No. C11, pp. 10961–10970.

Cavaleri, L., J. H. G. M. Alves, F. Ardhuin, A. Babanin, M. Banner, K. Belibassakis, M. Benoit, M. Donelan, J. Groeneweg, T. H. C. Herbers, P. Hwang, P. A. E. M. Janssen, T. Janssen, I. V. Lavrenov, R. Magne, J. Monbaliu, M. Onorato, V. Polnikov, D. Resio, W. E. Rogers, A. Sheremet, J. McKee Smith, H. L. Tolman, G. Van Vledder, J. Wolf, and I. Young, 2007, "Wave Modeling – The State of the Art", *Progress in Oceanography*, Vol. 75, No. 4, pp. 603–674.

Cavaleri, L., S. Abdalla, A. Benetazzo, L. Bertotti, J. R. Bidlot, S. Breivik, R. E. Carniel, J. Jensen, W. E. Portilla-Yandun, A. Rogers, A. Roland, J. M. Sanchez-Arcilla, J. Smith, Y. Staneva, G. P. Toledo, A. J. Van Vledder, and A. Van Der Westhuysen, 2018, "Wave Modelling in Coastal and Inner Seas", *Progress in Oceanography*, Vol. 167, pp. 164–233.

Ceyhunlu, A. I., G. Ceribasi, N. Ahmed, and H. Al-Najjar, 2021, "Climate Change Analysis by Using Sen's Innovative and Trend Analysis Methods for Western Black Sea Coastal Region of Turkey", *Journal of Coastal Conservation*, Vol. 25, No. 1, 11852–11865.

Chirosca, A. M., and Rusu, L., 2025, "Projections of Wind and Wave Climate on the Main Routes of the Mediterranean and Black Seas", *Journal of Ocean Engineering and Marine Energy*, Vol. 11, No. 1, pp. 149–167.

Chtioui, T., M. Benaabidate, M. H. Ouladsine, and M. Azzouz, 2024, "Assessing Coastal Flood Risk under Extreme Events and Sea Level Rise in the Casablanca–Mohammedia Coastline (Morocco)", *Natural Hazards*, Vol. 120, No. 12, pp. 10727–10752.

Copernicus Climate Change Service, 2019, "CORDEX Regional Climate Model Data on Single Levels", *Copernicus Climate Change Service (C3S) Climate Data Store (CDS)*, accessed on August 19, 2024.

Copernicus Climate Change Service, 2023, "ERA5 Hourly Data on Single Levels From 1940 To Present", *Copernicus Climate Change Service (C3S) Climate Data Store (CDS)*, accessed on August 22, 2024.

Cui, M., H. von Storch, and E. Zorita, 1995, "Coastal Sea Level and the Large-Scale Climate State: A Downscaling Exercise for the Japanese Islands", *Tellus A: Dynamic Meteorology and Oceanography*, Vol. 47, No. 1, pp. 132–144.

Çakmak, R. E., E. Çalışır, G. Lemos, A. Akpınar, A. Semedo, R. M. Cardoso, and P. M. Soares, 2022, "Evaluation of the Performance of a Dynamic Wave Climate Ensemble Simulated Using EURO-CORDEX Winds in the Black Sea and Sea of Azov", *International Journal of Climatology*, Vol. 42, No. 16, pp. 8345–8367.

Çakmak, R. E., E. Çalışır, G. Lemos, A. Akpınar, A. Semedo, R. M. Cardoso, and P. M. Soares, 2023, "Regional Wave Climate Projections Forced by EURO-CORDEX Winds for the Black Sea and Sea of Azov towards the End of the 21st Century", *International Journal of Climatology*, Vol. 43, No. 13, pp. 5927–5950.

Dean, R. G., and R. A. Dalrymple, 2001, *Coastal Processes with Engineering Applications*, Cambridge University Press, Cambridge, United Kingdom.

Didier, D., J. Baudry, P. Bernatchez, D. Dumont, M. Sadegh, E. Bismuth, M. Bandet, S. Dugas, and C. Sévigny, 2019a, "Multihazard Simulation for Coastal Flood Mapping: Bathtub Versus Numerical Modelling in an Open Estuary, Eastern Canada", *Journal of Flood Risk Management*, Vol. 12, No. S1.

Didier, D., M. Bandet, P. Bernatchez, and D. Dumont, 2019b, "Modelling Coastal Flood Propagation under Sea Level Rise: A Case Study in Maria, Eastern Canada", *Geosciences*, Vol. 9, No. 2.

Didier, D., P. Bernatchez, G. Boucher-Brossard, A. Lambert, C. Fraser, R. L. Barnett, and S. Van-Wierts, 2015, "Coastal Flood Assessment Based on Field Debris Measurements and Wave Runup Empirical Model", *Journal of Marine Science and Engineering*, Vol. 3, No. 3, pp. 560–590.

Dingemans, M. W., 1997, *Water Wave Propagation Over Uneven Bottoms*, World Scientific Publishing Company, London.

Dodet, G., A. Melet, F. Ardhuin, X. Bertin, D. Idier, and R. Almar, 2019, “The Contribution of Wind-Generated Waves to Coastal Sea-Level Changes”, *Surveys in Geophysics*, Vol. 40, pp. 1563–1601.

Eldeberky, Y., 1996, *Nonlinear Transformation of Wave Spectra in the Nearshore Zone*, Ph.D. thesis, Delft University of Technology, Department of Civil Engineering, The Netherlands.

ElKotby, M.R., T.A. Sarhan, M. El-Gamal, and A. Masria, 2024, “Evaluation of Coastal Risks to Sea Level Rise: Case Study of Nile Delta Coast”, *Regional Studies in Marine Science*, Vol. 78.

Erikson, L. H., A. Espejo, P. L. Barnard, K. A. Serafin, C. A. Hegermiller, A. O'Neill, P. Ruggiero, P. W. Limber, and F. J. Mendez, 2018, “Identification of Storm Events and Contiguous Coastal Sections for Deterministic Modeling of Extreme Coastal Flood Events in Response to Climate Change”, *Coastal Engineering*, Vol. 140, pp. 316–330.

Favaretto, C., L. Martinelli, and P. Ruol, 2019, “Coastal Flooding Hazard Due to Overflow Using a Level II Method: Application to the Venetian Littoral”, *Water*, Vol. 11.

Field, C. B., V. R. Barros, K. J. Mach, M. D. Mastrandrea, M. van Aalst, W. N. Adger, D. J. Arent, J. Barnett, R. Betts, T. E. Bilir, J. Birkmann, J. Carmin, D. D. Chadee, A. J. Challinor, M. Chatterjee, W. Cramer, D. J. Davidson, Y. O. Estrada, J.-P. Gattuso, Y. Hijioka, O. Hoegh-Guldberg, H. Q. Huang, G. E. Insarov, R. N. Jones, P. Romero-Lankao, J. N. Larsen, I. J. Losada, J. A. Marengo, R. F. McLean, L. O. Mearns, R. Mechler, J. F. Morton, I. Niang, T. Oki, J. M. Olwoch, M. Opondo, E. S. Poloczanska, H.-O. Pörtner, M. H. Redsteer, A. Reisinger, A. Revi, D. N. Schmidt, M. R. Shaw, W. Solecki, D. A. Stone, J. M. R. Stone, K. M. Strzepek, A. G. Suarez, P. Tschakert, R. Valentini, S. Vicuña, A. Villamizar, K. E. Vincent, R. Warren, L. L. White, T. J. Wilbanks, P. P. Wong, and G. W. Yohe, 2014, “Technical Summary”, in *Climate Change 2014: Impacts, Adaptation and Vulnerability. Part A: Global and Sectoral Aspects*, Cambridge University Press, Cambridge, United Kingdom and New York, NY, USA, pp. 35–94.

Formentin, S. M., 2021, “Key Performance Indicators for the Upgrade of Existing Coastal Defense Structures”, *Journal of Marine Science and Engineering*, Vol. 9, No. 9.

Foti, E., R. E. Musumeci, and M. Stagnitti, 2020, “Coastal Defence Techniques and Climate Change: A Review”, Rendiconti Lincei. Scienze Fisiche e Naturali, Vol. 31, pp. 123–138.

Galiatsatou, P., C. Makris, and P. Prinos, 2018, “Optimized Reliability Based Upgrading of Rubble Mound Breakwaters in a Changing Climate”, *Journal of Marine Science and Engineering*, Vol. 6, No. 3.

Galiatsatou, P., C. Makris, Y. Krestenitis, and P. Prinos, 2021, “Nonstationary Extreme Value Analysis of Nearshore Sea-State Parameters under the Effects of Climate Change: Application to The Greek Coastal Zone and Port Structures”, *Journal of Marine Science and Engineering*, Vol. 9, No. 8.

Gallien, T. W., N. Kalligeris, M. P. C. Delisle, B. X. Tang, J. T. D. Lucey, and M. A. Winters, 2018, “Coastal Flood Modeling Challenges in Defended Urban Backshores”, *Geosciences*, Vol. 8, No. 12.

Garland, B. B., 2010, “Rising Sea Level and Long-Term Sustainability of Near-Shore Islands of the United Arab Emirates: An Approach to Establishing Setback Lines for Abu Dhabi”, *WIT Transactions on Ecology and the Environment*, Vol. 130, pp. 135–146.

GEBCO Compilation Group, 2024, GEBCO 2024 Grid, https://www.gebco.net, accessed on July 4, 2024.

Giupponi, C., M. E. Borsuk, B. J. M. de Veries, and K. Hasselmann, 2013, “Innovative Approaches to Integrated Global Change Modelling”, *Environmental Modelling and Software*, Vol. 44, pp. 1-9.

Gomes da Silva, P., G. Coco, R. Garnier, and A. H. F. Klein, 2020, "On the Prediction of Runup, Setup and Swash on Beaches", *Earth-Science Reviews*, Vol. 204.

Gonzalez, N. M., R. Waldman, I. M. Parras-Berrocal, and S. Somot, 2025, "Decomposing Steric and Dynamic Sea Level Trends in a Future High-Emission Scenario of the Mediterranean Sea", *EGU General Assembly 2025*, Vienna, Austria, 27 Apr–2 May 2025, EGU25-16149.

Görmüş, T., B. Ayat, B. Aydoğan, and F. Tatui, 2021, "Basin Scale Spatiotemporal Analysis of Shoreline Change in the Black Sea", *Estuarine, Coastal and Shelf Science*, Vol. 252.

Günther, H., S. Hasselmann, and P. A. E. M. Janssen, 1992, "The WAM Model Cycle 4", Hamburg, Germany.

Hanna, S. R., D. W. Heinold, and A. P. I. Department, 1985, *Development and Application of a Simple Method for Evaluating Air Quality Models*, Washington, D.C.: American Petroleum Institute. API Publication No. 4409.

Hasselmann, K., 1997, "Climate-change Research after Kyoto", *Nature*, Vol. 390, pp. 225–226.

Hasselmann, K., 2009, "What to Do? Does Science Have a Role?", *European Physical Journal Special Topics*, Vol. 176, pp. 37–51.

Hasselmann, K., 2013, "Detecting and Responding to Climate Change", *Tellus B: Chemical and Physical Meteorology*, Vol. 65.

Hasselmann, K., and D. V. Kovalevsky, 2013, "Simulating Animal Spirits in Actor-Based Environmental Models", *Environmental Modelling and Software*, Vol. 44, pp. 10-24.

Hasselmann, K., T. P. Barnett, E. Bouws, H. Carlson, D. E. Cartwright, K. Enke, J. A. Ewing, H. Gienapp, D. E. Hasselmann, P. Kruseman, A. Meerburg, P. Müller, D. J. Olbers,

K. Richter, W. Sell, and H. Walden, 1973, "Measurements of Wind-Wave Growth and Swell Decay During the Joint North Sea Wave Project (JONSWAP)", *Deutsche Hydrographische Zeitschrift,* Vol. A8, No. 12, pp. 1–95.

Hasselmann, S., K. Hasselmann, J. H. Allender, and T. P. Barnett, 1985, "Computations and Parameterizations of the Linear Energy Transfer in a Gravity Wave Spectrum, Part II: Parameterizations of the Nonlinear Transfer for Application in Wave Models", *Journal of Physical Oceanography*, Vol. 15, No. 11, pp. 1378–1391.

Hatzikyriakou, A., and N. Lin, 2017, "Simulating Storm Surge Waves for Structural Vulnerability Estimation and Flood Hazard Mapping", *Natural Hazards*, Vol. 89, No. 2, pp. 939–962.

Hersbach, H., B. Bell, P. Berrisford, G. Biavati, A. Horányi, J. Muñoz Sabater, J. Nicolas, C. Peubey, R. Radu, I. Rozum, D. Schepers, A. Simmons, C. Soci, D. Dee, and J. N. Thépaut, 2023, "ERA5 Hourly Data on Single Levels From 1940 To Present", *Copernicus Climate Change Service Climate Data Store,* accessed on July 10, 2024.

Hersbach, H., B. Bell, P. Berrisford, S. Hirahara, A. Horányi, J. Muñoz-Sabater, J. Nicolas, C. Peubey, R. Radu, D. Schepers, A. Simmons, C. Soci, S. Abdalla, X. Abellan, G. Balsamo, P. Bechtold, G. Biavati, J. Bidlot, M. Bonavita, G. De Chiara, P. Dahlgren, D. Dee, M. Diamantakis, R. Dragani, J. Flemming, R. Forbes, M. Fuentes, A. Geer, L. Haimberger, S. Healy, R. J. Hogan, E. Hólm, M. Janisková, S. Keeley, P. Laloyaux, P. Lopez, C. Lupu, G. Radnoti, P. de Rosnay, I. Rozum, F. Vamborg, S. Villaume, and J. N. Thépaut, 2020, "The ERA5 Global Reanalysis", *Quarterly Journal of the Royal Meteorological Society,* Vol. 146, No. 730, pp. 1999–2049.

Hinkel, D.E., W. Wiersma, and S.G. Jurs, 2003, *Applied Statistics for the Behavioral Sciences*, 5th ed., Houghton Mifflin, Boston, MA.

Hinkel, J., and R. J. Nicholls, 2020, "Responding to sea level rise", *The Bridge: Linking Engineering and Society*, National Academy of Engineering, Washington, DC.

Holthuijsen, L. H., N. Booij, and R. C. Ris, 1993, "A Spectral Wave Model for the Coastal Zone", *Proceedings of the 2nd International Symposium on Ocean Wave Measurement and Analysis*, New Orleans, Louisiana, United States, pp. 630–641.

Idier, D., J. Rohmer, R. Pedreros, S. Le Roy, J. Lambert, J. Louisor, G. Le Cozannet, and E. Le Cornec, 2020, "Coastal Flood: A Composite Method for Past Events Characterization Providing Insights in Past, Present and Future Hazards—Joining Historical, Statistical and Modelling Approaches", *Natural Hazards*, Vol. 101, pp. 465–501.

IPCC, 2007, *Climate Change 2007: Synthesis Report. Contribution of Working Groups I, II and III to the Fourth Assessment Report of the Intergovernmental Panel on Climate Change*, IPCC, Geneva, Switzerland.

IPCC, 2013, *Climate Change 2013: The Physical Science Basis. Summary for Policymakers, Technical Summary and Frequently Asked Questions*, Working Group I Contribution to the Fifth Assessment Report of the Intergovernmental Panel on Climate Change, Cambridge University Press, Cambridge, UK and New York, NY, USA.

IPCC, 2014, *Climate Change 2014: Synthesis Report. Contribution of Working Groups I, II and III to the Fifth Assessment Report of the Intergovernmental Panel on Climate Change*, IPCC, Geneva, Switzerland.

IPCC, 2019, *IPCC Special Report on the Ocean and Cryosphere in a Changing Climate*, in: Pörtner, H.-O., Roberts, D.C., Masson-Delmotte, V., Zhai, P., Tignor, M., Poloczanska, E., Mintenbeck, K., Alegría, A., Nicolai, M., Okem, A., Petzold, J., Rama, B., Weyer, N.M. (Eds.), Cambridge University Press, Cambridge, UK and New York, NY, USA, p. 755.

IPCC, 2021, *Chapter 2: Changing State of the Climate System, in: Climate Change 2021: The Physical Science Basis. Contribution of Working Group I to the Sixth Assessment Report of the Intergovernmental Panel on Climate Change*, V. Masson-Delmotte, P. Zhai, A. Pirani, S.L. Connors, C. Péan, S. Berger, N. Caud, Y. Chen, L. Goldfarb, M.I.

Gomis, M. Huang, K. Leitzell, E. Lonnoy, J.B.R. Matthews, T.K. Maycock, T. Waterfield, O. Yelekçi, R. Yu, and B. Zhou (eds.), Cambridge University Press.

IPCC, 2022a, *Chapter 2: Terrestrial and Freshwater Ecosystems and Their Services, in: Climate Change 2022: Impacts, Adaptation and Vulnerability. Contribution of Working Group II to the Sixth Assessment Report of the Intergovernmental Panel on Climate Change*, H.-O. Pörtner, D.C. Roberts, M. Tignor, E.S. Poloczanska, K. Mintenbeck, A. Alegría, M. Craig, S. Langsdorf, S. Löschke, V. Möller, A. Okem, B. Rama (eds.), Cambridge University Press.

IPCC, 2022b, *Chapter 12: Cross-sectoral Perspectives, in: Climate Change 2022: Mitigation of Climate Change. Contribution of Working Group III to the Sixth Assessment Report of the Intergovernmental Panel on Climate Change*, P.R. Shukla, J. Skea, R. Slade, A. Al Khourdajie, R. van Diemen, D. McCollum, M. Pathak, S. Some, P. Vyas, R. Fradera, M. Belkacemi, A. Hasija, G. Lisboa, S. Luz, J. Malley (eds.), Cambridge University Press.

Irani, M., M.M. Naderi, A.R.M. Bavani, E. Hassanzadeh, and H. Moftakhari, 2024, "A Framework for Coastal Flood Hazard Assessment under Sea Level Rise: Application to the Persian Gulf", *Journal of Environmental Management*, Vol. 349.

Isaksen, L., M. Bonavita, R. Buizza, M. Fisher, J. Haseler, M. Leutbecher, and L. Raynaud, 2010, "Ensemble of Data Assimilations at ECMWF", *Technical Memorandum No. 636*, ECMWF, Reading, UK.

Janssen, P. A. E. M., 1989, "Wave-Induced Stress and the Drag of Air Flow Over Sea Waves", *Journal of Physical Oceanography*, Vol. 19, No. 5, pp. 745–754.

Janssen, P. A. E. M., 1991, "Quasi-Linear Theory of Wind-Wave Generation Applied to Wave Forecasting", *Journal of Physical Oceanography*, Vol. 21, No. 11, pp. 1631–1642.

Japan Aerospace Exploration Agency, 2015, “ALOS World 3D – 30 m (AW3D30) Global Digital Surface Model”, *Earth Observation Research Center (EORC)*, JAXA, https://www.eorc.jaxa.jp/ALOS/en/index_e.htm, accessed on January 5, 2025.

Jisan, M. A., S. Bao, and L. J. Pietrafesa, 2018, “Ensemble Projection of the Sea Level Rise Impact on Storm Surge and Inundation at the Coast of Bangladesh”, *Natural Hazards and Earth System Sciences*, Vol. 18, pp. 351–364.

Johansson, M. M., H. Pellikka, K. K. Kahma, and K. Ruosteenoja, 2014, “Global Sea Level Rise Scenarios Adapted to the Finnish Coast”, *Journal of Marine Systems*, Vol. 129, pp. 35–46.

Katopodis, T., I. Markantonis, D. Vlachogiannis, N. Politi, and A. Sfetsos, 2021, “Assessing Climate Change Impacts on Wind Characteristics in Greece Through High Resolution Regional Climate Modelling”, *Renewable Energy*, Vol. 179, pp. 427–444.

Kim, Y., R. A. Holman, H. F. Stockdon, and D. M. Thompson, 2023, “Observations of Beach Change and Runup, and the Performance of Empirical Runup Parameterizations During Large Storm Events”, *Coastal Engineering*, Vol. 180.

Kirezci, E., C. D. Young, R. Ranasinghe, L. J. Mentaschi, S. Vousdoukas, and A. D. Woodworth, 2020, “Projections of Global-Scale Extreme Sea Levels and Resulting Episodic Coastal Flooding over the 21st Century”, *Scientific Reports*, Vol. 10, Article 11629.

Komen, G. J., K. Hasselmann, and S. Hasselmann, 1984, “On the Existence of a Fully Developed Wind-Sea Spectrum”, *Journal of Physical Oceanography*, Vol. 14, No. 8, pp. 1271–1285.

Kotlarski, S., K. Keuler, O. B. Christensen, A. Colette, M. Déqué, A. Gobiet, K. Goergen, D. Jacob, D. Lüthi, E. van Meijgaard, G. Nikulin, C. Schär, C. Teichmann, R. Vautard, K. Warrach-Sagi, and V. Wulfmeyer, 2014, “Regional Climate Modeling on European

Scales: A Joint Standard Evaluation of the EURO-CORDEX RCM Ensemble", *Geoscientific Model Development*, Vol. 7, pp. 1297–1333.

Kovalevsky, D., I. Arto, K. Dhavala, T. Filatova, K. Hasselmann, S. Moghayer, L. Niamir, and A. Voinov, 2015, "Report on Integration of Climate Scenarios in the Modeling System".

Kutupoğlu, V., R. E. Çakmak, A. Akpınar, and G. P. Van Vledder, 2018, "Setup and Evaluation of a SWAN Wind Wave Model for the Sea of Marmara", *Ocean Engineering*, Vol. 165, pp. 450–464.

Laino, E., and G. Iglesias, 2024, "Multi-Hazard Assessment of Climate-Related Hazards for European Coastal Cities", *Journal of Environmental Management*, Vol. 357.

Lei, Z., W. Wu, Y. Gu, F. Zhai, and P. Li, 2023, "A General Method to Determine the Optimal Whitecapping Dissipation Coefficient in the SWAN Model", *Frontiers in Marine Science*, Vol. 10.

Lerma, A. N., T. Bulteau, S. Elineau, F. Paris, P. Durand, B. Anselme, and R. Pedreros, 2018, "High-Resolution Marine Flood Modelling Coupling Overflow and Overtopping Processes: Framing the Hazard Based on Historical and Statistical Approaches", *Natural Hazards and Earth System Sciences*, Vol. 18, No. 1, pp. 207–229.

Li, N., Y. Yamazaki, V. Roeber, K. F. Cheung, and G. Chock, 2018, "Probabilistic Mapping of Storm-Induced Coastal Inundation for Climate Change Adaptation", *Coastal Engineering*, Vol. 133, pp. 126–141.

Lincke, D., and J. Hinkel, 2021, "Coastal Migration Due to 21st Century Sea-Level Rise", *Earth's Future*, Vol. 9, No. 5.

Lincke, D., C. Wolff, J. Hinkel, A. Vafeidis, L. Blickensdörfer, and D. P. Skugor, 2020, "The Effectiveness of Setback Zones for Adapting to Sea-Level Rise in Croatia", *Regional Environmental Change,* Vol. 20, No. 2, p. 46.

Liu, J., B. Li, W. Chen, J. Li, and J. Yan, 2022, "Evaluation of ERA5 Wave Parameters with In Situ Data in the South China Sea", *Atmosphere,* Vol. 13, No. 6.

Maranzoni, A., M. D'Oria, and A. Rizzo, 2023, "Quantitative Flood Hazard Assessment Methods: A Review", *Journal of Flood Risk Management*, Vol. 16, No. 1.

Martzikos, N.T., P.E. Prinos, C.D. Memos, and V.K. Tsoukala, 2021, "Key Research Issues of Coastal Storm Analysis", *Ocean and Coastal Management*, Vol. 199.

Melet, A., B. Meyssignac, R. Almar, and G. Le Cozannet, 2018, "Under-Estimated Wave Contribution to Coastal Sea-Level Rise", *Nature Climate Change,* Vol. 8, No. 3, pp. 234–239.

Melet, A., R. Almar, and B. Meyssignac, 2020, "Contribution of Wave Setup to Projected Coastal Sea Level Changes", *Journal of Geophysical Research: Oceans,* Vol. 125, No. 2.

Mentaschi, L., G. Besio, F. Cassola, and A. Mazzino, 2013, "Problems in RMSE-Based Wave Model Validations", *Ocean Modelling*, Vol. 72, pp. 53–58.

Mentaschi, L., G. Besio, F. Cassola, and A. Mazzino, 2015, "Performance Evaluation of Wavewatch III in the Mediterranean Sea", *Ocean Modelling,* Vol. 90, pp. 82–94.

Mentaschi, L., M. I. Vousdoukas, J. Hinkel, P. J. Ward, and L. Feyen, 2020, "Economic Motivation for Raising Coastal Flood Defenses in Europe", *Nature Communications*, Vol. 11.

Morim, J., M. A. Hemer, X. L. Wang, N. Cartwright, C. Trenham, and A. Semedo, 2019, “Robustness and Uncertainties in Global Multivariate Wind-Wave Climate Projections”, *Nature Climate Change*, Vol. 9, No. 9, pp. 711–718.

Moss, R. H., J. A. Edmonds, K. A. Hibbard, M. R. Manning, S. K. Rose, D. P. Van Vuuren, T. R. Carter, S. Emori, M. Kainuma, T. Kram, G. A. Meehl, J. F. Mitchell, N. Nakicenovic, K. Riahi, S. J. Smith, R. J. Stouffer, A. M. Thomson, J. P. Weyant, and T. J. Wilbanks, 2010, “The Next Generation of Scenarios for Climate Change Research and Assessment”, *Nature*, Vol. 463, No. 7282, pp. 747–756.

Muis, S., B. Güneralp, B. Jongman, J. C. J. H. Aerts, and P. J. Ward, 2015, “Flood Risk and Adaptation Strategies Under Climate Change and Urban Expansion: A Probabilistic Analysis Using Global Data”, *Science of The Total Environment*, Vol. 538, pp. 445–457.

Muis, S., M. I. Apecechea, J. Dullaart, J. de Lima Rego, K. S. Madsen, J. Su, K. Yan, and M. Verlaan, 2020, “A High-Resolution Global Dataset of Extreme Sea Levels, Tides and Storm Surges, Including Future Projections”, *Frontiers in Marine Science*, Vol. 7.

Muis, S., M. Verlaan, H. C. Winsemius, J. C. J. H. Aerts, and P. J. Ward, 2016, “A Global Reanalysis of Storm Surges and Extreme Sea Levels”, *Nature Communications*, Vol. 7.

Munroe, R., and S. Curtis, 2017, “Storm Surge Evolution and Its Relationship to Climate Oscillations at Duck, NC”, *Theoretical and Applied Climatology*, Vol. 129, No. 1-2, pp. 185–200.

Nicholls, R. J., S. E. Hanson, J. A. Lowe, A. B. A. Slangen, T. Wahl, J. Hinkel, and A. J. Long, 2021, “Integrating New Sea-Level Scenarios into Coastal Risk and Adaptation Assessments: An Ongoing Process”, *WIREs Climate Change*, Vol. 12, No. 3.

Olbert, A. I., T. Dabrowski, S. Nash, and M. Hartnett, 2012, "Regional Modelling of the 21st Century Climate Changes in the Irish Sea", *Continental Shelf Research*, Vol. 41, pp. 48–60.

Onea, F., and E. Rusu, 2014, "Wind Energy Assessments along the Black Sea Basin", *Meteorological Applications*, Vol. 21, No. 2, pp. 316–329.

Oppenheimer, M., B. C. Glavovic, J. Hinkel, R. van de Wal, A. K. Magnan, A. Abd-Elgawad, R. Cai, M. Cifuentes-Jara, R. M. DeConto, T. Ghosh, J. Hay, F. Isla, B. Marzeion, B. Meyssignac, and Z. Sebesvari, 2019, "Sea Level Rise and Implications for Low-Lying Islands, Coasts, and Communities", *IPCC Special Report on the Ocean and Cryosphere in a Changing Climate*, [Pörtner, H.-O., D. C. Roberts, V. Masson-Delmotte, P. Zhai, M. Tignor, E. Poloczanska, K. Mintenbeck, A. Alegría, M. Nicolai, A. Okem, J. Petzold, B. Rama, N. M. Weyer (eds.)], Chapter 4, pp. 321–445.

Pallares, E., A. Sánchez-Arcilla, and M. Espino, 2014, "Wave Energy Balance in Wave Models (SWAN) for Semi-Enclosed Domains—Application to the Catalan Coast", *Continental Shelf Research*, Vol. 87, pp. 41–53.

Park, Y. H., and K. D. Suh, 2012, "Variations of Storm Surge Caused by Shallow Water Depths and Extreme Tidal Ranges", *Ocean Engineering*, Vol. 55, pp. 44–51.

Pein, J., J. Staneva, B. Mayer, M.D. Palmer, and C. Schrum, 2023, "A Framework for Estuarine Future Sea-Level Scenarios: Response of the Industrialised Elbe Estuary to Projected Mean Sea Level Rise and Internal Variability", *Frontiers in Marine Science*, Vol. 10.

Pickering, M.D., Wells, N.C., Horsburgh, K.J., and Green, J.A.M., 2012, "The Impact of Future Sea-Level Rise on the European Shelf Tides", *Continental Shelf Research*, Vol. 35, pp. 1–15.

Pierson, W. J., and L. Moskowitz, 1964, "A Proposed Spectral Form for Fully Developed Wind Seas Based on the Similarity Theory of S. A. Kitaigorodskii", *Journal of Geophysical Research*, Vol. 69, No. 24, pp. 5181–5190.

Poulose, J., A.D. Rao, and P.K. Bhaskaran, 2018, "Role of Continental Shelf on Non-Linear Interaction of Storm Surges, Tides and Wind Waves: An Idealized Study Representing the West Coast of India", *Estuarine, Coastal and Shelf Science*, Vol. 207, pp. 457–470.

Ragno, E., A. Antonini, and D. Pasquali, 2023, "Investigating Extreme Sea Level Components and Their Interactions in the Adriatic and Tyrrhenian Seas", *Weather and Climate Extremes*, Vol. 41.

Ris, R. C., L. H. Holthuijsen, and N. Booij, 1999, "A Third-Generation Wave Model for Coastal Regions: 2. Verification", *Journal of Geophysical Research: Oceans*, Vol. 104, No. C4, pp. 7667–7681.

Rogers, D., D. Lincke, J. Hinkel, and R. J. Nicholls, 2025, "The Role of Climate and Population Change in Global Flood Exposure and Vulnerability", *Nature Communications*, in press.

Rummukainen, M., 2009, "State-Of-The-Art with Regional Climate Models", *Wiley Interdisciplinary Reviews: Climate Change*, Vol. 1, No. 1, pp. 82–96.

Rusu, E., 2019, "A 30-Year Projection of the Future Wind Energy Resources in the Coastal Environment of the Black Sea", *Renewable Energy*, Vol. 139, pp. 228–234.

Rusu, L., 2020, "A Projection of the Expected Wave Power in the Black Sea until the End of the 21st Century", *Renewable Energy*, Vol. 160, pp. 136–147.

Sahoo, B., T. Sahoo, and P.K. Bhaskaran, 2021, "Wave–Current-Surge Interaction in A Changing Climate over a Shallow Continental Shelf Region", *Regional Studies in Marine Science*, Vol. 46.

Salauddin, M., J. J. O’Sullivan, S. Abolfathi, and J. M. Pearson, 2021, “Eco-Engineering of Seawalls—An Opportunity for Enhanced Climate Resilience from Increased Topographic Complexity”, *Frontiers in Marine Science*, Vol. 8.

Saxena, S., R. Purvaja, G. M. D. Suganya, and R. Ramesh, 2013, “Coastal Hazard Mapping in the Cuddalore Region, South India”, *Natural Hazards*, Vol. 66, No. 3, pp. 1519–1536.

Sekovski, I., L. Del Río, and C. Armaroli, 2020, “Development of a Coastal Vulnerability Index Using Analytical Hierarchy Process and Application to Ravenna Province (Italy)”, *Ocean and Coastal Management*, Vol. 183.

Shankar, N. J., and R. Jayaratne, 2003, “Wave Run-Up and Overtopping on Smooth and Rough Slopes of Coastal Structures”, *Ocean Engineering*, Vol. 30, No. 2, pp. 221–238.

Silva, A. P., A. H. F. Klein, A. F. H. Fetter-Filho, C. J. Hein, F. J. Méndez, M. F. Broggio, and C. Dalinghaus, 2020, “Climate-Induced Variability in South Atlantic Wave Direction over the Past Three Millennia”, *Scientific Reports*, Vol. 10.

Slangen, A. B. A., M. D. Palmer, C. M. L. Camargo, J. A. Church, T. L. Edwards, T. H. J. Hermans, L. J. Lowe, G. A. Meehl, B. Meyssignac, S. Ospina-Noreña, T. R. Payne, and R. S. W. van de Wal, 2023, “The Evolution of 21st Century Sea-Level Projections From IPCC AR5 to AR6 and Beyond”, *Cambridge Prisms: Coastal Futures*, Vol. 1.

Stockdon, H. F., J. W. Long, M. L. Palmsten, A. van der Westhuysen, K. S. Doran, and R. J. Snell, 2023, “Operational Forecasts of Wave-Driven Water Levels and Coastal Hazards for US Gulf and Atlantic Coasts”, *Communications Earth and Environment*, Vol. 4.

Stockdon, H. F., R. A. Holman, P. A. Howd, and A. H. Sallenger Jr., 2006, “Empirical Parameterization of Setup, Swash, and Runup”, *Coastal Engineering*, Vol. 53, No. 7, pp. 573–588.

Sun, W., B. Liang, Z. Shao, and Z. Wang, 2022, "Analysis of Komen Scheme in the SWAN Model for the Whitecapping Dissipation During the Tropical Cyclone", *Ocean Engineering*, Vol. 266.

SWAN Team, 2024, *SWAN User Manual: Cycle III Version 41.51*, Scientific and Technical Documentation, Delft University of Technology.

Taylor, K. E., R. J. Stouffer, and G. A. Meehl, 2012, "An Overview of CMIP5 and the Experiment Design", *Bulletin of the American Meteorological Society*, Vol. 93, No. 4, pp. 485–498.

Tebaldi, C., Ranasinghe, R., Vousdoukas, M., Rasmussen, D. J., Vega-Westhoff, B., Kirezci, E., Kopp, R. E., Sriver, R., and Mentaschi, L., 2021, "Extreme Sea Levels at Different Global Warming Levels", *Nature Climate Change*, Vol. 11, No. 9, pp. 746–751.

Tiggeloven, T., H. de Moel, H. C. Winsemius, D. Eilander, G. Erkens, E. Gebremedhin, et al., 2020, "Global-Scale Benefit–Cost Analysis of Coastal Flood Adaptation to Different Flood Risk Drivers Using Structural Measures", *Natural Hazards and Earth System Sciences*, Vol. 20, No. 4, pp. 1025–1044.

Van der Meer, J. W., and T. Bruce, 2014, "New Physical Insights and Design Formulas on Wave Overtopping at Sloping and Vertical Structures", *Journal of Waterway, Port, Coastal, and Ocean Engineering*, Vol. 140, No. 6.

Van der Westhuysen, A. J., 2007, *Advances in the Spectral Modelling of Wind Waves in the Nearshore*, Ph.D. Thesis, Delft University of Technology.

Vautard, R., A. Gobiet, D. Jacob, M. Belda, A. Colette, J. Fernández, M. García-Díez, K. Goergen, I. Güttler, T. Halenka, T. Karacostas, E. Katragkou, K. Keuler, S. Kotlarski, S. Mayer, E. van Meijgaard, G. Nikulin, M. Patarčić, J. Scinocca, S. Sobolowski, M. Suklitsch, C. Teichmann, K. Warrach-Sagi, V. Wulfmeyer, and P. Yiou, 2013, "The Simulation of European Heat Waves from an Ensemble of Regional Climate Models within the EURO-CORDEX Project", *Climate Dynamics*, Vol. 41, pp. 2555–2575.

Vitousek, S., P. Barnard, C. Fletcher, N. Frazer, L. Erikson, and C. D. Storlazzi, 2017, "Doubling of Coastal Flooding Frequency Within Decades Due to Sea-Level Rise", *Scientific Reports*, Vol. 7, No. 1.

Vousdoukas, M. I., L. Mentaschi, E. Voukouvalas, A. Bianchi, F. Dottori, and L. Feyen, 2018, "Climatic and Socioeconomic Controls of Future Coastal Flood Risk in Europe", *Nature Climate Change*, Vol. 8, No. 9, pp. 776–780.

Vousdoukas, M. I., L. Mentaschi, E. Voukouvalas, M. Verlaan, and L. Feyen, 2017, "Extreme Sea Levels on the Rise Along Europe's Coasts", *Earth's Future*, Vol. 5, No. 3, pp. 304–323.

Walpole, R. E., R. H. Myers, S. L. Myers, and K. Ye, 2010, *Probability and Statistics for Engineers and Scientists*, 2nd Edition, Pearson Prentice Hall, Boston.

WAMDI group, 1988, "The WAM Model: A Third Generation Ocean Wave Prediction Model", *Journal of Physical Oceanography*, Vol. 18, No. 12, pp. 1775–1810.

Wang, S., C. K. Shum, M. Bevis, X. He, Y. Zhang, Y. Ding, C. Zhang, and J.-P. Montillet, 2025, "Sea Level Reconstruction Reveals Improved Separations of Regional Climate and Trend Patterns over the Last Seven Decades", *Earth System Science Data Discussions*, in review.

Weber, M., V. Barth, and K. Hasselmann, 2005, "A Multi-Actor Dynamic Integrated Assessment Model (MADIAM) of Induced Technological Change and Sustainable Economic Growth", *Ecological Economics*, Vol. 54, No. 2-3, pp. 306–327.

Whitham, G. B., and T. C. T. Ting, 1976, "Linear and Nonlinear Waves", *Journal of Applied Mechanics*, Vol. 43, No. 1, pp. 190–190.

Wilmes, S.-B., J. A. M. Green, N. Gomez, T. P. Rippeth, and H. Lau, 2017, "Global Tidal Impacts of Large-Scale Ice Sheet Collapses", *Journal of Geophysical Research: Oceans*, Vol. 122, No. 11, pp. 8354–8370.

Wood, M., I.D. Haigh, Q.Q. Le, H.N. Nguyen, H.B. Tran, S.E. Darby, R. Marsh, N. Skliris, J.J.-M. Hirschi, R.J. Nicholls, and N. Bloemendaal, 2023, “Climate-Induced Storminess Forces Major Increases in Future Storm Surge Hazard in the South China Sea Region”, *Natural Hazards and Earth System Sciences,* Vol. 23, No. 7, pp. 2475–2504.

Xie, D., Q. P. Zou, A. Mignone, and J. D. MacRae, 2019, “Coastal Flooding from Wave Overtopping and Sea Level Rise Adaptation in the Northeastern USA”, *Coastal Engineering*, Vol. 150, pp. 39–58.

Yan, K., M. Muis, M. Irazoqui Apecechea, and M. Verlaan, 2020a, “Water Level Change Indicators for the European Coast from 1977 to 2100 Derived from Climate Projections”, *Copernicus Climate Change Service (C3S) Climate Data Store (CDS)*, accessed on March 1, 2023.

Yan, K., M. Muis, M. Irazoqui, M. Verlaan, 2020b, “Water Level Change Time Series for The European Coast from 1977 to 2100 Derived from Climate Projections”, *Copernicus Climate Change Service (C3S) Climate Data Store (CDS),* accessed on March 1, 2023.

Yılmaz, O. S., 2022, “Flood Hazard Susceptibility Areas Mapping Using Analytical Hierarchical Process (AHP), Frequency Ratio (FR) And AHP-FR Ensemble Based on Geographic Information Systems (GIS): A Case Study for Kastamonu, Türkiye”, Acta Geophysica, Vol. 70, No. 6, pp. 2747–2769.

Zhai, R., C. Huang, W. Yang, L. Tang, and W. Zhang, 2023, “Applicability Evaluation of ERA5 Wind and Wave Reanalysis Data in the South China Sea”, *Journal of Ocean and Limnology*, Vol. 41, No. 2, pp. 495–517.

Zhou, M., and S. Wang, 2024, “The Risk of Concurrent Heatwaves and Extreme Sea Levels Along the Global Coastline is Increasing”, *Communications Earth & Environment*, Vol. 5.

Zijlema, M., 2010, “Computation of Wind-Wave Spectra in Coastal Waters with SWAN on Unstructured Grids”, *Coastal Engineering*, Vol. 57, No. 3, pp. 267–277.

Zijlema, M., and A. J. van der Westhuysen, 2005, “On Convergence Behaviour and Numerical Accuracy in Stationary SWAN Simulations of Nearshore Wind Wave Spectra”, *Coastal Engineering*, Vol. 52, No. 3, pp. 237–256.